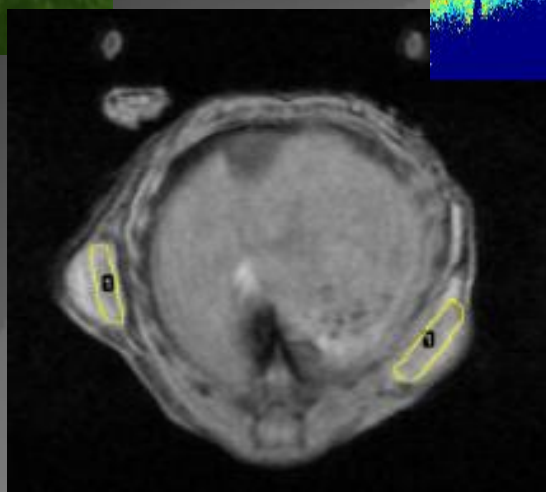
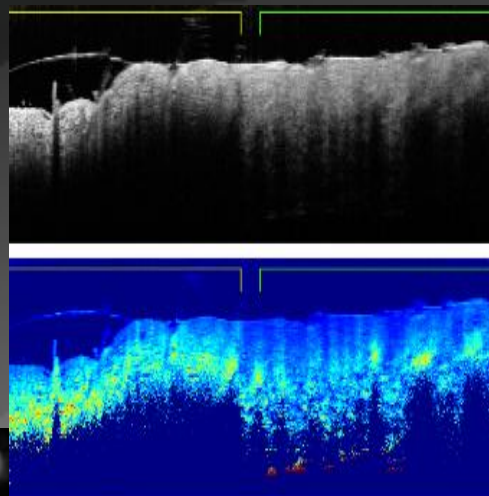
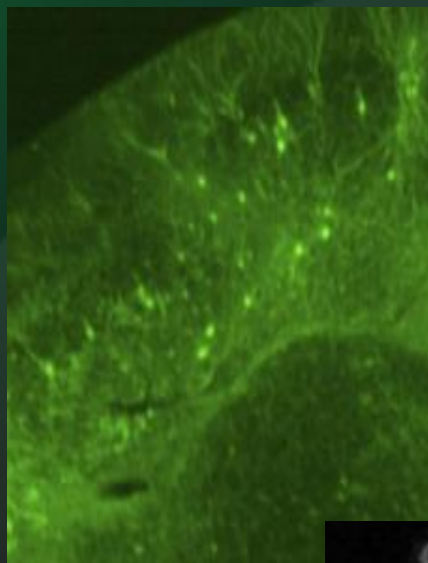


# Chinese-Russian Workshop on Biophotonics and Biomedical Optics-2023



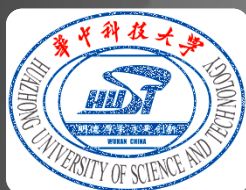
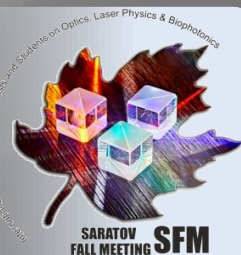
SEPTEMBER 25 - 26, 2023

SARATOV STATE UNIVERSITY, SARATOV, RUSSIA

WUHAN NATIONAL LABORATORY FOR OPTOELECTRONICS,

HUAZHONG UNIVERSITY OF SCIENCE

AND TECHNOLOGY, CHINA



ИНЖЕКТ  
РОСАТОМ



ООО НПТ  
Наноструктурная Технология Стекла

OPTICA | Formerly  
OSA

Saratov State University (National Research University of Russia)

**Chinese-Russian Workshop on  
Biophotonics and Biomedical Optics-2023  
Proceedings of Chinese-Russian Workshop**

Edited by Polina A. Dyachenko, Dan Zhu and Valery V. Tuchin

SEPTEMBER 25 – 26, 2023

SARATOV

КИТАЙСКО-РОССИЙСКИЙ СЕМИНАР ПО  
БИОФОТОНИКЕ И БИМЕДИЦИНСКОЙ ОПТИКЕ-2023

Сборник материалов китайско-российского семинара

Под редакцией Полины А. Дьяченко, Дана Чжу и Валерия В. Тучина

25-26 СЕНТЯБРЯ 2023 Г.

САРАТОВ



УДК 535.8(082)  
ББК 22.34  
К 45

**Chinese-Russian Workshop on Biophotonics and Biomedical Optics-2023. Proceedings of Chinese-Russian Workshop/** Edited by P.A. Dyachenko, Dan Zhu and V.V. Tuchin – Saratov, Russian Federation: Publishing house "Saratov source", 2023. – 50 p.

**ISBN 978-5-6051304-0-6**

The collection includes extended proceedings of lectures and reports of the participants of the Chinese-Russian Workshop on Biophotonics and Biomedical Optics, held online as part of the Saratov Fall Meeting 2023.

Китайско-российский семинар по биофотонике и биомедицинской оптике-2023. Материалы Китайско-российского семинара/ Под редакцией П.А. Дьяченко, Дан Чжу и В.В. Тучина – Саратов, Российская Федерация. Изд-во "Саратовский источник", 2023. – 50 с.

Сборник включает расширенные материалы лекций и докладов участников китайско-российского семинара по биофотонике и биомедицинской оптике, проведенного онлайн в рамках осенней встречи в Саратове 2023. В сборник трудов конференции вошли статьи участников Китайско-российского семинара по биофотонике и биомедицинской оптике, прошедшего онлайн в рамках Saratov Fall Meeting 2023.

Saratov State University (National Research University of Russia), 410012, Saratov, Astrakhan str., 83

Саратовский национальный исследовательский государственный университет имени Н. Г. Чернышевского, 410012, Саратов, улица Астраханская, 83

УДК 535.8(082)  
ББК 22.34

## Contents

1. CHINESE-RUSSIAN WORKSHOP ON BIOPHOTONICS AND BIOMEDICAL OPTICS-2023 .....	4
2. STUDY OF IN SITU PAIN RELIEF AND PERSONALIZED TREATMENT OF PDT, Dongqin Lei, Rongrui Zhng, Jing Wang, Weihui Zeng And Cuiping Yao .....	5
3. OPTICAL IMAGING AND MODULATION OF MENINGEAL LYMPHATIC VESSELS, Feifan Zhou .....	6
4. CELLULAR MEMBRANE-DERIVED NANOVESICLES AS A VERSATILE DRUG DELIVERY SYSTEM FOR IMAGING-GUIDED CANCER THERAPY, Yang Zhang And Gang Liu .....	7
5. DEEP PENETRATION SUPERRESOLUTION IMAGING WITH ADAPTIVE OPTICS AND MULTI-FOCAL STRUCTURED ILLUMINATION, Chenshuang Zhang, Yong Zhang, Danying Lin, Bin Yu, Junle Qu .....	8
6. COMPLEX APPROACH TO <i>IN VITRO</i> AND <i>IN VIVO</i> MONITORING OF THE DEGRADATION OF IMPLANTS BASED ON ESTER COPOLYMERS USING MR AND FLUORESCENCE IMAGING, Astemir R. Likhov, Asiya N. Saydasheva, Natalia I. Kazachkina, Dmitry D. Demin, Veronika N. Volodina, Victoria V. Deeva, Daniil O. Antonov, Ilya D. Solovyev, Nadezhda N. Marynich, Irina G. Meerovich, Sofya V. Atzigeida, Daria K. Tuchina, Valery V. Tuchin, And Victoria V. Zherdeva .....	9
7. THREE-DIMENSIONAL VIRTUAL OPTICAL CLEARING FOR HIGH-THROUGHPUT DEEP TISSUE IMAGING, Jiajia Chen, Yao Zheng, Wei Gong And Ke Si .....	15
8. REFRACTOMETRIC ANALYSIS OF BLOOD SERUM, Ludmila Plotnikova, Olga Vezo, Andrey Garifullin , Aleksey Kuvshinov, Sergey Voloshin And Alexander Polyanichko .....	16
9. INVESTIGATION OF THE EFFECT OF PROLONGED EXPOSURE TO OCA-AEROSOL (GLYCERIN/PROPYLENE GLYCOL) ON RAT PLASMA BY RAMAN SPECTROSCOPY, Arina Sokova, Ekaterina Lazareva, Alexander Polozhenkov, Artem Mylnikov, Alla Bucharskaya And Valery Tuchin .....	18
10. UPCONVERSION SUPER-RESOLUTION MICROSCOPY, Qiuqiang Zhan .....	21
11. SHINING TO TRADITIONAL MEDICINE, Ting Li .....	22
12. TISSUE OPTICAL CLEARING FOR WHOLE-ORGAN IMAGING, Tingting Yu .....	23
13. THE NEAR-INFRARED-II FLUORESCENCE IMAGING PROBES FOR SURGICAL NAVIGATION, Ming Wu, Xiaolong Liu .....	24
14. EFFECT OF THE DOSE OF UPCONVERSION NANOPARTICLES ON THE REFRACTIVE INDEX OF TISSUES IN THE DEVELOPMENT OF MODEL LIVER CANCER, Ekaterina Lazareva, Roman Anisimov, Maria Lomova, Anna Doronkina, Artem Mylnikov, Nikita Navolokin, Vyacheslav Kochubey And Irina Yanina ..	25
15. OPTICAL MULTIMODAL STUDY OF SKIN TUMORS, Elina Genina, Yury Surkov, Isabella Serebryakova, Ekaterina Lazareva, Yana Kuzinova, Sergey Zaytsev, Olga Konopatskova, Dmitry Safronov, Sergey Kapralov, And Valery Tuchin .....	27
16. MODELING OF COVID-19 SPREAD: FROM CITY SCALE TO COUNTRY SCALE, Mikhail Kirillin, Aleksandr Khilov, Valeriya Perekatova, Ekaterina Sergeeva, Daria Kurakina, Ilya Fiks, Nikolay Saperkin, Ming Tang; Yong Zou, Elbert Macau, Americo Cunha Jr And Efim Pelinovsky .....	32
17. STUDY OF OSMOTIC AND CROSS-LINKING DEFORMATIONS IN BIOLOGICAL TISSUES BY OPTICAL COHERENCE ELASTOGRAPHY, Yulia Alexandrovskaya, Ekaterina Kasianenko, Olga Baum, Alexander Sovetsky, Alexander Matveev, Tatiana Shmigol, Pavel Karavaikin, Vadim Negrebetsky, Vladimir Zaitsev .....	37
18. ASSESSING THE APPLICABILITY OF AEROGELS FOR THE ANALYSIS OF SKIN VAPOR SAMPLES IN TERAHERTZ RADIATION, Viacheslav Zasedatel, Yana Tuleneva, Yury Kistenev .....	38
19. RAMAN-LIBS FOR TUMOR TISSUE IMAGING AND CELLS DETECTION, Youyuan Chen, Pengkun Yin, Zhengying Peeng, Qingyu Lin, Yixiang Duan .....	42
20. PILOT STUDY OF A LOW-INVASIVE EX VIVO METHOD OF OPTICAL CLEARING SKIN USING NEEDLE-FREE INJECTION OF OPTICAL CLEARING AGENTS, Yuriy Surkov, Isabella Serebryakova, Elina Genina and Valery Tuchin .....	43
21. INFLUENCE OF WAVELENGTH OF LIGHT ON ANTIMYCOTIC ACTIVITY OF CHLORINE-CONTAINING PHOTODYNAMIC DRUGS, Andrei Belikov, Yulia Fedorova, Sergey Smirnov, Anastasia Kozlova And Lyudmila Kraeva .....	47
22. PHOTOSAFE NON-INVASIVE DETECTION OF DEEP-SEATED LESIONS VIA TRANSMISSION RAMAN SPECTROSCOPY, Jian Ye .....	50



## **CHINESE-RUSSIAN WORKSHOP ON BIOPHOTONICS AND BIOMEDICAL OPTICS-2023**

**SEPTEMBER 25 – 26, 2023, SARATOV, RUSSIA**

### *Chairs:*

**Dan Zhu**, Wuhan National Laboratory for Optoelectronics, Huazhong University of Science and Technology, Wuhan, China

**Valery V. Tuchin**, Saratov State University, Institute of Precision Mechanics and Control of FRC “Saratov Scientific Centre of the Russian Academy of Sciences”, Tomsk State University, RC of Biotechnology of the RAS, Russia

### *Secretaries:*

**Tingting Yu**, Wuhan National Laboratory for Optoelectronics, Huazhong University of Science and Technology, Wuhan, China

**Polina A. Dyachenko**, Saratov State University, Tomsk State University, Russia

**The traditional Chinese-Russian Workshop on Biophotonics and Biomedical Optics-2023** was held online on September 25-26, 2023. It is designed to bring together Russian and Chinese scientists, engineers and clinical researchers from various scientific disciplines involved in the application of optics, photonics and imaging technologies for solving problems of biology and medicine. The scope of this bilateral forum ranges from basic research to instrumentation, biological and clinical applications.

- The topics of this forum are broad and will cover (but not limited to) the following:
- Optical Interactions in Tissue and Cells
- Biomedical Spectroscopy, Microscopy and Imaging
- Advanced Optical Techniques for Clinical Medicine
- Multimodal Biomedical Imaging
- Nanobiophotonics
- Photonic Therapeutics, Diagnostics and Instrumentations
- Tissue Optical Clearing and Drug Delivery
- Antimicrobial and Antiviral Phototherapies
-

## STUDY OF IN SITU PAIN RELIEF AND PERSONALIZED TREATMENT OF PDT

DONGQIN LEI<sup>1</sup>, RONGRUI ZHNG<sup>1</sup>, JING WANG<sup>1</sup>, WEIHUI ZENG<sup>2</sup> AND CUIPING YAO<sup>1\*</sup><sup>1</sup>*School of Life Science and Technology, Xi'an Jiaotong University, China*<sup>2</sup>*The Second Affiliated Hospital, School of Medicine, Xi'an Jiaotong University, China*  
zsycp@xjtu.edu.cn

## ABSTRACT

Photodynamic therapy has been used for treatment of port wine stains in clinic, which has a good outcome, especially for children. However, the pricking and burning sensation during photodynamic therapy is very acute, which is hard to bear for children and prevent cooperation. In addition, multiple treatments were needed for most patients. Memories of pain can impose a netative physiological or psychological effects on children. These disadvantages limit the use of PDT for port wine stain. Therefore, managing patients' pain during PDT is a very important challenge that clinicians must face. In some studies general anaesthesia was employed during PDT. However, there is no consensus on the best anaesthetic techniques to use when performing PDT for PWS [1]. The safety and efficiency of general anaesthesia should be further assessed. Here we have developed an in situ anaesthesia strategies, in which a nanostructure was designed to encapsulate the photosensitizer and lidocaine, a kind of local anesthetic, for medicine delivery and in situ releasing. For assessment of the pain relief of the pain during photodynamic therapy, the xenografted tumor of melanoma treatment was used to mimic port wine stain treatment due to the abnormal and abundant blood vessel in tumor. For experiments, the nanostructures were intravenously injected into melanoma tumor-bearing mice, in vivo fluorescence images showed that the photosensitizer could enormously accumulate at the tumor site. Electrophysiological experiment was used to prove the effectiveness of pain relief by using nanostructure during PDT as shown in figure 1, and the amount of expression of pain-related proteins further confirmed the results. The in vitro and in vivo anti-tumor results revealed excellent photodynamic efficacy. Therefore, such anesthetic in situ released nanostructure with photosensitizer might provide a promising new strategy for pain relief during PDT as well as enhance PDT efficacy. Furthermore, a method for measuring pain during PDT through electrophysiological experiments has been proposed for the first time. On the other hand, an so different outcomes were observed for different people with same parameters such as light intensity, concentration of photosensitizer in clinic, which should be relative to the personalized factors such as photosensitizer accumulation, locally blood oxygen and so on. To realize the personalized treatment of the PDT, using animal model, a hyperspectral imaging system was build based on a liquid crystal tunable filter. By combining wide-field spectrally resolved fluorescence imaging with a dual-band fluorescence spectral correction algorithm, we achieved quantitative detection of photosensitizer concentration. Also multispectral imagings were used to determin tissue oxygen saturation by calculating the absorption difference of hemoglobin. Base on these information, narrow-band optical imaging was emoloyed to calculate changes in target vessel diameter for quantitative assessment of photodynamic damage. The experimental results demonstrated the effective detection of each dose parameter in PDT using the hyperspectral system, enabling the prediction of treatment outcomes. we expected that these results could be useful for devepment of the persenalized treatment.

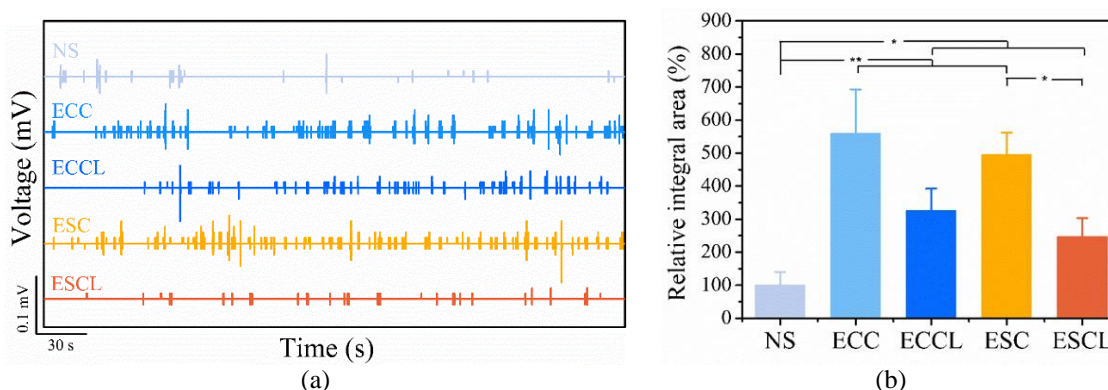


**Figure:** (a) The electrophysiological recordings of the sciatic nerve of mice after being treated by the micelles under 660 nm laser (960 mW cm<sup>-2</sup>) illumination in 5 min (b) The relative integral area of the neural signal

## REFERENCES

- [1] Linlin Tang, Wei Liu, Qian Yu, Hongjie Guo, Xue Yang and Ling Xiong, General anaesthesia for photodynamic therapy of port-wine stain in children: A retrospective study, *Photodiagnosis and Photodynamic Therapy*, 41, 103273, 2023,

OPTICAL IMAGING AND MODULATION OF MENINGEAL LYMPHATIC VESSELS

FEIFAN ZHOU<sup>1</sup>

<sup>1</sup> *Key Laboratory of Biomedical Engineering of Hainan Province, School of Biomedical Engineering, Hainan University, China*

[zhouff@hainanu.edu.cn](mailto:zhouff@hainanu.edu.cn)

**ABSTRACT**

Meningeal lymphatic vessels (mLVs) have been shown to be involved in amyloid beta ( $A\beta$ ) clearance, which is considered as a potential therapeutic target for Alzheimer's disease (AD). However, how to ameliorate AD by optical imaging and modulation of mLVs remains a great challenge. Based on the superficial spatial distribution of mLVs, photoacoustic imaging and fluorescence imaging were used to observe and evaluate the structure and function of mLVs, and corresponding modulation strategy was developed to regulate mLV drainage for improvement of cognition and AD-associated pathology.

## CELLULAR MEMBRANE-DERIVED NANOVESICLES AS A VERSATILE DRUG DELIVERY SYSTEM FOR IMAGING-GUIDED CANCER THERAPY

YANG ZHANG AND GANG LIU

*State Key Laboratory of Molecular Vaccinology and Molecular Diagnostics & Center for Molecular Imaging and Translational Medicine, School of Public Health, Xiamen University, China  
gangliu.cmitm@xmu.edu.cn*

### ABSTRACT

The development of smart nanoparticles that enable to circumvent biological barriers and transport cargoes to target sites in the body promises safer and more effective drug delivery. Since cell membrane-based nanovesicles have the characteristics of both nano-sized and cell-based drug delivery platforms, they are regarded as promising cancer targeted delivery tools for both endogenous and exogenous cargoes. What is perhaps most fascinating about these cell membrane-based drug delivery systems is that the natural targeting ability of those producing cells makes the exogenous engineering of targeting moieties unnecessary. In our laboratory, a variety of bio-inspired nano-biomaterials, such as virus-like nanoparticles and ferritin nanocages, have been studied for drug delivery, cell labeling, and gene therapy. A number of hybrid nanoparticles containing synthetic and biological components have been utilized for achieving sustained release and target-specific delivery. We are particularly interested in cell membrane-based nanoparticles containing bioactive molecules useful for therapeutic and imaging applications in cancer theranostics. In this presentation, an innovative biomimetic nanoparticle platform for delivering therapeutic anticancer agents and imaging-guided cancer therapy will be introduced. In addition, the major hurdles in the clinical translation of cell membrane-based delivery systems will be discussed.

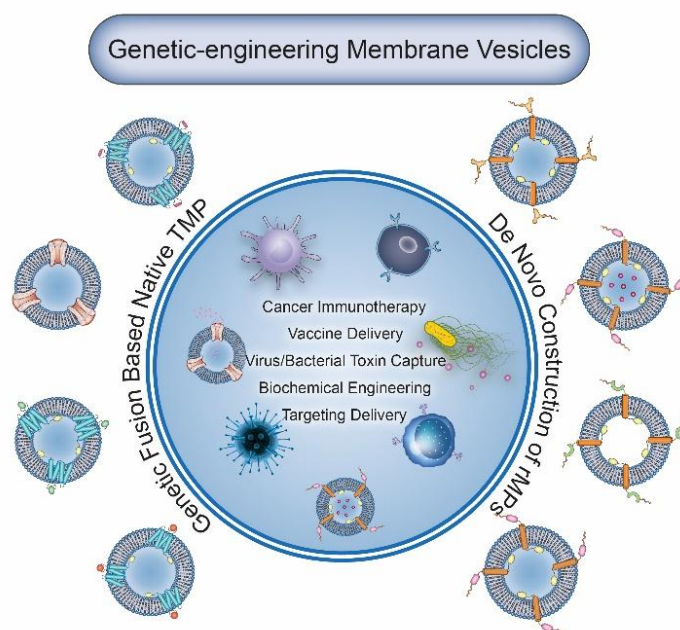


**Figure 1:** The functional proteins can be anchored on the cell surface via genetic engineering tactics for various application prospects including cancer immunotherapy, vaccine delivery, virus/bacterial toxin capture, cancer oncolytic virotherapy and chemotherapy drugs delivery.

### REFERENCES

- [1] C. Liu, et al. *Nat Nanotechnol.* 2022,17, 531-540.
- [2] X. Pang, et al, *Adv. Mater.* 2019, 31, 1902530.
- [3] P. Zhang, et al, *Adv. Mater.* 2018, 30, 1705350.

**DEEP PENETRATION SUPERRESOLUTION IMAGING WITH ADAPTIVE OPTICS AND  
MULTI-FOCAL STRUCTURED ILLUMINATION**

CHENSHUANG ZHANG, YONG ZHANG, DANYING LIN, BIN YU, JUNLE QU

*Center for Biomedical Optics and Photonics, College of Physics and Optoelectric Engineering,  
Shenzhen University*

jlqu@szu.edu.cn

**ABSTRACT**

Optical imaging is crucial for biomedical research and clinical diagnosis. Improved depth and resolution are necessary for studying synaptic functions, neuronal structures, and microvessels in living animals' brain tissue. We developed an adaptive optics-based MSIM system (AO-MSIM) to overcome the limitations of multi-focus structured illumination microscopy (MSIM) when imaging thick samples. By generating a multi-focus excitation lattice using a spatial light modulator, we achieved multi-focus structured illumination scanning imaging. Aberrations in the excitation and emission paths were corrected using wavefront information, a spatial light modulator, and a deformable mirror. With pixel relocation and deconvolution image reconstruction algorithms, AO-MSIM achieved 150nm spatial resolution at a 500 $\mu$ m imaging depth, demonstrating its application in imaging thick brain tissue samples.

## COMPLEX APPROACH TO *IN VITRO* AND *IN VIVO* MONITORING OF THE DEGRADATION OF IMPLANTS BASED ON ESTER COPOLYMERS USING MR AND FLUORESCENCE IMAGING

ASTEMIR LIKHOV<sup>1</sup>, ASIYA SAYDASHEVA<sup>1</sup>, NATALIA KAZACHKINA<sup>1</sup>, DMITRY DEMIN<sup>3</sup>, VERONIKA VOLODINA<sup>1</sup>, VICTORIA DEEVA<sup>1</sup>, DANIIL ANTONOV<sup>1</sup>, ILYA SOLOVYEV<sup>1</sup>, NADEZHDA MARYNICH<sup>1</sup>, IRINA MEEROVICH<sup>1</sup>, SOFYA ATZIGEIDA,<sup>2</sup> DARIA TUCHINA<sup>1,2</sup>, VALERY TUCHIN<sup>1,2</sup>, AND VICTORIA ZHERDEVA<sup>1\*</sup>

<sup>1</sup> RC of Biotechnology of the RAS, Moscow, Russia;

<sup>2</sup> Saratov State University, Saratov, Russia;

<sup>3</sup> MIREA — Russian Technological University, Moscow, Russia

vjerdeva@inbi.ras.ru

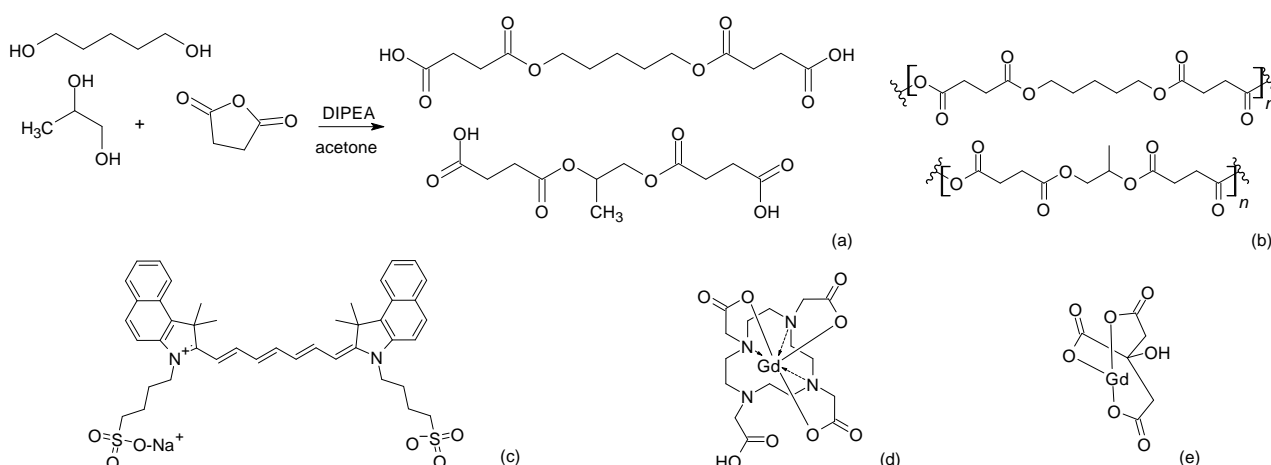
### ABSTRACT

Copolymer-based materials are widely used in medicine and biotechnology to produce various medical products, such as implants, prostheses, surgical suture material drug delivery systems, sensors and even triboelectric nanogenerators. The interest in such materials is increasing due to their multifunctional properties, such as the controlled degradation, the ability to stimulate tissue regeneration, the ability to act as carriers for controlled drug release, and triboelectric properties [1–3]. Some examples of copolymer-based materials include polymer nanoparticles [4], implantable triboelectric nanogenerator [5], polymer hydrogel [6], polymer matrix microcontainer [7], stimuli-responsive polymer materials [8].

Bioresorbable copolymers have the ability to degrade and be absorbed by the body over time. It has been noted that such materials might show high variation of degradation behavior [1].

The aim of our work was to monitor the degradation and assess the biocompatibility of ester copolymers *in vitro* and *in vivo*, as well as to demonstrate the possibility of visualizing these copolymers *in vivo* using a bimodal approach involving magnetic resonance imaging (MRI) and fluorescence imaging.

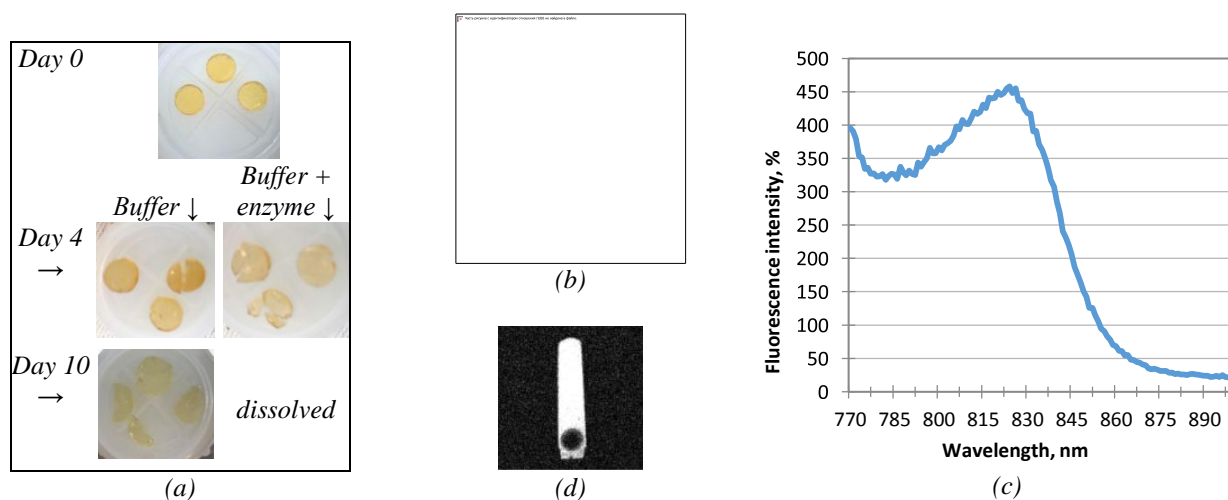
Copolymers were synthesized according to the protocol [2] and with some modification based on the 1,3-propanediol, 1,5-pentadiol, succinic acid and citric acid (Fig.1a, 1b). The copolymers were labeled with indocyanine green (ICG) (Fig. 1c) and magnetic resonance agent such as Gd-DOTA (Gadolinium (III) 1,4,7,10-Tetraazacyclododecane-1,4,7,10-tetraacetate) or Gd-citrate complex (Fig.1d, 1e). Fourier-transform infrared spectroscopy (FTIR) analysis showed no structural differences between the labeled polymer samples and the initial polymers.



**Figure 1:** Compounds used in polymer synthesis: (a) stage 1 - synthesis of monomeric structures from 1,3-propanediol and 1,5-pentadiol - (b) stage 2 - polymerization with the addition of succinic acid or citric acid - (c) ICG - (d) Gd-DOTA - (e) Gd-citrate complex

For all experiments copolymers samples were prepared as 5 mm discs using hole puncher (Fig.2a). The hydrolysis of the copolymers was modeled *in vitro* using buffered physiological solution (PhS) pH 7.4 and heat

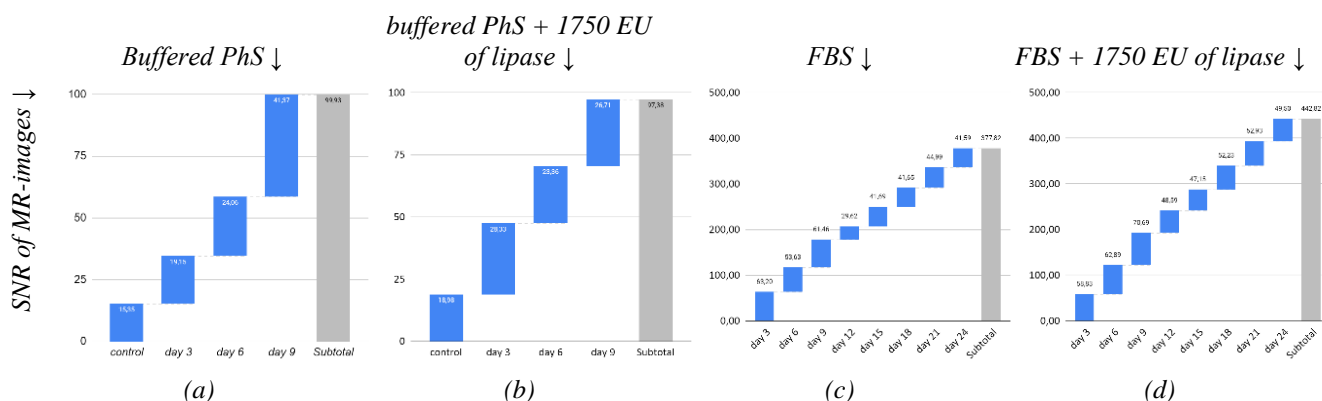
inactivated fetal bovine serum (FBS). Three discs were used in each vial (Fig.2b) for hydrolysis experiments, and the weight of the discs was measured every 3 days (Fig. 2a). Fluorescence and MRI signal changes (Fig.2c, 2d) have been registered at the same dates every 3 days. Porcine pancreas extract stock solution was prepared, and lipase activity was measured as 17500EU using «Lipase color liquid» (Sentinel Diagnostics, Italy). Enzyme solution was used to imitate lipase-mediated hydrolysis. The incubation conditions with the enzyme were set to maintain the physiological lipase enzymatic activity (0-150 EU) for 3 days at +37C°, after which the incubation solution was replaced with the fresh one.



**Figure 2:** Polyester copolymers in vitro study: (a) copolymer discs before hydrolysis (up), at 4<sup>th</sup> day (middle) and 10<sup>th</sup> day (bottom) of non-enzyme and enzyme-mediated degradation in buffered physiological solution - (b) test tubes for the hydrolysis experiment, containing 3 disk samples with enzyme (upper row) and control (lower row) on the 4<sup>th</sup> day of experiment - (c) fluorescence spectra of the ICG incorporated into the copolymer structure - (d) sagittal MR-imaging for the Gd release from the sample

The degradation rate of the copolymers differed in buffered PhS and in FBS. Thus, the hydrolysis caused by enzyme-based solution in FBS proceeded approximately 3 times slower than in PhS. According to Gombotz and Pettit [9], polymers may interact with serum proteins, for example by absorbing them, and this can change polymers properties. We hypothesized that the absorption of serum proteins hinders the availability of ester bonds for enzymes. Figure 3 illustrates the changes in signal to noise ratio (SNR) intensity for MRI and fluorescence intensity (FI) measurements.

The MRI signal in PhS increases nonlinearly due to the swelling and subsequent rapid hydrolysis of the copolymers (Fig.3a). When the enzyme is added, the Gd citrate complex releasing becomes more linear, probably, due to the rapid hydrolysis initiation (Fig.3b). The Gd-citrate release kinetic demonstrates the regular day-by-day rate in FBS (Fig.3c), possibly due to the absorption of serum proteins on the polymer. Complete degradation of the polymer in serum occurs on days 24-28, while in the absence of the enzyme, this process may take 50-70 days. ICG release kinetic is non-linear in PhS and approximate to linear in FBS (Fig.3e, 3f), but the ICG-release FI in FBS+Lipase (Fig.3 h) is dramatically higher in comparing to FBS only (Fig.3g). We presumed that pH and different conditions in our solutions impact its optical properties as it was mentioned repeatedly [12].



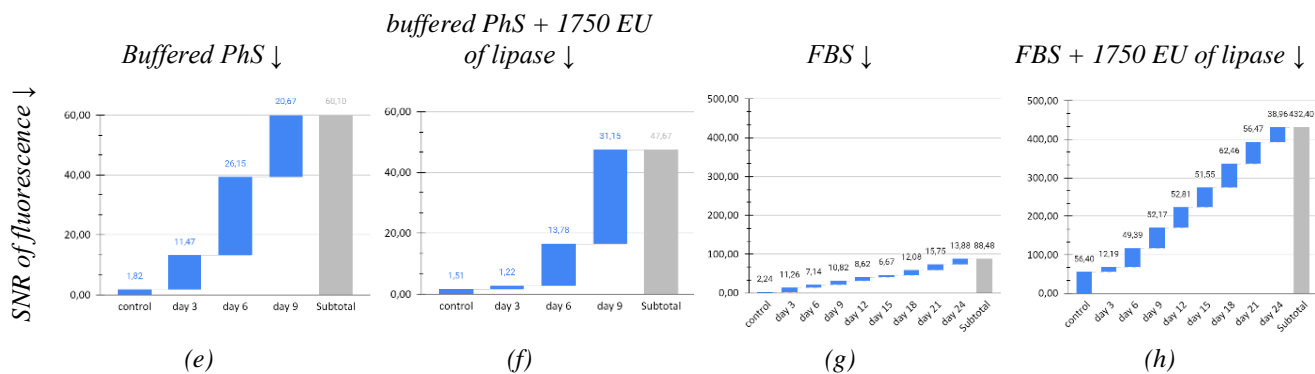


**Figure 3:** Degradation of copolymers in vitro under the different conditions measured by MRI (upper row) and FI (lower row): (a), (e) in buffered PhS - (b), (f) in PhS with addition 1750 EU of lipase - (c), (g) in FBS - (d), (h) in FBS with addition 1750 EU of lipase

Polymers weight loss was correlated to the MRI and FI change during the whole cycle of enzyme-mediated hydrolysis (Fig.4). In the swelling phase, both the weight of the polymer and the MRI and fluorescence signals increase, while in the degradation phase, they are inversely proportional - as the weight decreases, the signals increase. The tilt angle indicates the correlation coefficient, which was calculated as 1 for MRI, while for changes in fluorescence it is not, as fluorescence strongly depends on the environment [10].

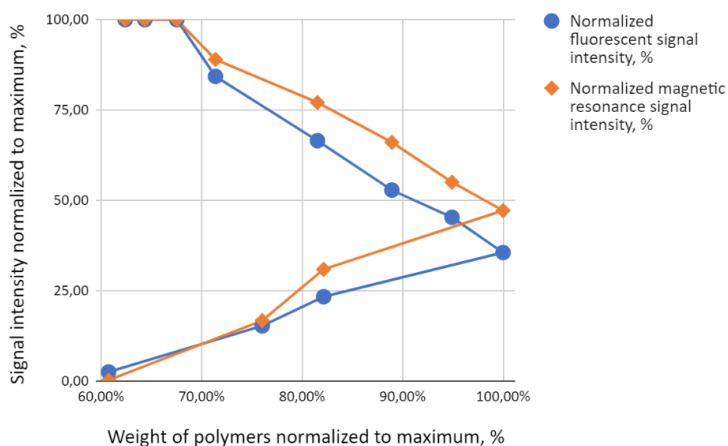
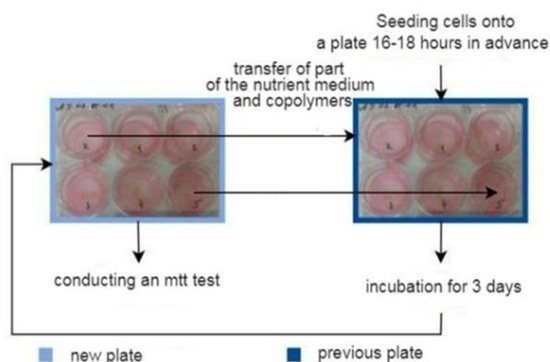
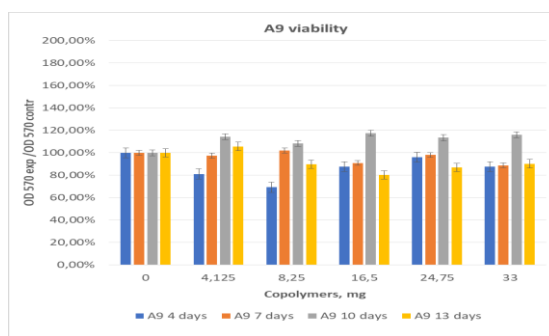


**Figure 4:** Correlation between copolymers' weight change and MRI & FI signals normalized to their maxima during all cycle of hydrolysis in FBS.

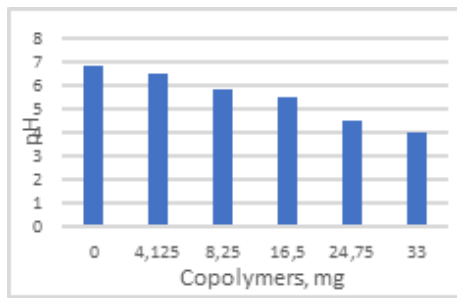
The MTT test was used to assess the toxicity of the copolymers to cells. The experimental design is illustrated in Figure 5a. Copolymer samples showed no toxicity in relation to the mouse cell lines (A9, C2C12) under physiological pH conditions. However, it was observed that in the absence of buffering agents, such as HEPES, the presence of the polymer in the medium led to a shift towards aciditification (pH 4.0-4.5) (Fig. 5b), negatively impacting cell survival. No significant changes in viability in respective of the polymer concentration in the wells were observed for fibroblast-like cells A9 (Fig. 5c). The co-incubation of the polyester copolymers with myoblast-like C2C12 cells resulted in the intensification of cell proliferation (Fig. 5d). The similar effect was previously observed by Y. Guo et.al. and explained by the citrate enhancement effect for *in vivo* skeletal muscle regeneration [11].



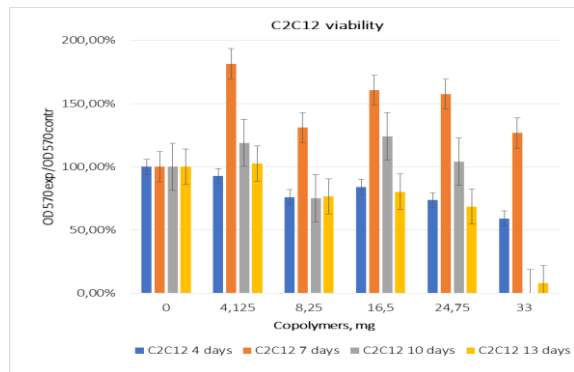
(a)



(c)



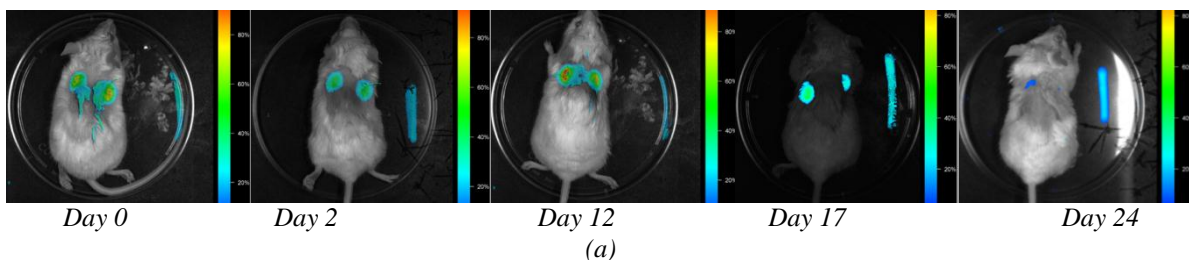
(b)



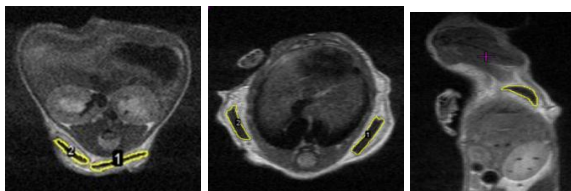
(d)

**Figure 5:** (a) Design of the experiment on the toxicity of copolymers to cells: the copolymer samples contained 0.4mm- pore polyethylene inserts were inserted to the wells with the pre-seeded cells; after 3 days, the insert with copolymer and part of the nutrient medium were transferred into the new wells with pre-seeded cells, and the cells from the previous plate were sent for the MTT test - (b) diagram for pH medium's changes dependence on the copolymers weight at the 3<sup>rd</sup> day of incubation with cells- (c, d) viability of C2C12 myoblast-like cells (c) and A9 fibroblast-like cells (d) in the following by MTT-tests from 4th to 13th days of co-incubation with polyester copolymers in quantity of 0-33 mg/well.

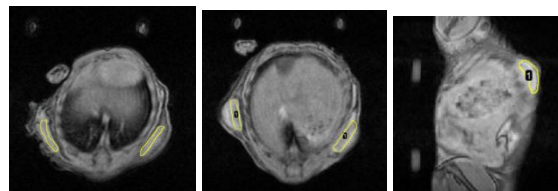
To evaluate the biocompatibility of the copolymers, 5 mm copolymer discs were implanted into BALB/c mice subdorsal. No signs of toxicity or intoxication were observed during all period of observation. Fluorescence images were obtained using planar imaging (Fig. 6a), MRI images were obtained in two modes: T1-weighted gradient echo (T1 3D GRE) (Fig. 6b) and T2-weighted fast spin echo (T2 FSE) (Fig. 6c). ICG fluorescence was detectable up to day 24-28, as well as polymer disks MRI. Similar to the *in vitro* experiments, an initial increase in signal was observed, followed by a gradual attenuation over time. (Fig. 6d, 6e).



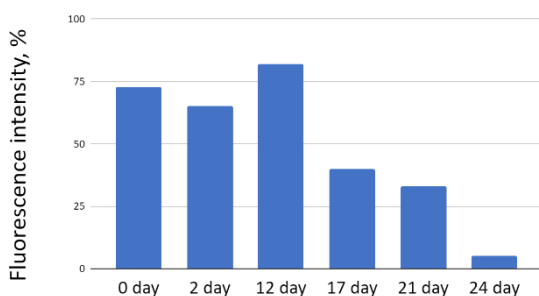
(a)



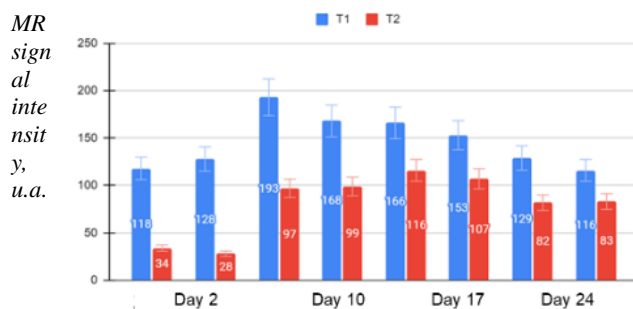
(b)



(c)



(d)



(e)

**Figure 6:** MRI and fluorescence vialisation of copolymer-based implants in mice Balb/c: (a) pseudo-color staining of ICG-labeled polyester copolymers implanted to mice - (b) MR images, obtained in T1 mode - (c) MR images, obtained in T2 mode - (d) changes in fluorescent intensity in vivo - (e) changes in MRI signal intensity in vivo

A side effect observed was the increased acidification of the environment surrounding the polymer, accompanied by aseptic inflammation, which was detected as hyperintensive T2 using MRI in BALB/c mice up to 7-8

days post implantation (Fig.6c). Based on our findings, we hypothesized that improving the biocompatibility of the copolymer could be achieved by reducing its citrate content.

Glycerol is widely used as an optical clearing agent (OCA) in tissues [13, 14]. When tissue is exposed to OCA, due to its reversible dehydration and refractive index matching of the tissue scatterers and interstitial fluid, light scattering decreases and optical transmission through the tissue increases. The kinetics of this process is determined by the time of diffusion of tissue water and OCA molecules in the tissue. Thus, from changing the transmission spectrum of a tissue during the action of an agent on it, one can determine the rate of diffusion of molecules in the tissue [13].

Spectral measurements were carried out *ex vivo* on samples of rat muscle tissue immersed in OCA with the addition of ICG. Figure 7 shows the spectra and time dependences for a number of characteristic wavelengths of collimated transmittance of a tissue sample. In the spectra, absorption bands of ICG near the wavelength of 800 nm and hemoglobin/myoglobin near 550 nm are clearly visible. Tissue transmittance increases with time due to the action of OCA, but to varying degrees at different wavelengths.

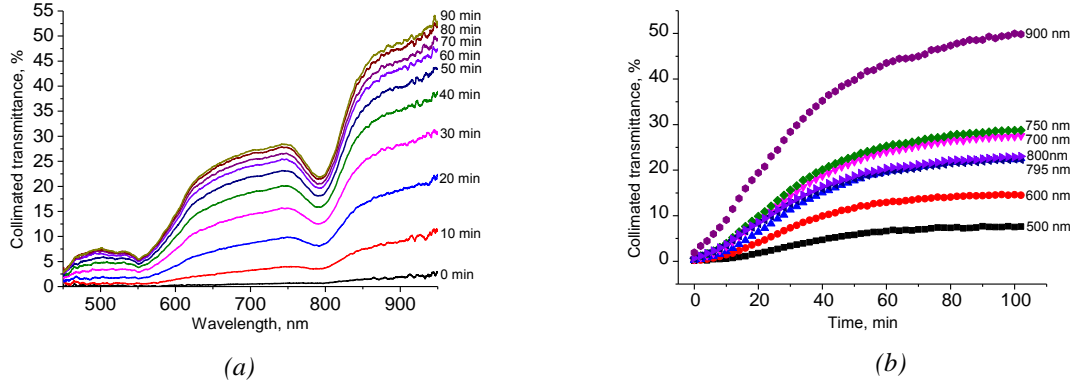


**Figure 7:** Spectra (a) and kinetic dependences at characteristic wavelengths (b) of collimated transmittance of rat muscle tissue sample during immersion in OCA (70% glycerol, 25% water and 5% DMSO) with the addition of ICG ( $5 \times 10^{-3}$  mg/ml).

The measured spectra of tissue samples were used to calculate the rate of diffusion of agents using the algorithm described in [13-15]. Theoretically, the time dependence of the collimated transmittance of the sample was determined using the Bouguer-Beer-Lambert law:

$$T_c^{teor}(\lambda, t) = \exp\{-[\mu_a(\lambda) + \mu_s(\lambda, t)] \cdot l\}, \quad (1)$$

where  $\mu_a(\lambda)$  and  $\mu_s(\lambda, t)$  are the absorption and scattering coefficients of the tissue sample, respectively,  $\text{cm}^{-1}$ ,  $l$  is the thickness of the sample, cm. The effective diffusion coefficient  $D_a$  of an agent in tissue can be extracted using the following relationships:

$$T_c(t) \propto 1 - \exp\left(-\frac{t}{\tau}\right), \quad \tau = \frac{4l^2}{\pi^2 D_a}, \quad (2)$$

where  $\tau$  is the characteristic diffusion time of the agent when it is delivered through both surfaces of the sample (two-side diffusion). The efficiency of optical clearing of the samples was also assessed as the ratio of the difference between the initial ( $\mu_{s_0}$ ) and minimum ( $\mu_{s_{min}}$ ) values of the scattering coefficient to the initial ( $\mu_{s_0}$ ) value in the sample:

$$OC_{eff} = \frac{\mu_{s_0} - \mu_{s_{min}}}{\mu_{s_0}}. \quad (3)$$

Since the exogenous chromophore ICG with a characteristic spectrum was added to the main endogenous chromophores of muscle tissue (hemoglobin/myoglobin) (Fig. 7a), the  $OC_{eff}$  varies in the range of 66% to 86% depending on the selected wavelength. In general, the efficiency of optical clearing of a muscle tissue sample is quite high. At the wavelength of maximum fluorescence intensity of ICG, equal to 820 nm, the intensity of the transmitted light through a layer of muscle tissue, 0.9 mm thick, increases by approximately 25 times, despite some absorption of ICG at this wavelength.

The values of the diffusion coefficients found from the data presented in Fig. 7 for spectral regions characteristic of the strong influence of glycerol, as an OCA,  $D_{Gly} = (5.8 \pm 0.6)10^{-7} - (6.0 \pm 0.5)10^{-7} \text{ cm}^2/\text{s}$ , and the ICG bands,  $D_{ICG} = (5.8 \pm 0.6)10^{-7} \text{ cm}^2/\text{s}$ , turned out to be close to each other. This may indicate that glycerol and ICG form a molecular complex and move as a single complex in the tissue.

In conclusion, the study demonstrated the potential of fluorescence imaging and MRI to label and visualize ester copolymers *in vitro* and *in vivo*. It was found that hydrolysis is the predominant degradation mechanism in buffer solutions and contributes to enzyme-mediated cleavage. In fetal serum, the presence of proteins slows down biodegradation compared to the buffer. Fluorescent and paramagnetic labels were released in two phases, with the weight of the copolymers correlating with the release. MRI and fluorimetry were used to assess polymer biodegradation *in vitro*

and *in vivo*, providing valuable insights into the degradation process, structural changes, and release of labels and degradation products. These methods contribute to a better understanding of the behavior of copolymer materials in biomedical applications, leading to improved predictability and effectiveness of biomedical devices.

In the course of experimental studies, using collimated transmittance spectroscopy, the diffusion rate of one of the degradation products of implants, such as glycerol, as well as the dye-label of the implant, ICG, was measured in *ex vivo* muscle tissue.

### Acknowledgments

We acknowledge Prof. Alexei Bogdanov (University of Massachusetts Medical School, Radiology, Worcester, Massachusetts, USA) for the concept of this study and for the advice. We acknowledge Prof. Savitsky and his lab (Laboratory of physical biochemistry of RC of Biotechnology of the RAS) for providing fluorescence imaging facilities for the *in vivo* experiments. Fibroblast-like cell line A9 and myoblast-like cell line C2C12 were obtained from the Shared Research Facility “Vertebrate cell culture collection” (Institute of cytology of the RAS, S-Peterburg, Russia).

### Funding

This research was funded by Ministry of Science and Higher Education of the Russian Federation grant № 13.2251.21.0009 from 29.09.2021 (Agreement № 075-15-2021-942).

### REFERENCES

- [1] L. N. Woodard and M. A. Grunlan, “Hydrolytic Degradation and Erosion of Polyester Biomaterials,” *ACS Macro Letters*, vol. 7, no. 8. American Chemical Society, pp. 976–982, 2018.
- [2] B. S. Heidari *et al.*, “A novel biocompatible polymeric blend for applications requiring high toughness and tailored degradation rate,” *J Mater Chem B*, vol. 9, no. 10, pp. 2532–2546, 2021.
- [3] M. R. A. V. and R. A. V. Zambrano, J. Pawlak, and R. Venditti, “Effects of Chemical and Morphological Structure on Biodegradability of Fibers, Fabrics, and Other Polymeric Materials,” *Bioresources*, vol. 15, no. 4, pp. 9786–9833, 2020.
- [4] L. Palanikumar *et al.*, “Spatiotemporally and sequentially-controlled drug release from polymer gatekeeper-hollow silica nanoparticles,” *Sci Rep*, vol. 7, 2017.
- [5] M. Timusk *et al.*, “Study of triboelectric properties and biocompatibility of some selected polyesters: Toward implantable triboelectric nanogenerator devices,” *Polymer (Guildf)*, vol. 281, p. 126088, 2023.
- [6] C. Kleber, K. Lienkamp, J. Rühle, and M. Asplund, “Electrochemically Controlled Drug Release from a Conducting Polymer Hydrogel (PDMAAp/PEDOT) for Local Therapy and Bioelectronics,” *Adv Healthc Mater*, vol. 8, no. 10, 2019.
- [7] R. S. Petersen, L. H. Nielsen, T. Rindzevicius, A. Boisen, and S. S. Keller, “Controlled drug release from biodegradable polymer matrix loaded in microcontainers using hot punching,” *Pharmaceutics*, vol. 12, no. 11, pp. 1–13, 2020.
- [8] X. Fu, L. Hosta-Rigau, R. Chandrawati, and J. Cui, “Multi-Stimuli-Responsive Polymer Particles, Films, and Hydrogels for Drug Delivery,” *Chem*, vol. 4, no. 9. Elsevier Inc, pp. 2084–2107, 2018.
- [9] W. R. Gombotz and D. K. Pettit, “Biodegradable Polymers for Protein and Peptide Drug Delivery,” 1995.
- [10] M. Levitus and S. Ranjit, “Cyanine dyes in biophysical research: The photophysics of polymethine fluorescent dyes in biomolecular environments,” *Q Rev Biophys*, vol. 44, no. 1, pp. 123–151, 2011.
- [11] Y. Guo *et al.*, “Bioactive biodegradable polycitrate nanoclusters enhances the myoblast differentiation and *in vivo* skeletal muscle regeneration via p38 MAPK signaling pathway,” *Bioact Mater*, vol. 5, no. 3, pp. 486–495, 2020.
- [12] M. Attia *et al.* “Optical properties of indocyanine green under ultrasound treatment” *J. Photochem. Photobiol.*, vol. 2, 2020.
- [13] V.V. Tuchin, D. Zhu, and E.A. Genina (Eds.), *Handbook of Tissue Optical Clearing: New Prospects in Optical Imaging*, Taylor & Francis Group LLC, CRC Press, Boca Raton, FL, 2022.
- [14] Tuchina D. K., Shi R., Bashkatov A. N., Genina E.A., Zhu D., Luo Q., Tuchin V.V. Ex vivo optical measurements of glucose diffusion kinetics in native and diabetic mouse skin, *J. Biophotonics* **8** (4), p. 332–346, 2015.
- [15] D.K. Tuchina, I.G. Meerovich, O.A. Sindeeva, V. V. Zherdeva, A. P. Savitsky, A. A. Bogdanov Jr, V. V. Tuchin, Magnetic resonance contrast agents in optical clearing: Prospects for multimodal tissue imaging, *J. Biophotonics* **13** (11), 2020.

## THREE-DIMENSIONAL VIRTUAL OPTICAL CLEARING FOR HIGH-THROUGHPUT DEEP TISSUE IMAGING

JIAJIA CHEN<sup>1,3</sup>, YAO ZHENG<sup>1,3</sup>, WEI GONG<sup>1,3</sup> AND KE SI<sup>1,2,3</sup>

<sup>1</sup>*School of Brain Science and Brain Medicine, Zhejiang University School of Medicine, China*

<sup>2</sup>*College of Optical Science and Engineering, Zhejiang University, China*

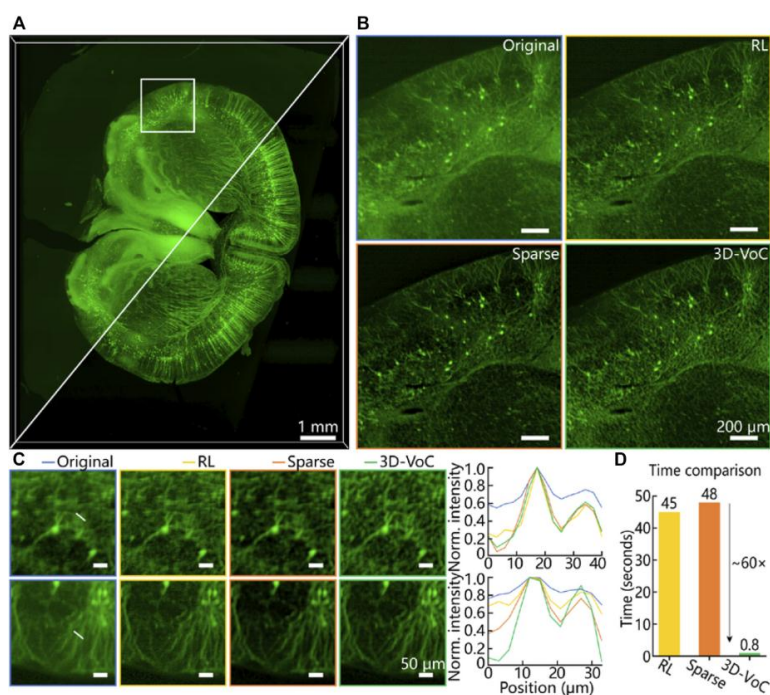
<sup>3</sup>*Liangzhu Laboratory, MOE Frontier Science Center for Brain Science and Brain-machine Integration,*

*State Key Laboratory of Brain-machine Intelligence, Zhejiang University, China*

kesi@zju.edu.cn

### ABSTRACT

High-throughput deep tissue imaging and chemical tissue clearing protocols have brought out great promotion in biological research. However, due to uneven transparency introduced by tissue anisotropy in imperfectly cleared tissues, fluorescence imaging based on direct chemical tissue clearing still encounters great challenges, such as image blurring, low contrast, artifacts and so on. Here we reported a three-dimensional virtual optical clearing method based on unsupervised cycle-consistent generative adversarial network, termed 3D-VoCycleGAN, to digitally improve image quality and tissue transparency of biological samples. We demonstrated the good image deblurring and denoising capability of our method on imperfectly cleared mouse brain and kidney tissues. With 3D-VoCycleGAN prediction, the signal-to-background ratio (SBR) of images in imperfectly cleared brain tissue areas also showed above 40% improvement. Compared to other deconvolution methods, our method could evidently eliminate the tissue opaqueness and restore the image quality of the larger 3D images deep inside the imperfect cleared biological tissues with higher efficiency. And after virtually cleared, the transparency and clearing depth of mouse kidney tissues were increased by up to 30%. To our knowledge, it is the first interdisciplinary application of the CycleGAN deep learning model in the 3D fluorescence imaging and tissue clearing fields, promoting the development of high-throughput volumetric fluorescence imaging and deep learning techniques.



### REFERENCES

- [1] J. Chen, Z. Du, and K. Si, "Three-Dimensional Virtual Optical Clearing with Cycle-Consistent Generative Adversarial Network," *Frontiers in Physics* 10 (2022).
- [2] J. Chen, Z. Du, C. Xu, X. Xiao, W. Gong, and K. Si, "Ultrafast 3D histological imaging based on a minutes-time scale tissue clearing and multidirectional selective plane illumination microscopy," *Optics letters* 47, 4331-4334 (2022).
- [3] X. Zhu, L. Huang, Y. Zheng, Y. Song, Q. Xu, J. Wang, K. Si, S. Duan, and W. Gong, "Ultrafast optical clearing method for three-dimensional imaging with cellular resolution," *PNAS* 116, 11480-11489 (2019).

## REFRACTOMETRIC ANALYSIS OF BLOOD SERUM

LUDMILA PLOTNIKOVA<sup>1</sup>, OLGA VEZO<sup>1</sup>, ANDREY GARIFULLIN<sup>1,2</sup>, ALEKSEY KUVSHINOV<sup>2</sup>, SERGEY VOLOSHIN<sup>2,3,4</sup> AND ALEXANDER POLYANICHKO<sup>1,5</sup>

<sup>1</sup>*St. Petersburg State University, Russia*

<sup>2</sup>*Russian Research Institute of Hematology and Transfusiology, Russia*

<sup>3</sup>*Kirov Military Medical Academy, Russia*

<sup>4</sup>*Mechnikov Northwestern State Medical University, Russia*

<sup>5</sup>*Institute of Cytology of the Russian Academy of Sciences, Russia*

[ljusja@mail.ru](mailto:ljusja@mail.ru)

### ABSTRACT

Refractometric analysis is based on measuring the refractive index of samples in various state. When working with biological fluids, refractometry is a fast and fairly accurate alternative to the biochemical analysis of certain parameters, in particular, the total protein of blood serum. Serum contains dissolved substances in concentrations of 80-100 g/l, most of which are proteins. Serum refractometry assumes that the concentration of inorganic electrolytes and non-protein organic compounds does not change significantly from sample to sample, and differences in refractive index primarily reflect differences in protein concentrations.

The dependence of the refractive index of blood serum and its main protein components on temperature was studied using an Abbemat WR/MW refractometer (Anton Paar, Austria) in the temperature range of 15–45°C. The presence of a temperature dependence of the refractive index of both model systems and blood serum samples was shown. The paper discusses the applicability of the approach for the comparative analysis of blood serum samples from healthy donors and patients with oncohematological diseases.

Multiple myeloma (MM) is a disease of the hematopoietic system in which a monoclonal (one type) protein related to immunoglobulins (Mprotein) and (or) its light chains are synthesized, which are found in blood serum and (or) urine, rarely only in the cytoplasm clonal cells. MM is included in 1% of all malignant tumors and makes up just over 10% of all hematological malignancies; today it is considered incurable [1]. Recently, much attention has been paid to the development and use of various rapid methods for determining the protein composition of biological samples, including for the diagnosis of MM [2 - 4]. In some cases, as, for example, when determining multiple myeloma, it is necessary to obtain a reliable estimate of the amount of certain components in the composition of the biological material. Refractometric analysis in such a situation has a number of advantages, such as simplicity, short time and high accuracy of analysis.

The work studied the differences in the refractive indices of blood serum from healthy people and patients with multiple myeloma before and after a course of therapy using an Abbemat 200 refractometer (Anton Paar, Austria). We used blood serum samples from 14 patients of both sexes aged from 42 to 78 years with a diagnosis of stage II-III multiple myeloma, under the supervision of the hematology clinic of the Russian Research Institute of Hematology and Transfusiology, as well as control blood serum samples from 55 healthy blood donors. Serum samples after completion of the first course of antitumor therapy were collected from 8 of 14 patients.

Figure 1 shows the results of measuring the amount of protein in a sample depending on the refractive index of all studied samples. It can be noticed that all the points on the diagram are grouped in two areas. The area located at the bottom of the diagram contains samples from healthy donors, while the points corresponding to patients with MM before treatment are grouped at the top of the diagram. The results obtained indicate that, on average, both studied parameters, the refractive index and the amount of protein, are higher in the blood serum of patients with MM than in healthy donors. The latter is in good agreement with the data of biochemical and immunological analysis of the samples.

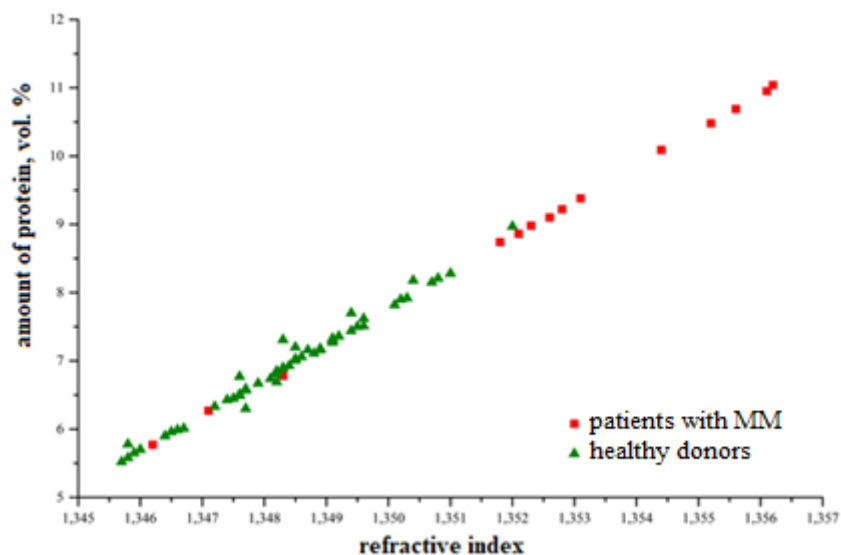


**Figure 1.** Results of measuring the amount of protein in a sample depending on the refractive index of all studied samples.

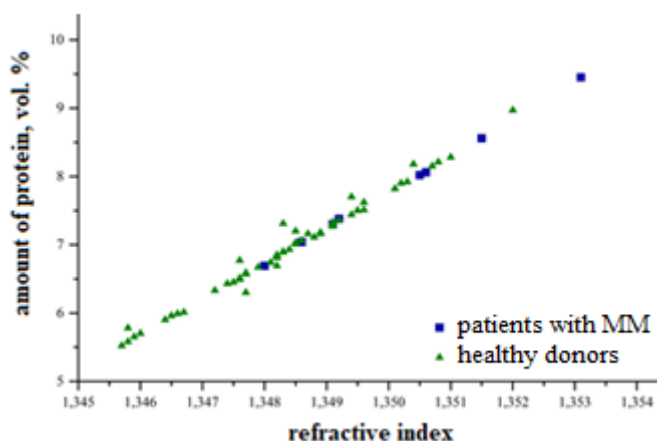


**Figure 2.** Results of measuring the amount of protein in a sample depending on the refractive index of patients with MM after the first course of antitumor therapy.

In Figure 2 there is a tendency towards a decrease in the amount of protein in the blood serum and, as a consequence, the refractive index in patients with MM who have undergone the first course of antitumor therapy, despite the persistence of significant differences between these patients and healthy donors.

Thus, we can conclude that refractometric analysis allows monitoring changes in protein concentration and refractive index of the blood serum of patients with MM, while combining simplicity, accuracy and high speed of analysis. Based on the data obtained, refractometry can be considered a promising method for studying samples of this type.

#### ACKNOWLEDGEMENTS

Investigations were carried out using the equipment of resource center "Center for Diagnostics of Functional Materials for Medicine, Pharmacology and Nanoelectronics" of Scientific Park of St. Petersburg State University.

#### REFERENCES

- [1] M. Gertz, S. Rajkumar, Multiple Myeloma. Diagnosis and Treatment, NY: Springer, p. 311, 2014.
- [2] L. Plotnikova, A. Polyanichko, T. Nosenko, M. Uspenskaya, A. Garifullin, S. Voloshin, Characterization of the infrared spectra of serum from patients with multiple myeloma, AIP Conference proceedings, v. 1760, 020052-1–020052-4, 2016.
- [3] E.A. Telnaya, L.V. Plotnikova, A.D. Garifullin, A.Yu. Kuvshinov, S.V. Voloshin, A.M. Polyanichko, Infrared Spectroscopy of Blood Serum from Patients with Oncohematological Diseases, Biophysics, v. 65 (6), 981–986, 2020.  
L.V. Plotnikova, M.O. Kobeleva, E.V. Borisov, A.D. Garifullin, A.V. Povolotskaya, S.V. Voloshin, A.M. Polyanichko, Infrared Spectroscopy of Blood Serum from Patients with Multiple Myeloma, Cell and Tissue Biology, 13(2), 130-135, 2019.

## INVESTIGATION OF THE EFFECT OF PROLONGED EXPOSURE TO OCA-AEROSOL (GLYCERIN/PROPYLENE GLYCOL) ON RAT PLASMA BY RAMAN SPECTROSCOPY

ARINA SOKOVA<sup>1</sup>, EKATERINA LAZAREVA<sup>1,2</sup>, ALEXANDER POLOZHENKOV<sup>3</sup>, ARTEM MYLNIKOV<sup>3</sup>, ALLA BUCHARSKAYA<sup>1,2,3</sup> AND VALERY TUCHIN<sup>1,2,4</sup>

<sup>1</sup> *Scientific and Educational Institute of Optics and Biophotonics, Saratov State University, Russia*

<sup>2</sup> *Interdisciplinary Laboratory of Biophotonics, National Research Tomsk State University, Russia*

<sup>3</sup> *Department of Pathological Anatomy, Saratov State Medical University, Russia*

<sup>4</sup> *Laboratory of problems of laser diagnostics of technical and living systems Institute of Precision Mechanics and Control RAS, Russia*

sokova.2001@mail.ru

### ABSTRACT

Current problem of our time is the replacement of tobacco smoking with the use of devices with steam smoking mixtures. However, scientists have already proved that their use also has a negative effect on the human body causing irreversible changes [1-5]. Raman spectroscopy (RAMAN) is one of the methods that allows analyzing the molecular composition of a substance, in particular blood and plasma [6-7]. Various blood components have a significant effect on the Raman spectra [8-9]. The blood serum obtained after the separation of whole blood into fractions contains almost 90% water, about 6.6–8.5% proteins and other organic and mineral compounds, which are intermediate or final products of metabolism carried by blood.

The experiment was carried out using 14 female white laboratory rats of the Wistar line (weight  $180 \pm 30$  g, aged 9 months). The animals were randomly selected and divided into 2 groups: 1 - control group (without exposure); 2 - group with inhalation exposure to an OCA aerosol POD system. The content of glycerol and propylene glycol in the liquid intended for filling the POD system was 50/50%.

The impact of the POD system on rats was carried out using a specially designed installation, which is: a glass container with a volume of 0.003 m<sup>3</sup> with two holes: the first hole for connecting the POD system, the second for the Janet syringe. The duration of one inhalation averaged 5-7 minutes, the total number of inhalations was 5 per day. The rest period of laboratory rats after one manipulation was 15 minutes. The animals were removed from the experiment on day 14. Excretion was carried out by decapitation, with the preliminary introduction of the dissociative injectable anesthetic Zoletil100. After that, blood sampling was performed.

The blood of laboratory rats was centrifuged for 15 minutes at 2000 rpm, after which blood plasma was taken and poured into separate test tubes. As a result, six blood plasma samples were obtained for the control group) and six samples for the group with inhalation exposure to OCA-aerosol (14 days).

To register the Raman spectra, hardware was used consisting of a spectrometer (Ocean Optics, QE65000), a diode laser (785 nm, laser energy 400 mw), a hand RAMAN probe ( $f = 7.5$  mm) and a computer.

The RAMAN spectra after the analysis for the presence of peaks for the control group and the group of animals after exposure to OPA-aerosol are shown in Figure.

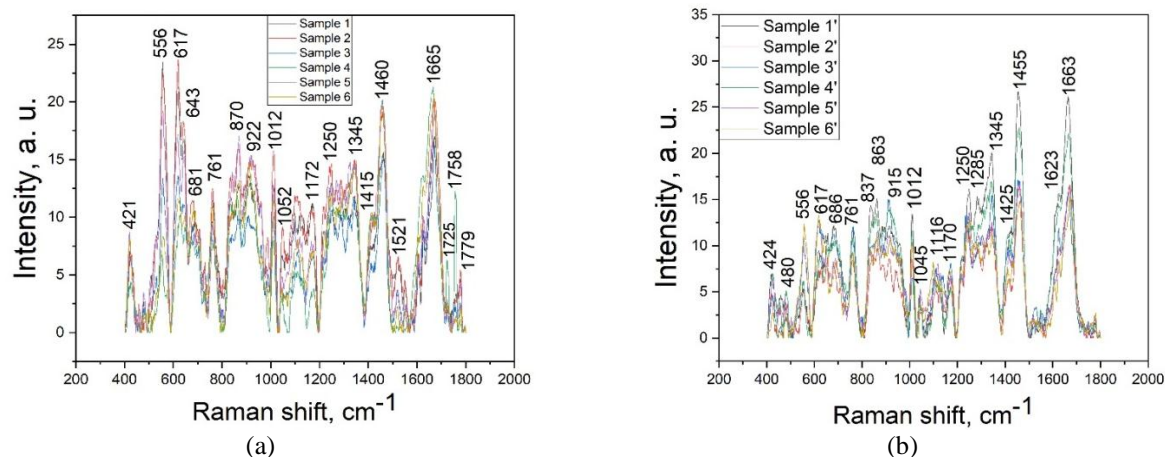


**Figure:** Raman spectrum for six samples of the control group (a) and the group exposed to inhalation effects of OCA - aerosol (b)

The central position of the peaks was determined from the Raman spectra. Data for each of the groups are given in Table. To assess the impact of OCA, the impact efficiency coefficient was calculated  $E_{OC}$ :

$$E_{OC} = \frac{I_{oca} - I_{control}}{I_{control}} \times 100\%,$$

where  $I_{oca}$  – is the intensity of the selected line of the RAMAN spectrum for a group of animals after exposure to an OCA-aerosol,  $I_{control}$  – is the intensity of the selected line of the RAMAN spectrum for the control group.

The results after averaging the data by groups are shown in Table and show by how many percent the intensity of RAMAN on the spectrum increased or decreased for the group exposed to inhalation effects of POD-systems aerosol relative to the intensity of the RAMAN spectrum for the control group. Since the resolution of the device is  $10 \text{ cm}^{-1}$ , differences in the position of the peaks by a large amount may indicate possible changes in the molecular structure.

**Table:** Characteristics of RAMAN spectra for the control group and the group of animals exposed to inhalation effects of OPA -aerosol

Control group		The group after the OPA-aerosol		$E_{OC}$ , %	Component	Raman shift, $\text{cm}^{-1}$	Ref.
Raman shift, $\text{cm}^{-1}$	Intensity, a.u.	Raman shift, $\text{cm}^{-1}$	Intensity, a.u.				
422.85	6.30	422.85	4.94	-21.55	Histidine	422	[11]
558.58	14.57	553.98	7.64	-47.55	Uracil	556	[11]
620.18	15.36	622.44	10.21	-33.54	Glutathione	625	[11]
642.74	13.08	651.73	9.24	-29.41	Tyrosine	643	[10]
725.06	4.10	--	--	--	Acetyl coenzyme A	724	[11]
837.75	11.08	839.88	10.39	-6.18	Tyrosine	830	[10]
867.50	12.95	861.15	11.53	-10.94	D-(+)-Mannose	861	[11]
--	--	892.81	9.88	--	Palmitic acid	893	[11]
911.67	13.21	913.76	11.65	-11.78	D-(+)-Trehalose	912	[11]
982.02	4.70	--	--	--	Arginine	982	[11]
1010.58	11.25	1010.58	9.43	-16.23	Phenylalanine	1003	[10]
1046.96	4.83	--	--	--	Tryptophan	1046	[11]
1063.00	4.14	--	--	--	Palmitic acid	1063	[11]
1102.78	7.87	--	--	--	D-(+)-Trehalose	1102	[11]
1173.22	7.58	1171.28	6.12	-19.23	Stearic acid	1173	[11]
1272.36	10.73	--	--	--	Histidine	1271	[11]
1342.91	13.29	1342.91	14.31	7.70	Hydrophobicity marker for tryptophan	1340	[10]
1458.23	17.89	1458.23	18.74	4.72	D-Fructose-6-phosphate	1458	[11]
1608.2	6.85	--	--	--	Phenylalanine	1609	[10]
1626.62	10.25	1624.95	11.09	8.16	Amide	1630-1635	[10]
1669.68	18.65	1668.04	18.15	-2.69		1660-1670	[10]

According to the results obtained, it can be noted that the number of peaks in the intensity of the RAMAN spectrum in the group exposed to the OCA - aerosol significantly decreased in comparison with the control group. However, the group after the OCA - aerosol had one peak, which is missing from the reference group: this is the peak of intensity located at a RAMAN shift equal to  $892 \text{ cm}^{-1}$ , which according to the literature data may correspond to the RAMAN band of palmitic acid [11].

The positions of the centers of most peaks have shifted slightly, but there are RAMAN bands that have not changed their position on the frequency scale. This phenomenon is observed at the RAMAN shifts equal to: 422.85, 1010.58, 1217.44, 1342.91, 1415.5 and  $1458.23 \text{ cm}^{-1}$ .

A significant decrease in the intensity of RAMAN by 47.5% is observed in the band characteristic of uracil  $556 \text{ cm}^{-1}$ , and in the experiment a change in the position of the center of this peak from 553 to  $559 \text{ cm}^{-1}$  is noted [11].

*The reported study was funded by a grant under the Decree of the Government of the Russian Federation No. 220 of 09 April 2010 (Agreement No. 075-15-2021-615 of 04 June 2021)*

## REFERENCES

- [1] J. Didkowska, U. Wojciechowska, M. Manczuk, J. Lobaszewski, Lung cancer epidemiology: contemporary and future challenges worldwide, *Ann. Transl. Med.* 4, 150, 2016.

- [2] M.I. Restrepo, J.D. Chalmers, Y. Song, C. Mallow, J. Hewlett, F. Maldonado, L. Yarmus, Year in review 2016: respiratory infections, acute respiratory distress syndrome, pleural diseases, lung cancer and interventional pulmonology, *Respirology* 22, 602–611, 2017.
- [3] D. Zhu, K.V. Larin, Q. Luo, V.V. Tuchin, Recent progress in tissue optical clearing, *Laser & Photonics Reviews*, 7(5), 732–757, 2013.
- [4] V.V. Tuchin, Tissue optics and photonics: Light-tissue interaction, *Journal of Biomedical Photonics & Engineering* 1, 98–134, 2015.
- [5] A.A. Sokova, E.N. Lazareva, A.B. Bucharskaya, V.V. Tuchin, Study of the optical properties of blood plasma with the addition of solutions of glycerin and propylene glycol using Raman spectroscopy, Interaction of microwave, terahertz and optical radiation with semiconductor micro- and nanostructures, metamaterials and biological objects: Collection of articles of the ninth All-Russian school-seminar, Saratov: Saratov Source, 254-257, 2022.
- [6] Q. Lin, E.N. Lazareva, V.I. Kochubey, Y. Duan, V.V. Tuchin, Kinetics of optical clearing of human skin studied in vivo using portable Raman spectroscopy, *Laser Physics Letters* 17, 105601, 2020
- [7] A.A. Mankova, O.P. Cherkasova, E.N. Lazareva, A.B. Bucharskaya, P.A. Dyachenko, Yu.V. Kistenev, D.A. Vrazhnov, V.E. Skiba, V.V. Tuchin, A.P. Shkurinov, Study of blood serum in rats with transplanted cholangiocarcinoma using raman Spectroscopy, *Optics and Spectroscopy* 128(7), 964–971, 2020.
- [8] V.N. Grishanov, Raman spectroscopy in medical diagnostics [Electronic resource], Samara: SSAU Publishing House, 2015.
- [9] Yu.A. Khristoforova, I.A. Bratchenko, D.N. Artemyev, O.O. Myakinin, A.A. Moryatov, O.I. Kaganov, S.V. Kozlov, V.P. Zakharov, Optical diagnosis of malignant and benign skin tumors, *Information technologies and nanotechnologies*, 265-268, 2017.
- [10] N. Kuhar, S. Sil, T. Verma, S. Umopathy, Challenges in application of Raman spectroscopy to biology and materials, *The Royal Society of Chemistry* 8, 25888–25908, 2018.
- [11] J.D. Gelder, K.D. Gussem, P. Vandenabeele, L. Moens Reference database of Raman spectra of biological molecules, *Journal of Raman spectroscopy* 38, 1133–1147, 2007.

## UPCONVERSION SUPER-RESOLUTION MICROSCOPY

QIUQIANG ZHAN\*

South China Academy of Advanced Optoelectronics, South China Normal University, Guangzhou, P. R. China

zhanqiuqiang@m.scnu.edu.cn

## ABSTRACT

The optical microscopy resolution is limited by the physics of diffraction,  $d=\lambda/2n\sin\theta$ . The N-photon microscopy can theoretically improve resolution,  $d=\lambda/(2n\sin\theta N^{1/2})$ . However, this is a paradox that higher N always means longer  $\lambda_{ex}$ . To break this limit, we proposed 730-nm CW laser excited 4-photon microscopy with Nd-sensitized UCNPs, obtaining 161-nm sub-diffraction resolution[1]. Photon avalanche (PA) occurring in lanthanide-doped solids is a very important mechanism, which can arouse a giant nonlinear response in the luminescence intensity to the excitation light intensity, while not relying on intense laser pulses as in traditional nonlinear optical processes. The achievement of PA, mostly restricted to bulk materials, conventionally relies on very sophisticated excitation schemes, individual for each PA system. Recently, we established a universal PA strategy to generate huge optical nonlinearities from various lanthanide emitters, i.e., migrating photon avalanche (MPA) based on multilayer core-shell nanomaterials[2]. The core of a MPA nanoparticle is the key to activating avalanche looping cycles, where PA are synchronously achieved for both  $Yb^{3+}$  and  $Pr^{3+}$  ions under 852-nm laser excitation, exhibiting a 26<sup>th</sup> order nonlinearity and a clear pumping threshold. The avalanching  $Yb^{3+}$  ions can migrate their optical nonlinear response in a long range to other emitters (e.g.,  $Ho^{3+}$  and  $Tm^{3+}$ ) located in the subsequent shell layer, resulting in an even higher order nonlinearity due to a further cascading multiplicative effect (as high as 46<sup>th</sup> for  $Tm^{3+}$ ). As a demonstration, using one low-power, 852-nm CW beam, we implemented nanoscopy with a lateral resolution down to 62 nm. Our strategy provides a facile route to achieve a giant optical nonlinearity in different nano-emitters, which holds great potential for widespread applications.

Stimulated emission depletion (STED) microscopy has become a powerful diffraction-unlimited technique for fluorescence imaging with resolution governed by  $d=\lambda/(2n\sin\theta(1+I/I_{sat})^{1/2})$ . However, STED fundamentally suffers from high-intensity light illumination, photobleaching, re-excitation background, sophisticated probe-defined laser schemes, and limited photon budget of the probes. In 2015, we realized emission depletion in UCNPs[3]. In 2017, using UCNPs we developed low-power CW laser enabled nonbleaching cytoskeleton STED imaging[4,5]. In our very recent progress, we have successfully broken the theoretical limit of saturation intensity itself by two orders using new mechanism, and provides background-free, contrast-enhanced imaging at  $\lambda_{ex}/38$  resolution. We demonstrate a versatile strategy, stimulated-emission induced excitation depletion (STExD), to deplete the emission of multi-chromatic probes using a single pair of low-power, NIR CW lasers with fixed wavelength. With the effect of cascade amplified depletion effects, we achieve emission depletion for a wide range of emitters by manipulating their common sensitizer. We demonstrate an ultrahigh depletion efficiency of 99.3% for the 450 nm emission with a record low saturation intensity of 23.8 kW cm<sup>-2</sup>[6]. We further demonstrate nanoscopic imaging with a series of multi-chromatic nanoprobe, two-color STExD imaging, and subcellular imaging of the immunolabelled actin filaments [7].

## REFERENCES

- [1] Wang, B., et al., Visible-to-visible four-photon ultrahigh resolution microscopic imaging with 730-nm diode laser excited nanocrystals. *Optics Express*, 2016. 24(2): p. A302-A311.
- [2] Liang, Y., et al., Migrating photon avalanche in different emitters at the nanoscale enables 46th-order optical nonlinearity. *Nature Nanotechnology*, 2022. 17(5): p. 524-530.
- [3] Wu, R., et al., Optical depletion mechanism of upconverting luminescence and its potential for multi-photon STED-like microscopy. *Optics Express*, 2015. 23(25): p. 32401-32412.
- [4] Zhan, Q., et al., Achieving high-efficiency emission depletion nanoscopy by employing cross relaxation in upconversion nanoparticles. *Nature Communications*, 2017. 8(1): p. 1058.
- [5] Peng, X., et al., Fast upconversion super-resolution microscopy with 10  $\mu$ s per pixel dwell times. *Nanoscale*, 2019. 11(4): p. 1563-1569.
- [6] Guo, X., et al., Achieving low-power single-wavelength-pair nanoscopy with NIR-II continuous-wave laser for multi-chromatic probes. *Nature Communications*, 2022. 13(1): p. 2843.
- [7] Pu, R., et al., Super-resolution microscopy enabled by high-efficiency surface-migration emission depletion. *Nature Communications* 2022, 13 (1), 6636.

## SHINING TO TRADITIONAL MEDICINE

TING LI

*Institute of Biomedical Engineering, Chinese Academy of Medical Sciences & Peking Union Medical College, China*

liting@bme.cams.cn

### ABSTRACT

Traditional Chinese Medicine (TCM) has a long-standing history of employing therapies like acupuncture and cupping for treating various ailments such as knee pain, lower back pain, and stress urinary incontinence. Despite its widespread use, the physiological basis of these therapies remains relatively underexplored. To address this gap, this study integrates near-infrared spectroscopy (NIRS) in both acupuncture and cupping therapies to provide real-time physiological observations, thus demystifying these "black box" models.

We designed hollow NIRS probes with dual detection channels for real-time measurements during acupuncture at specific acupoints like "Xuehai." The probes recorded significant and consistent increases in oxy-hemoglobin (HbO), deoxy-hemoglobin (Hb), and total blood volume (HbT) around the acupoint during treatment, which reverted to baseline after needle removal. This indicates that acupuncture induces tissue vasodilation and enhances oxygen consumption, shedding light on its underlying mechanisms. A subject fainted during an acupuncture experiment, with recorded hemodynamic alterations showing a significant increase in Hb and decrease in HbO, indicating tissue deoxidization about 1 minute before fainting. This suggests that NIRS may have potential as an early predictor of fainting. Our NIRS probes can be integrated with laser acupuncture, thereby achieving a unified approach to diagnosis and treatment.

For cupping therapy, leveraging the Visible Chinese Human dataset and 3D Monte Carlo modeling, we developed a specialized NIRS instrument integrated into the cupping cup and a second external probe encircling the treatment area. Our device facilitated real-time tracking of changes HbO, Hb, and HbT during and post-treatment. In vivo experiments revealed significant hemodynamic alterations adjacent to and within the cupping site, implying blood oxygen redistribution. Our experiment included cupping on the shoulder blade and lower back. The results from the lower back cupping experiment showed a significant difference in blood oxygen changes between patients with lower back pain and healthy individuals, demonstrating the potential of this technology in the clinical application of cupping.

Our innovative NIRS-based apparatuses hold promise for elucidating the physiological mechanisms underpinning acupuncture and cupping. Moreover, they offer real-time monitoring capabilities that could enable adjustments during therapy, potentially improving treatment efficacy. This groundbreaking study not only augments our understanding of TCM but also pioneers new interdisciplinary avenues—specifically, TCM photonics.

## TISSUE OPTICAL CLEARING FOR WHOLE-ORGAN IMAGING

TINGTING YU<sup>1</sup>

<sup>1</sup> *Britton Chance Center for Biomedical Photonics - MoE Key Laboratory for Biomedical Photonics, Advanced Biomedical Imaging Facility-Wuhan National Laboratory for Optoelectronics, Huazhong University of Science and Technology, Wuhan, Hubei 430074, China*  
yutingting@hust.edu.cn

### ABSTRACT

Acquiring the three-dimensional (3D) structure of biological tissues is essential for research in life sciences. Modern optical imaging techniques and fluorescent labeling technologies have provided vital tools for obtaining high-resolution information on the 3D structures of biological tissues. However, the turbid nature of biological tissues limits the depth of light penetration, leading to restricted applications for large tissues or whole organs. Tissue optical clearing technology takes a different approach by making the tissues transparent using various physical and chemical strategies to reduce the attenuation of light in tissues, and providing a new approach for the 3D imaging of whole tissue organs. Here, we will introduce our progress in the research of tissue optical clearing methods and applications, covering the fluorescence labeling, tissue clearing, and imaging of large tissues/whole organs.

### REFERENCES

- [1] Qi Y, Yu T, Xu J, Wan P, Ma Y, Zhu J, et al. FDISCO: Advanced solvent-based clearing method for imaging whole organs. *Science Advances*. 2019;5(1):eaau8355.
- [2] Zhu J, Yu T, Li Y, Xu J, Qi Y, Yao Y, et al. MACS: Rapid aqueous clearing system for 3D mapping of intact organs. *Advanced Sciences*. 2020;7(8):1903185.
- [3] Zhu J, Liu X, Xu J, Deng Y, Wang P, Liu Z, et al. A versatile vessel casting method for fine mapping of vascular networks using a hydrogel-based lipophilic dye solution. *Cell Reports Methods*. 2023;3(2):100407.

## THE NEAR-INFRARED-II FLUORESCENCE IMAGING PROBES FOR SURGICAL NAVIGATION

MING WU<sup>1</sup>, XIAOLONG LIU<sup>1</sup>

*Mengchao Hepatobiliary Hospital of Fujian Medical University, Fujian Fuzhou, P. R. China*

*xiaoloong.liu@gmail.com*

### ABSTRACT

Fluorescence surgical navigation technology depends on fluorescence imaging system and fluorescence probe to display focus information more accurately during operation. Currently, the fluorescent surgical navigation probes approved for clinical use include sodium fluorescein, 5-aminolevulinic acid (5-ALA), methylene blue (MB) and indocyanine green (ICG). However, the excitation and emission wavelengths of sodium fluorescein, 5-ALA and MB locate in the 400-700nm region. As a result, the penetration depth is very limited, only tissue surface imaging can be performed, and the signal-to-noise ratio is also very low. Therefore, the application of these probes in surgical navigation has been gradually eliminated in clinic. In order to obtain deeper tissue penetration depth and carry out more accurate fluorescence imaging and surgical navigation, it is necessary to use near-infrared fluorescence probes with longer excitation and emission wavelengths. Indocyanine green (ICG) is currently the most widely used and thoroughly studied near-infrared fluorescence molecular probe in fluorescence surgical navigation. ICG, which was first synthesized by Kodak Laboratory in Japan in 1955, can be excited by light at the wavelength of 750 ~ 810nm and emit near-infrared light with the maximum wavelength of 830nm. The near infrared fluorescence surgical navigation technique based on ICG has been widely used in the field of tumor surgery, and many clinical studies have confirmed its clinical value in the aspects of surgical thoroughness, surgical convenience, recurrence-free survival, and total survival. However, NIR-I fluorescence imaging still has a series of inherent bottlenecks, such as low penetration depth, high background signal, poor signal-to-noise ratio and so on. In recent years, with the deepening of NIR-II fluorescence imaging research and the rapid development of nanotechnology, a series of organic small molecules, organic nano-probes and inorganic nano-probes have been developed and applied as NIR-II fluorescent molecular probes in the fields of fluorescence imaging and surgical navigation. We will present the recent developed NIR-II fluorescence imaging probes for surgical navigation in our group.

## EFFECT OF THE DOSE OF UPCONVERSION NANOPARTICLES ON THE REFRACTIVE INDEX OF TISSUES IN THE DEVELOPMENT OF MODEL LIVER CANCER

EKATERINA LAZAREVA<sup>1,2</sup>, ROMAN ANISIMOV<sup>1</sup>, MARIA LOMOVA<sup>1</sup>, ANNA DORONKINA<sup>1</sup>, ARTEM MYLNIKOV<sup>3</sup>, NIKITA NAVOLOKIN<sup>3</sup>, VYACHESLAV KOCHUBEY<sup>1</sup> AND IRINA YANINA<sup>1,2</sup>

<sup>1</sup>*Scientific and Educational Institute of Optics and Biophotonics, Saratov State University, Russia*

<sup>2</sup>*Interdisciplinary Laboratory of Biophotonics, National Research Tomsk State University, Russia*

<sup>3</sup>*Department of Pathological Anatomy, Saratov State Medical University, Russia*

lazarevaen@list.ru

### ABSTRACT

Upconversion nanoparticles(UCNP) play an important role in the application of photodynamic therapy, which helps to treat malignant tumors with high efficiency [1, 2]. Since the development of pathology changes the structure and composition of biological tissues, and, consequently, their optical properties undergo significant changes, several research groups have proposed using the refractive index, as one of the main optical parameters, as a marker for differentiating normal and pathological biological tissue, including experimental diabetes in animals [3]. Also, the refractive index is an important optical characteristic that is necessary for a complete description of the optical properties of biological tissues.

The presented study was carried out on white mature Wistar rats, according to the method described in the article [4]. When conducting experiments on animals, accepted international ethical standards were observed [5]. The study modeled the development of alveolar liver cancer (cholangiocarcinoma, PC1) by injecting 0.5 ml of a 25% tumor suspension in Hanks solution subcutaneously into the scapula area. Animals were removed from the experiment on day 28 after tumor implantation. Laboratory animals with transplanted liver tumors were injected with various doses (one, two and three times) of solutions of UCNP NaYF<sub>4</sub> with a solution of bovine serum albumin (BSA) and folic acid (FA) (concentration 2 mg/ml).

The refractive index was measured on a multi-wavelength Abbe refractometer DR-M2/1550 (Atago, Japan) using 12 interference filters for the spectral region 480-1550 nm. To isolate wavelengths, narrow-band interference filters were used for 480, 486, 546, 589, 644, 656, 680, 800, 930, 1100, 1300, 1550 nm.

Data for refractive indices at a wavelength of 589 nm for tissues after the introduction of single, double and triple doses of NaYF<sub>4</sub>+BSA+FA nanoparticles are presented in Table 1.

**Table 1.** Refractive index at 589 nm for tissues after administration of various doses of UCNP

<b>Skin</b>	
Single dose	1.3557
Double dose	1.3723
Triple dose	1.3753
<b>Subcutaneous adipose tissue</b>	
Single dose	1.3797
Double dose	1.3946
Triple dose	1.3937
<b>Muscle tissue</b>	
Single dose	1.3449
Double dose	1.3598
Triple dose	1.3697
<b>Tumor tissue (model liver cancer)</b>	
Single dose	1.3459
Double dose	1.3623
Triple dose	1.4018

Figure 1 shows the dispersion dependences for various tissues taken in the area of tumor development after the introduction of NaYF<sub>4</sub> + BSA + FA UCNP in single, double and triple doses.

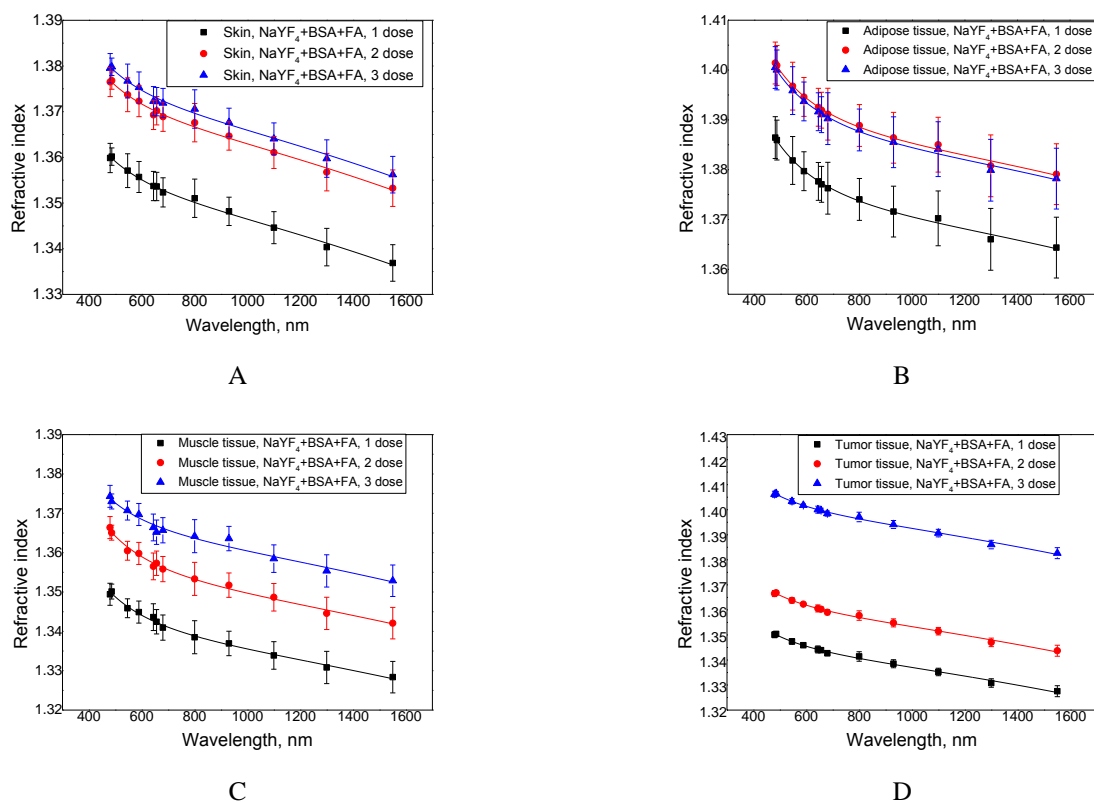


**Figure 1:** Dispersion dependence of altered biological tissues after the introduction of various doses of nanoparticles:  
 A - skin samples after administration of NaYF<sub>4</sub>+BSA+FA;  
 B - samples of subcutaneous adipose tissue after administration of NaYF<sub>4</sub>+BSA+FA;  
 C - muscle tissue samples after administration of NaYF<sub>4</sub>+BSA+FA;  
 D - samples of model liver cancer after administration of NaYF<sub>4</sub>+BSA+FA

According to the data obtained, for all tissues there is an increase in the refractive index with an increase in the administered dose of nanoparticles. The refractive index at a wavelength of 589 nm for tumor tissue was equal to 1.3459 for a single, 1.3623 for a double and 1.4018 for a triple dose of NaYF<sub>4</sub> + BSA + FA. An increased value of the refractive index may indicate the accumulation of nanoparticles in the tumor tissue and other tissues located in the area tumor development.

Thus, the injection of nanoparticles in different doses causes changes in the refractometric properties of tissues. Analysis of the refractive indices of various biological tissues after the introduction of various doses of nanoparticles of this type showed that tissues with a higher dose administered are characterized by a higher refractive index than tissue samples taken near the site of tumor development with the introduction of nanoparticles of lower doses. The result may be related to the accumulation of nanoparticles in tumor tissue and surrounding tissues and suggests that refractive index can be used to assess the accumulation of nanoparticles in tissues.

The study was supported by RSF grant no. 21-72-10057, <https://rscf.ru/project/21-72-10057/>.

## REFERENCES

- [1] M.H. Abdel-Kader, Photodynamic therapy. – Berlin: Springer-Verlag, p. 317. 2016.
- [2] E.V. Filonenko, Fluorescence diagnostics and photodynamic therapy - rationale for use and possibilities in oncology, Photodynamic therapy and photodiagnosics 1, 3-7, 2014.
- [3] P. Giannios, S. Koutsoumpas, K.G. Toutouzas, M. Matiatou, G.C. Zografos, and K. Moutzouris, Complex refractive index of normal and malignant human colorectal tissue in the visible and near-infrared, J. Biophotonics 10 (2), 303–310, 2017.
- [4] A.B. Bucharskaya, N.I. Dikht, G.A. Afanas'eva, G.S. Terentyuk, N.B. Zakharova, G.N. Maslyakova, B.N. Khlebtsov and N.G. Khlebtsov, Saratov. Nauch.-Med. Zh.. 11, 107, 2015
- [5] International Guiding Principles for Biomedical Research Involving Animals. CIOMS and ICLAS. 2012. <http://www.cioms.ch/index.php/12-newsflash/227-cioms-and-iclas-release-the-new-international-guiding-principles-for-biomedical-research-involving-animals>

## OPTICAL MULTIMODAL STUDY OF SKIN TUMORS

ELINA GENINA<sup>1,2</sup>, YURY SURKOV<sup>1,2</sup>, ISABELLA SEREBRYAKOVA<sup>1,2</sup>, EKATERINA LAZAREVA<sup>1,2</sup>, YANA KUZINOVA<sup>3</sup>, SERGEY ZAYTSEV<sup>1,4</sup>, OLGA KONOPATSKOVA<sup>3</sup>, DMITRY SAFRONOV<sup>3</sup>, SERGEY KAPRALOV<sup>3</sup>, AND VALERY TUCHIN<sup>1,2,5</sup>

<sup>1</sup>*Optics and Biophotonics Department, Saratov State University, Russia*

<sup>2</sup>*Laboratory of Laser Molecular Imaging and Machine Learning, National Research Tomsk State University, Russia*

<sup>3</sup>*Faculty Surgery and Oncology Department, Saratov State Medical University, Russia*

<sup>4</sup>*CNRS, CRAN, Université de Lorraine, France*

<sup>5</sup>*Institute of Precision Mechanics and Control, FRC "Saratov Scientific Centre of the Russian Academy of Sciences," Russia*

eagenina@yandex.ru

### ABSTRACT

Despite the development of medicine, cancer remains one of the leading causes of morbidity and mortality worldwide. Most often, if the tumor is diagnosed earlier and treated, the patient will have a better prognosis and much greater opportunities for complete recovery [1,2]. An effective solution to the problem is the use of modern optical technologies, such as light-induced autofluorescence spectroscopy (LIAFS), diffuse reflectance spectroscopy (DRS), Raman spectroscopy, optical coherence tomography (OCT), etc., which are non-invasive methods and provide obtaining diagnostic information in real time. In addition, they are portable and relatively low cost.

LIAFS and imaging relying on endogenous fluorophores represent non-invasive and fast approach for skin cancers diagnosis. However, due to high pigmentation of pigmentary skin nevi and early malignant melanomas of the skin, this method has a significant limitation because of low light penetration depth [3].

DRS is well suited for use in biomedical applications due to its low instrumentation cost, easy implementation. Optical fibers are coupled to a multichannel hyperspectral imaging system, which allows simultaneous acquisition of reflectance spectra from the sample [4].

Neoplastic cells are characterized by increased nuclear material, an increased nuclear-to-cytoplasmic ratio, increased mitotic activity, abnormal chromatin distribution, and decreased differentiation. There is a progressive loss of cell maturation, and proliferation of these undifferentiated cells results in increased metabolic activity. General features of neoplastic cells result in specific changes in nucleic acid, protein, lipid, and carbohydrate quantities and/or conformations. The original analyses for Raman signals are based on differences in intensity, shape, and location of the various Raman bands between normal and cancerous cells and tissues [5]. However, it should be taken into account that high sensitivity to small biochemical changes is accompanied by weak Raman signal often in the presence of high background. Overall, all skin lesions appear to share similar major Raman peaks and bands in fingerprint region. There are no distinctive Raman peaks or bands that can be uniquely assigned to, for example, basal cell carcinoma (BCC) by visual inspection alone. The development of the malignant skin disease increases the content of metabolic products in the pathological areas of the skin, changes the concentration of proteins and lipids [5].

OCT is used for preoperative determination of the peripheral boundaries of BCC in order to choose the optimal treatment method and minimize the invasiveness of surgical intervention. OCT is characterized by high efficiency for the *in vivo* diagnosis of malignant and benign skin tumors. It can be used for lifetime monitoring of structural changes of the skin during and after treatment of BCC in order to assess its effectiveness. However, due to the limited depth of probing, OCT cannot be used to determine the depth of invasion [6].

High resolution ultrasound (US) imaging systems, which use ultrasound frequencies above 15 MHz can differentiate structures of less than 100  $\mu\text{m}$  on the beam axis (axial resolution) and 200  $\mu\text{m}$  on the scan axis (resolution axis). The frequency ranges from 20 to 50 MHz, allowing visualization of the superficial layer of the skin (epidermis and dermis, and the upper part of hypodermis), where the majority of lesions and skin tumors are located. However, the sonographic appearance is often stereotyped: overall anechoic tumor, including large focally dense echoes [7].

In recent years there has been an increasing interest in the combined usage of these technologies that results in increased sensitivity and specificity [2]. Multimodal approaches can increase the effectiveness of early diagnosis and treatment procedures, as well as reduce cancer mortality.

Skin cancers are due to the development of abnormal cells that have the ability to invade or spread to other parts of the body. This is a heterogeneous group of cancers that includes malignant melanoma (MM) and non-melanoma skin cancer, the main ones being basal-cell carcinoma (BCC) and squamous-cell carcinoma (SCC) [8].

MM is the most aggressive form of skin cancer. It is the leading cause of death related to skin disease [1]. The overall mortality rate increases up to 50% in the case of lesions thicker than 4 mm. However, the overall survival of thin lesions (less than 0.5 mm thick) is excellent [2].

BCC is the most common epithelial neoplasm of the skin. It consists of cells similar to the cells of the basal layer of the epidermis and differs from other skin cancers by extremely rare metastasis, but it is capable of extensive local growth, which leads to significant cosmetic and functional disorders [8].

BCC can broadly be divided into three groups, based on the growth patterns. Nodular basal-cell carcinoma includes most of the remaining categories of basal-cell cancer. Nodular BCC (also known as "classic BCC") accounts for 50% of all BCC. It most commonly occurs on the sun-exposed areas of the head and neck. Histopathology shows aggregates of basaloid cells with well-defined borders, showing a peripheral palisading of cells and one or more typical clefts. Central necrosis with eosinophilic, granular features may be also present. The heavy aggregates of mucin determine a cystic structure.<sup>5</sup> Superficial BCC is characterized by a superficial proliferation of neoplastic basal-cells. Infiltrative BCC, which also encompasses morpheaform and micronodular BCC, is more difficult to treat with conservative methods, given its tendency to penetrate into deeper layers of the skin. Besides, pigmented BCC exhibits increased melanization [2, 8].

BCC is difficult to distinguish from benign formations by external signs. They can often come in association with other lesions of the skin, such as actinic keratosis, seborrheic keratosis, SCC. Often, patients do not perceive such wounds as skin cancer, but consider them accidental, frivolous "sores" or acne. However, it is prone to extensive local growth, which can lead to its germination deep into the skin and destruction of the surrounding tissue [9, 10].

Thus, multimodal approach in combined with optical clearing increases the effectiveness of methods of optical diagnostics of cancer.

In this study, the development of technologies for biomedical imaging of skin cancer is presented. A combination of high-resolution ultrasound examination and optical methods as Raman spectroscopy, OCT, and DRS were used for differentiation of different BCC subtypes. DRS measurements were combined with the use of biocompatible optical clearing agents to increase the efficacy of MM diagnostics.

#### Experimental design for basal-cell carcinoma study.

The study involved 40 light-skinned volunteers with BCC and benign neoplasms (BN). Informed consents were acquired from all patients prior to the study. Enrolled patients' age ranged from 40 to 84 years. Among the neoplasms studied were 5 of BN and 26 of BCC, which were divided into the following subtypes: infiltrative-ulcerative (3), pigmented (2), superficial (15), morpheaform (3) and nodular BCC (3). The group of BN included nevi, fibromas and dermatofibromas. At the beginning of the study, a visual examination of the volunteer was carried out by an oncologist. The final diagnosis was made by a specialist based on the results of cytological and/or histopathological studies at the Regional Oncological Clinics No. 2 of Saratov.

The neoplasms were photographed before the study using commercially evaluated Digital Video Dermatoscope DE300 Firefly (tpm taberna pro medicum GmbH, Germany) with 10× zoom and 1920×1080 resolution.

For ultrasonography we used the DUB SkinScanner (tpm taberna pro medicum GmbH, Germany) in B-scan mode with US probes with frequencies of 33 and 75 MHz, scanning depths of 6 and 3.2 mm and longitudinal resolution of 48 and 21 μm, respectively. The width of the ultrasound scanning window was 13 mm.

To analyze the US data for each neoplasm, 5 US images were selected without artifacts and having the most contrasting borders of the neoplasm with healthy skin. For each ultrasound image, a region of interest (ROI) was marked by the operator, and 12 parameters were calculated depending on the shape and size of the neoplasm: area, perimeter, roundness, eccentricity of the ellipse describing ROI, equivalent diameter of a circle area of a rectangle describing ROI, length of the major axis of the ellipse describing ROI, length of the minor major axis of the ellipse describing ROI, modulus the angle between the major axis of the ellipse describing the ROI and the horizontal axis of the image, the ratio of the area of the ROI to the area of the rectangle describing the ROI, the angle between the maximum diameter of the rectangle describing the ROI and the horizontal axis of the image, the ratio of the perimeter to the area.

Diffuse reflectance was recorded using multichannel reflectance spectrometer USB4000-UV-VIS with a fiber-optic probe QR400-7-VIS-NIR (Ocean Optics, USA) and a spectral range of 450-950 nm. For each neoplasm, at least 5 diffuse reflectance spectra were recorded. To take into account the individual spectral features of the volunteer's skin, for each neoplasm, healthy skin areas nearby or symmetrically located to the lesions were measured.

From the data of the reflectance spectra, the several characteristic coefficients were calculated. The melanin pigmentation index ( $M$ ) of human skin was determined by the following formula:

$$M = 100 \times (OD_{620} - OD_{700}), \quad (1)$$

where  $OD_{\lambda} = -\lg R_{\lambda}$  is the effective optical density at the wavelength  $\lambda$ .

The erythema index ( $E$ ) was calculated using the following formula:

$$E = 100[OD_{560} + 1.5(OD_{545} + OD_{575}) - 2(OD_{510} + OD_{610})]. \quad (2)$$

The following expression was used to estimate the index of hemoglobin content ( $H$ ):

$$H = \frac{OD_{545} - OD_{529}}{16} - \frac{OD_{570} - OD_{545}}{25}. \quad (3)$$

The slope coefficient of the diffuse reflectance spectrum ( $K$ ) in the wavelength range of 650-800 nm and the coefficient reflecting the deviation of the reflectance spectrum from the linear approximation ( $N$ ) in the wavelength range of 650-800 nm were also calculated.

The coefficient  $R_t$  was used to differentiate between malignant melanoma and dysplastic nevi and calculated by the formula:

$$R_t = \frac{R_{\text{healthy}500} R_{\text{neoplasm}700}}{R_{\text{healthy}700} R_{\text{neoplasm}500}}, \quad (4)$$

where  $R_{\text{healthy}500}$ ,  $R_{\text{neoplasm}500}$ ,  $R_{\text{healthy}700}$ , and  $R_{\text{neoplasm}700}$  are the diffuse reflectance of healthy skin and neoplasms at wavelengths of 500 and 700 nm, respectively.

OCT images were recorded using a GAN930V2-BU (Thorlabs, USA) spectral OCT operating at a central wavelength of 930 nm with an axial resolution of 5.34  $\mu\text{m}$  and a scanning depth of 2 mm. At least 15 scans were obtained from different areas of the neoplasm.

For texture analysis 180 OCT images without artifacts were selected. Texture analysis is the analysis of changes in the brightness of pixels within a ROI. This includes the first-order statistical (FOS) methods: mean, standard deviation, skewness, and kurtosis, which are related to the distribution of grayscale pixel intensity and do not depend on interpixel correlation. Second-order statistics (SOS) or gray level coincidence matrices (GLCM), on the contrary, depends on the spatial arrangement of the intensity of the pixels in the ROI. The SOS (or Haralick) parameters include energy, homogeneity, contrast, correlation and entropy.

For each OCT B-scan, ROI containing an image of the internal structure of the neoplasm was chosen. The size of the ROI was not less than 534  $\mu\text{m}$  in depth and not less than 400  $\mu\text{m}$  in width.

In order to reduce the effect of noise outside the structural image of the biological tissue, a threshold filter was used. The intensity of each pixel was compared with the threshold value, if the intensity was less than or equal to the threshold value, the intensity of this pixel was taken equal to 0. To determine the threshold value on each OCT scan, a rectangular area approximately 500 by 2000  $\mu\text{m}$  in size below the biological tissue image was selected, according to which the average and standard deviation of the pixel intensity were calculated. The threshold value was the sum of the mean and standard deviation. To reduce the effect of speckle noise on B-scans, we successively used an erosion filter with a window width of 3 pixels and a 2D smoothing filter with a Gaussian kernel with a standard deviation of 1.5.

To calculate the Haralick parameters, GLCM were calculated for four orientations: horizontal, vertical and two diagonals (directions defined by four angles: 0°, 45°, 90° and 135°). From each GLCM, 5 Haralick characteristics were extracted - energy, homogeneity, contrast, correlation and entropy. Five FOS parameters were calculated from the gray level distribution histogram. In total, 65 characteristic parameters were obtained for each ROI. Pixels with intensity equal to zero, associated with the background, were not taken into account when estimating the FOS and Haralick parameters.

Thus, five observations were obtained for each neoplasm; each observation consisted of 6 DRS parameters, 65 OCT parameters, 12 US parameters. All calculated parameters were compared with the oncologist's diagnosis and combined into a single table, where the columns corresponded to the parameter, the rows to measurements (observations).

To classify the diagnosis and subtype of BCC according to the data of the formed observations, a classifier was built based on the method of k-weighted nearest neighbors. The set number of required nearest neighbors was 10. The Euclidean function was used as the distance metric. To train and evaluate the quality of the model, a cross-validation method was used with data splitting into 5 sections; the number of training iterations was 10. Before the analysis, all parameters were normalized to the maximum value of the parameter among all observations.

Raman spectra were measured with spectrometer QE65000 (Ocean Optics, USA) equipped with 785-nm diode laser and probe ( $f = 7.5 \text{ mm}$ ).

#### **Experimental design for melanoma study.**

The objects of the study were 9 outbred mice. Transplantation of model skin melanoma was carried out by subcutaneous injection of a suspension of B16F10 melanoma tumor cells into the region of the outer side of the thigh from both sides. The experimental protocol consisted of two stages. The first stage was carried out on day 7 after subcutaneous injection of tumor cell suspension and was performed *in vivo*. The second stage was carried out *ex vivo* on day 14.

DRS was used in combination with optical immersion technique using polyethylene glycol-400 (PEG) and aqueous solutions of glucose and sucrose as optical clearing agents (OCA). As enhancers, propylene glycol (PG), oleic acid (OA), and dimethyl sulfoxide (DMSO) were used.

The spectral probe was placed in contact with the central part of the skin areas with subcutaneous melanoma, and the DR spectra of intact skin were registered. Similar DR spectra were also measured near the area of melanoma localization on healthy skin areas. After that, the examined healthy and affected areas of the skin were subjected to dermabrasion for 1 minute using cosmetic device MD3A 933 (Gezatone, France). Further, two areas of mouse skin affected by melanoma, as well as adjacent areas of healthy skin, were treated with therapeutic US for 5 minutes using Dinatron 125 (Dinatronics, USA) in the following mode: CW, 1 MHz, 1Wt/cm<sup>2</sup>. During treatment, 200  $\mu\text{l}$  of the OCA + enhancer mixture was applied to the skin under an ultrasound probe. After ultrasonic clarification, the final DR spectra were registered from each area of the skin.

Changes in the slope of the DR spectra in the ranges of 470–520 nm and 650–800 nm after optical clearing were analyzed. Differences in the DR signal in the area of three blood absorption peaks (420 nm, 545 nm and 575 nm) between skin areas with melanoma and healthy skin were estimated using the ratio  $R_{benign}/R_{melanoma}$ .

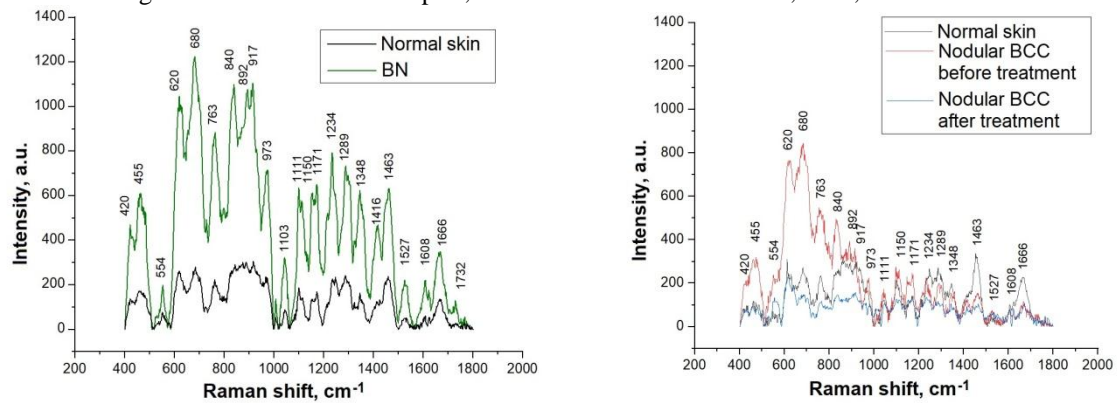
**Results of Multimodal diagnostics of basal-cell carcinoma.**

Figure 1 shows the results of evaluations of classification models, a Compatibility Matrix (Validation) based on the nearest neighbor method. Diagonal cells show where observations from the true group were assigned to their corresponding groups. It is clearly seen that the combination of DRS, OCT and US leads to an increase in true positive rates (TPR). TPR has maximal values for surface BCC (100%) and minimal for pigmented BCC (60%).

Method	Number of observations	Predicted class	TPR/FNR																																																																																																																													
DRS	<table border="1"> <thead> <tr> <th rowspan="2">True class</th> <th colspan="6">Predicted class</th> </tr> <tr> <th>BN</th> <th>Infiltrative-ulcerative BCC</th> <th>Pigmented BCC</th> <th>Surface BCC</th> <th>Morpheaform BCC</th> <th>Nodular BCC</th> </tr> </thead> <tbody> <tr> <th>BN</th> <td>37</td> <td></td> <td>1</td> <td>9</td> <td>3</td> <td></td> </tr> <tr> <th>Infiltrative-ulcerative BCC</th> <td>3</td> <td>5</td> <td>1</td> <td>6</td> <td></td> <td></td> </tr> <tr> <th>Pigmented BCC</th> <td>2</td> <td>1</td> <td>4</td> <td>3</td> <td></td> <td></td> </tr> <tr> <th>Surface BCC</th> <td></td> <td></td> <td></td> <td>74</td> <td></td> <td>1</td> </tr> <tr> <th>Morpheaform BCC</th> <td>1</td> <td></td> <td></td> <td>3</td> <td>11</td> <td></td> </tr> <tr> <th>Nodular BCC</th> <td></td> <td></td> <td></td> <td>4</td> <td></td> <td>13</td> </tr> </tbody> </table>	True class	Predicted class						BN	Infiltrative-ulcerative BCC	Pigmented BCC	Surface BCC	Morpheaform BCC	Nodular BCC	BN	37		1	9	3		Infiltrative-ulcerative BCC	3	5	1	6			Pigmented BCC	2	1	4	3			Surface BCC				74		1	Morpheaform BCC	1			3	11		Nodular BCC				4		13	<table border="1"> <thead> <tr> <th rowspan="2">True class</th> <th colspan="6">Predicted class</th> <th colspan="2">TPR/FNR</th> </tr> <tr> <th>BN</th> <th>Infiltrative-ulcerative BCC</th> <th>Pigmented BCC</th> <th>Surface BCC</th> <th>Morpheaform BCC</th> <th>Nodular BCC</th> <th>TPR</th> <th>FNR</th> </tr> </thead> <tbody> <tr> <th>BN</th> <td>74,0%</td> <td></td> <td>2,0%</td> <td>18,0%</td> <td>6,0%</td> <td></td> <td>74,0%</td> <td>26,0%</td> </tr> <tr> <th>Infiltrative-ulcerative BCC</th> <td>20,0%</td> <td>33,3%</td> <td>6,7%</td> <td>40,0%</td> <td></td> <td></td> <td>33,3%</td> <td>66,7%</td> </tr> <tr> <th>Pigmented BCC</th> <td>20,0%</td> <td>10,0%</td> <td>40,0%</td> <td>30,0%</td> <td></td> <td></td> <td>40,0%</td> <td>60,0%</td> </tr> <tr> <th>Surface BCC</th> <td></td> <td></td> <td></td> <td>98,7%</td> <td></td> <td>1,3%</td> <td>98,7%</td> <td>1,3%</td> </tr> <tr> <th>Morpheaform BCC</th> <td>6,7%</td> <td></td> <td></td> <td>20,0%</td> <td>73,3%</td> <td></td> <td>73,3%</td> <td>26,7%</td> </tr> <tr> <th>Nodular BCC</th> <td></td> <td></td> <td></td> <td>26,7%</td> <td></td> <td>73,3%</td> <td>73,3%</td> <td>26,7%</td> </tr> </tbody> </table>	True class	Predicted class						TPR/FNR		BN	Infiltrative-ulcerative BCC	Pigmented BCC	Surface BCC	Morpheaform BCC	Nodular BCC	TPR	FNR	BN	74,0%		2,0%	18,0%	6,0%		74,0%	26,0%	Infiltrative-ulcerative BCC	20,0%	33,3%	6,7%	40,0%			33,3%	66,7%	Pigmented BCC	20,0%	10,0%	40,0%	30,0%			40,0%	60,0%	Surface BCC				98,7%		1,3%	98,7%	1,3%	Morpheaform BCC	6,7%			20,0%	73,3%		73,3%	26,7%	Nodular BCC				26,7%		73,3%	73,3%	26,7%
	True class		Predicted class																																																																																																																													
BN		Infiltrative-ulcerative BCC	Pigmented BCC	Surface BCC	Morpheaform BCC	Nodular BCC																																																																																																																										
BN	37		1	9	3																																																																																																																											
Infiltrative-ulcerative BCC	3	5	1	6																																																																																																																												
Pigmented BCC	2	1	4	3																																																																																																																												
Surface BCC				74		1																																																																																																																										
Morpheaform BCC	1			3	11																																																																																																																											
Nodular BCC				4		13																																																																																																																										
True class	Predicted class						TPR/FNR																																																																																																																									
	BN	Infiltrative-ulcerative BCC	Pigmented BCC	Surface BCC	Morpheaform BCC	Nodular BCC	TPR	FNR																																																																																																																								
BN	74,0%		2,0%	18,0%	6,0%		74,0%	26,0%																																																																																																																								
Infiltrative-ulcerative BCC	20,0%	33,3%	6,7%	40,0%			33,3%	66,7%																																																																																																																								
Pigmented BCC	20,0%	10,0%	40,0%	30,0%			40,0%	60,0%																																																																																																																								
Surface BCC				98,7%		1,3%	98,7%	1,3%																																																																																																																								
Morpheaform BCC	6,7%			20,0%	73,3%		73,3%	26,7%																																																																																																																								
Nodular BCC				26,7%		73,3%	73,3%	26,7%																																																																																																																								
OCT	<table border="1"> <thead> <tr> <th rowspan="2">True class</th> <th colspan="6">Predicted class</th> </tr> <tr> <th>BN</th> <th>Infiltrative-ulcerative BCC</th> <th>Pigmented BCC</th> <th>Surface BCC</th> <th>Morpheaform BCC</th> <th>Nodular BCC</th> </tr> </thead> <tbody> <tr> <th>BN</th> <td>42</td> <td></td> <td>1</td> <td>4</td> <td>1</td> <td>2</td> </tr> <tr> <th>Infiltrative-ulcerative BCC</th> <td></td> <td>11</td> <td></td> <td>4</td> <td></td> <td></td> </tr> <tr> <th>Pigmented BCC</th> <td>3</td> <td>1</td> <td>3</td> <td>2</td> <td>1</td> <td></td> </tr> <tr> <th>Surface BCC</th> <td>4</td> <td>2</td> <td></td> <td>66</td> <td></td> <td>3</td> </tr> <tr> <th>Morpheaform BCC</th> <td>2</td> <td>1</td> <td></td> <td>4</td> <td>8</td> <td></td> </tr> <tr> <th>Nodular BCC</th> <td>1</td> <td></td> <td></td> <td>8</td> <td>1</td> <td>5</td> </tr> </tbody> </table>	True class	Predicted class						BN	Infiltrative-ulcerative BCC	Pigmented BCC	Surface BCC	Morpheaform BCC	Nodular BCC	BN	42		1	4	1	2	Infiltrative-ulcerative BCC		11		4			Pigmented BCC	3	1	3	2	1		Surface BCC	4	2		66		3	Morpheaform BCC	2	1		4	8		Nodular BCC	1			8	1	5	<table border="1"> <thead> <tr> <th rowspan="2">True class</th> <th colspan="6">Predicted class</th> <th colspan="2">TPR/FNR</th> </tr> <tr> <th>BN</th> <th>Infiltrative-ulcerative BCC</th> <th>Pigmented BCC</th> <th>Surface BCC</th> <th>Morpheaform BCC</th> <th>Nodular BCC</th> <th>TPR</th> <th>FNR</th> </tr> </thead> <tbody> <tr> <th>BN</th> <td>84,0%</td> <td></td> <td>2,0%</td> <td>8,0%</td> <td>2,0%</td> <td>4,0%</td> <td>84,0%</td> <td>16,0%</td> </tr> <tr> <th>Infiltrative-ulcerative BCC</th> <td></td> <td>73,3%</td> <td></td> <td>26,7%</td> <td></td> <td></td> <td>73,3%</td> <td>26,7%</td> </tr> <tr> <th>Pigmented BCC</th> <td>30,0%</td> <td>10,0%</td> <td>30,0%</td> <td>20,0%</td> <td>10,0%</td> <td></td> <td>30,0%</td> <td>70,0%</td> </tr> <tr> <th>Surface BCC</th> <td>5,3%</td> <td>2,7%</td> <td></td> <td>88,0%</td> <td></td> <td>4,0%</td> <td>88,0%</td> <td>12,0%</td> </tr> <tr> <th>Morpheaform BCC</th> <td>13,3%</td> <td>6,7%</td> <td></td> <td>26,7%</td> <td>53,3%</td> <td></td> <td>53,3%</td> <td>46,7%</td> </tr> <tr> <th>Nodular BCC</th> <td>6,7%</td> <td></td> <td></td> <td>53,3%</td> <td>6,7%</td> <td>33,3%</td> <td>33,3%</td> <td>66,7%</td> </tr> </tbody> </table>	True class	Predicted class						TPR/FNR		BN	Infiltrative-ulcerative BCC	Pigmented BCC	Surface BCC	Morpheaform BCC	Nodular BCC	TPR	FNR	BN	84,0%		2,0%	8,0%	2,0%	4,0%	84,0%	16,0%	Infiltrative-ulcerative BCC		73,3%		26,7%			73,3%	26,7%	Pigmented BCC	30,0%	10,0%	30,0%	20,0%	10,0%		30,0%	70,0%	Surface BCC	5,3%	2,7%		88,0%		4,0%	88,0%	12,0%	Morpheaform BCC	13,3%	6,7%		26,7%	53,3%		53,3%	46,7%	Nodular BCC	6,7%			53,3%	6,7%	33,3%	33,3%	66,7%
	True class		Predicted class																																																																																																																													
BN		Infiltrative-ulcerative BCC	Pigmented BCC	Surface BCC	Morpheaform BCC	Nodular BCC																																																																																																																										
BN	42		1	4	1	2																																																																																																																										
Infiltrative-ulcerative BCC		11		4																																																																																																																												
Pigmented BCC	3	1	3	2	1																																																																																																																											
Surface BCC	4	2		66		3																																																																																																																										
Morpheaform BCC	2	1		4	8																																																																																																																											
Nodular BCC	1			8	1	5																																																																																																																										
True class	Predicted class						TPR/FNR																																																																																																																									
	BN	Infiltrative-ulcerative BCC	Pigmented BCC	Surface BCC	Morpheaform BCC	Nodular BCC	TPR	FNR																																																																																																																								
BN	84,0%		2,0%	8,0%	2,0%	4,0%	84,0%	16,0%																																																																																																																								
Infiltrative-ulcerative BCC		73,3%		26,7%			73,3%	26,7%																																																																																																																								
Pigmented BCC	30,0%	10,0%	30,0%	20,0%	10,0%		30,0%	70,0%																																																																																																																								
Surface BCC	5,3%	2,7%		88,0%		4,0%	88,0%	12,0%																																																																																																																								
Morpheaform BCC	13,3%	6,7%		26,7%	53,3%		53,3%	46,7%																																																																																																																								
Nodular BCC	6,7%			53,3%	6,7%	33,3%	33,3%	66,7%																																																																																																																								
US	<table border="1"> <thead> <tr> <th rowspan="2">True class</th> <th colspan="6">Predicted class</th> </tr> <tr> <th>BN</th> <th>Infiltrative-ulcerative BCC</th> <th>Pigmented BCC</th> <th>Surface BCC</th> <th>Morpheaform BCC</th> <th>Nodular BCC</th> </tr> </thead> <tbody> <tr> <th>BN</th> <td>45</td> <td></td> <td></td> <td>3</td> <td>1</td> <td>1</td> </tr> <tr> <th>Infiltrative-ulcerative BCC</th> <td></td> <td>11</td> <td></td> <td>2</td> <td></td> <td>2</td> </tr> <tr> <th>Pigmented BCC</th> <td>2</td> <td></td> <td></td> <td>8</td> <td></td> <td></td> </tr> <tr> <th>Surface BCC</th> <td></td> <td>2</td> <td></td> <td>73</td> <td></td> <td></td> </tr> <tr> <th>Morpheaform BCC</th> <td></td> <td>3</td> <td></td> <td>9</td> <td>2</td> <td>1</td> </tr> <tr> <th>Nodular BCC</th> <td>4</td> <td>5</td> <td></td> <td>2</td> <td></td> <td>4</td> </tr> </tbody> </table>	True class	Predicted class						BN	Infiltrative-ulcerative BCC	Pigmented BCC	Surface BCC	Morpheaform BCC	Nodular BCC	BN	45			3	1	1	Infiltrative-ulcerative BCC		11		2		2	Pigmented BCC	2			8			Surface BCC		2		73			Morpheaform BCC		3		9	2	1	Nodular BCC	4	5		2		4	<table border="1"> <thead> <tr> <th rowspan="2">True class</th> <th colspan="6">Predicted class</th> <th colspan="2">TPR/FNR</th> </tr> <tr> <th>BN</th> <th>Infiltrative-ulcerative BCC</th> <th>Pigmented BCC</th> <th>Surface BCC</th> <th>Morpheaform BCC</th> <th>Nodular BCC</th> <th>TPR</th> <th>FNR</th> </tr> </thead> <tbody> <tr> <th>BN</th> <td>90,0%</td> <td></td> <td></td> <td>6,0%</td> <td>2,0%</td> <td>2,0%</td> <td>90,0%</td> <td>10,0%</td> </tr> <tr> <th>Infiltrative-ulcerative BCC</th> <td></td> <td>73,3%</td> <td></td> <td>13,3%</td> <td></td> <td>13,3%</td> <td>73,3%</td> <td>26,7%</td> </tr> <tr> <th>Pigmented BCC</th> <td>20,0%</td> <td></td> <td></td> <td>80,0%</td> <td></td> <td></td> <td>0,0%</td> <td>100,0%</td> </tr> <tr> <th>Surface BCC</th> <td></td> <td>2,7%</td> <td></td> <td>97,3%</td> <td></td> <td></td> <td>97,3%</td> <td>2,7%</td> </tr> <tr> <th>Morpheaform BCC</th> <td></td> <td>20,0%</td> <td></td> <td>60,0%</td> <td>13,3%</td> <td>6,7%</td> <td>13,3%</td> <td>86,7%</td> </tr> <tr> <th>Nodular BCC</th> <td>26,7%</td> <td>33,3%</td> <td></td> <td>13,3%</td> <td></td> <td>26,7%</td> <td>26,7%</td> <td>73,3%</td> </tr> </tbody> </table>	True class	Predicted class						TPR/FNR		BN	Infiltrative-ulcerative BCC	Pigmented BCC	Surface BCC	Morpheaform BCC	Nodular BCC	TPR	FNR	BN	90,0%			6,0%	2,0%	2,0%	90,0%	10,0%	Infiltrative-ulcerative BCC		73,3%		13,3%		13,3%	73,3%	26,7%	Pigmented BCC	20,0%			80,0%			0,0%	100,0%	Surface BCC		2,7%		97,3%			97,3%	2,7%	Morpheaform BCC		20,0%		60,0%	13,3%	6,7%	13,3%	86,7%	Nodular BCC	26,7%	33,3%		13,3%		26,7%	26,7%	73,3%
	True class		Predicted class																																																																																																																													
BN		Infiltrative-ulcerative BCC	Pigmented BCC	Surface BCC	Morpheaform BCC	Nodular BCC																																																																																																																										
BN	45			3	1	1																																																																																																																										
Infiltrative-ulcerative BCC		11		2		2																																																																																																																										
Pigmented BCC	2			8																																																																																																																												
Surface BCC		2		73																																																																																																																												
Morpheaform BCC		3		9	2	1																																																																																																																										
Nodular BCC	4	5		2		4																																																																																																																										
True class	Predicted class						TPR/FNR																																																																																																																									
	BN	Infiltrative-ulcerative BCC	Pigmented BCC	Surface BCC	Morpheaform BCC	Nodular BCC	TPR	FNR																																																																																																																								
BN	90,0%			6,0%	2,0%	2,0%	90,0%	10,0%																																																																																																																								
Infiltrative-ulcerative BCC		73,3%		13,3%		13,3%	73,3%	26,7%																																																																																																																								
Pigmented BCC	20,0%			80,0%			0,0%	100,0%																																																																																																																								
Surface BCC		2,7%		97,3%			97,3%	2,7%																																																																																																																								
Morpheaform BCC		20,0%		60,0%	13,3%	6,7%	13,3%	86,7%																																																																																																																								
Nodular BCC	26,7%	33,3%		13,3%		26,7%	26,7%	73,3%																																																																																																																								
DRS&OCT&US	<table border="1"> <thead> <tr> <th rowspan="2">True class</th> <th colspan="6">Predicted class</th> </tr> <tr> <th>BN</th> <th>Infiltrative-ulcerative BCC</th> <th>Pigmented BCC</th> <th>Surface BCC</th> <th>Morpheaform BCC</th> <th>Nodular BCC</th> </tr> </thead> <tbody> <tr> <th>BN</th> <td>49</td> <td>1</td> <td></td> <td></td> <td></td> <td></td> </tr> <tr> <th>Infiltrative-ulcerative BCC</th> <td></td> <td>12</td> <td></td> <td>3</td> <td></td> <td></td> </tr> <tr> <th>Pigmented BCC</th> <td>1</td> <td></td> <td>6</td> <td>3</td> <td></td> <td></td> </tr> <tr> <th>Surface BCC</th> <td></td> <td></td> <td></td> <td>75</td> <td></td> <td></td> </tr> <tr> <th>Morpheaform BCC</th> <td></td> <td>1</td> <td></td> <td></td> <td>12</td> <td>2</td> </tr> <tr> <th>Nodular BCC</th> <td></td> <td></td> <td></td> <td>2</td> <td></td> <td>13</td> </tr> </tbody> </table>	True class	Predicted class						BN	Infiltrative-ulcerative BCC	Pigmented BCC	Surface BCC	Morpheaform BCC	Nodular BCC	BN	49	1					Infiltrative-ulcerative BCC		12		3			Pigmented BCC	1		6	3			Surface BCC				75			Morpheaform BCC		1			12	2	Nodular BCC				2		13	<table border="1"> <thead> <tr> <th rowspan="2">True class</th> <th colspan="6">Predicted class</th> <th colspan="2">TPR/FNR</th> </tr> <tr> <th>BN</th> <th>Infiltrative-ulcerative BCC</th> <th>Pigmented BCC</th> <th>Surface BCC</th> <th>Morpheaform BCC</th> <th>Nodular BCC</th> <th>TPR</th> <th>FNR</th> </tr> </thead> <tbody> <tr> <th>BN</th> <td>98,0%</td> <td>2,0%</td> <td></td> <td></td> <td></td> <td></td> <td>98,0%</td> <td>2,0%</td> </tr> <tr> <th>Infiltrative-ulcerative BCC</th> <td></td> <td>80,0%</td> <td></td> <td>20,0%</td> <td></td> <td></td> <td>80,0%</td> <td>20,0%</td> </tr> <tr> <th>Pigmented BCC</th> <td>10,0%</td> <td></td> <td>60,0%</td> <td>30,0%</td> <td></td> <td></td> <td>60,0%</td> <td>40,0%</td> </tr> <tr> <th>Surface BCC</th> <td></td> <td></td> <td></td> <td>100,0%</td> <td></td> <td></td> <td>100,0%</td> <td>0,0%</td> </tr> <tr> <th>Morpheaform BCC</th> <td></td> <td>6,7%</td> <td></td> <td></td> <td>80,0%</td> <td>13,3%</td> <td>80,0%</td> <td>20,0%</td> </tr> <tr> <th>Nodular BCC</th> <td></td> <td></td> <td></td> <td>13,3%</td> <td></td> <td>86,7%</td> <td>86,7%</td> <td>13,3%</td> </tr> </tbody> </table>	True class	Predicted class						TPR/FNR		BN	Infiltrative-ulcerative BCC	Pigmented BCC	Surface BCC	Morpheaform BCC	Nodular BCC	TPR	FNR	BN	98,0%	2,0%					98,0%	2,0%	Infiltrative-ulcerative BCC		80,0%		20,0%			80,0%	20,0%	Pigmented BCC	10,0%		60,0%	30,0%			60,0%	40,0%	Surface BCC				100,0%			100,0%	0,0%	Morpheaform BCC		6,7%			80,0%	13,3%	80,0%	20,0%	Nodular BCC				13,3%		86,7%	86,7%	13,3%
	True class		Predicted class																																																																																																																													
BN		Infiltrative-ulcerative BCC	Pigmented BCC	Surface BCC	Morpheaform BCC	Nodular BCC																																																																																																																										
BN	49	1																																																																																																																														
Infiltrative-ulcerative BCC		12		3																																																																																																																												
Pigmented BCC	1		6	3																																																																																																																												
Surface BCC				75																																																																																																																												
Morpheaform BCC		1			12	2																																																																																																																										
Nodular BCC				2		13																																																																																																																										
True class	Predicted class						TPR/FNR																																																																																																																									
	BN	Infiltrative-ulcerative BCC	Pigmented BCC	Surface BCC	Morpheaform BCC	Nodular BCC	TPR	FNR																																																																																																																								
BN	98,0%	2,0%					98,0%	2,0%																																																																																																																								
Infiltrative-ulcerative BCC		80,0%		20,0%			80,0%	20,0%																																																																																																																								
Pigmented BCC	10,0%		60,0%	30,0%			60,0%	40,0%																																																																																																																								
Surface BCC				100,0%			100,0%	0,0%																																																																																																																								
Morpheaform BCC		6,7%			80,0%	13,3%	80,0%	20,0%																																																																																																																								
Nodular BCC				13,3%		86,7%	86,7%	13,3%																																																																																																																								

**Figure 1:** The indicators of validation of the classification of neoplasms, true positive rates (TPR) are marked in blue, false negative rates (FNR) are marked in orange. Rows show the true class, columns show the predicted class. The values in the empty cells correspond to 0.

Raman spectra for normal skin tissue and of nodular BCC before and after treatment are depicted in Figure 2. Proteins predominantly contribute to the appearance of bands in the spectral range 1240–1270, 1340, 1440–1460, and 1665  $\text{cm}^{-1}$ , the spectral features arising from the contribution of lipids, are observed in the 1271–1301, 1440, 1650–1660  $\text{cm}^{-1}$  bands.



**Figure 2:** Raman spectra of normal skin tissue, BN, and nodular BCC before and after treatment

One of the significant differences between malignant and benign formations is the process of metabolism and destruction of collagen. Cells of malignant tumors form fast-growing, low-differentiated structures, and the development of such structures is accompanied by the increased activity of collagenase. Collagenase destroys the molecular bonds of collagen fibers, and changes in Raman spectra of skin tissue can be observed in 1248, 1454, and 1665  $\text{cm}^{-1}$  bands associated with peaks of collagen [5]. In the BCC, there is an increased content of proteins (430, 475  $\text{cm}^{-1}$ ) and nucleic acids (622, 685  $\text{cm}^{-1}$ ), a decreased content of lipids (1287, 1419  $\text{cm}^{-1}$ ) and keratin (1463, 1670  $\text{cm}^{-1}$ ). Increased peaks associated with DNA (755  $\text{cm}^{-1}$ ) and cell nuclei (831  $\text{cm}^{-1}$ ).

**Results of Multimodal diagnostics of melanoma.** All mixtures of OCA to varying degrees after enlightenment showed an increase in differences in the DR signal from the three peaks of blood absorption between the skin areas with melanoma and healthy skin. The greatest differences after skin optical clearing *in vivo* were demonstrated by a mixture of PEG/OA/PG (an increase of ~2 times after the clearing relative to intact skin at the wavelength 420 nm (Soret absorption band).

The reduction in skin scattering, and, as a result, the best effect of optical clearing, based on the analysis of relative changes in the  $R_{benign}/R_{melanoma}$  ratio, was achieved at the *ex vivo* stage of the experiment with a mixture of Glucose/OA/PG. At the wavelengths 420 nm, 545 nm, and 575 nm, the relative changes in the  $R_{benign}/R_{melanoma}$  ratio after clearing were 314%, 205%, and 204%, respectively.

Thus, the sizes of neoplasms were evaluated using ultrasound examination, and their internal structure was visualized using OCT in combination with OC. Diffuse reflectance can extract physiological parameters such as hemoglobin content, oxygen saturation, and tissue microarchitecture. Raman spectroscopy is helpful for determining lipid, nuclear, and protein content.

Our results demonstrate the ability of these modalities to quantitatively assess tissue biochemical, structural, and physiological parameters that can be used to determine tissue pathology. Our future work will be extended on the use of all presented modalities, including skin optical clearing.

The study was funded by RFBR grant number 20-52-56005.

## REFERENCES

- [1] World Health Organization. Cancer. [https://www.who.int/health-topics/cancer#tab=tab\\_3](https://www.who.int/health-topics/cancer#tab=tab_3)
- [2] L. Lim, B. Nichols, M. R. Migden, N. Rajaram, J. S. Reichenberg, M. K. Markey, M. I. Ross, J.W. Tunnell, Clinical study of noninvasive *in vivo* melanoma and nonmelanoma skin cancers using multimodal spectral diagnosis, *J. Biomed. Opt.* 117003-117003, 2014.
- [3] E. Borisova, E. Carstea, L. Cristescu, E. Pavlova, N. Hadjiolov, P. Troyanova, L. Avramov, Light-induced fluorescence spectroscopy and optical coherence tomography of basal cell carcinoma, *J. Innovat. Opt. Health Sci.* 261-268, 2009.
- [4] E. Borisova, E. Nikolova, P. Troyanova, L. Avramov, Autofluorescence and diffuse reflectance spectroscopy of pigment disorders in human skin, *J. Optoelectron. Adv. Materials* 717–722, 2008.
- [5] Multimodal optical diagnostics of cancer, V. V. Tuchin, J. Popp, and V. Zakharov, (Eds.), Springer Nature, Cham, Switzerland p. 3-597, 2020.
- [6] W. Gao, V.P. Zakharov, O.O. Myakinin, I.A. Bratchenko, D.N. Artemyev, D.V. Kornilin, Medical images classification for skin cancer using quantitative image features with optical coherence tomography, *J. Innovat. Opt. Health Sci.* 1650003, 2016.
- [7] M. Laurent, M. Samimi, G. Georgesco, Y. Mourtada, M. Naouri, J.M. Grégoire, F. Ossant, F. Patat, L. Vaillant, High resolution ultrasound imaging of melanocytic and other pigmented lesions of the skin, Chapter 8, *Ultrasound imaging* (Ed. M. Tanabe), InTech, London, UK, p. 139-150, 2011.
- [8] G. Paolino, M. Donati, D. Didona, S. R. Mercuri, C. Cantisani, Histology of non-melanoma skin cancers: an update, *Biomedicine*, 71, 2017.
- [9] N. Fusco, G. Lopez, U. Gianelli, Basal-cell carcinoma and seborrheic keratosis: When opposites attract, *Int. J. Surg. Pathol.* 464, 2015.
- [10] W. James, D.M. Elston, J.R. Treat, M.A. Rosenbach, I.M. Neuhaus, Andrews' diseases of the skin: Clinical dermatology, 13th Edition, Elsevier, North York, Canada, p. 1008, 2020.

## MODELING OF COVID-19 SPREAD: FROM CITY SCALE TO COUNTRY SCALE

MIKHAIL KIRILLIN<sup>1</sup>, ALEKSANDR KHILOV<sup>1</sup>, VALERIYA PEREKATOVA<sup>1</sup>, EKATERINA SERGEEVA<sup>1</sup>, DARIA KURAKINA<sup>1</sup>, ILYA FIKS<sup>1</sup>, NIKOLAY SAPERKIN<sup>1,2</sup>, MING TANG<sup>3</sup>; YONG ZOU<sup>3</sup>, ELBERT MACAU<sup>4</sup>, AMERICO CUNHA JR<sup>5</sup> AND EFIM PELINOVSKY<sup>1,6</sup>

<sup>1</sup> *Federal Research Center A.V. Gaponov-Grekhov Institute of Applied Physics of the Russian Academy of Sciences, Russia*

<sup>2</sup> *Privolzhsky Research Medical University, Russia*

<sup>3</sup> *School of Physics and Electronic Science, China*

<sup>4</sup> *Federal University of São Paulo, Brazil*

<sup>5</sup> *Rio de Janeiro State University, Brazil*

<sup>6</sup> *National Research University – Higher School of Economics, Russia*

alhil@inbox.ru

## ABSTRACT

COVID-19 outbreak, which resulted in further COVID-19 pandemics, was one of the toughest worldwide challenges in recent years. It clearly showed the necessity of the development of models allowing for simulation and reasonable prediction of epidemiologic processes. Traditional approach is based on compartment models, such as SIR model, firstly introduced by Kermack and McKendrick almost 100 years ago [1]. SIR model employs the separation of population into several groups, such as susceptible (S), infected (I), and recovered (R), and further solution of differential equations describing the dynamics and interactions of these groups. Enhanced compartment models involve larger number of groups into calculations [2], distinguishing exposed (E), dead (D), in critical state (C) and others. SEIR model and its modifications were employed for fitting and predicting the spread of Ebola [3], seasonal influenza [4] and, of course, COVID-19 in a number of countries, e.g. Sweden [5], Japan [6], or large regions of countries, e.g. Italian Region of Lombardy [7]. However, compartment models are unable to account neither for random factors of epidemiologic processes nor individual behavior of persons.

We report on several developed models for the simulation of COVID-19 spread at different epidemiologic levels. We performed the analysis of the daily dynamics of newly revealed COVID-19 cases and COVID-19 associated lethal cases at macro level (whole country or big region), at meso level (megapolis, a region as a whole or a region with the realization of pendulum migration between regional center and periphery cities) and at micro level (city with the respect to its social connections). Analytical models based on logistic [8] and Gompertz [9] equations were developed for macro level. In logistic model total revealed cases  $N(t)$  is determined by equation

$$\frac{dN}{dt} = rN \left( 1 - \frac{N}{N_\infty} \right) \quad (1)$$

which gives exact solutions for  $N(t)$  and daily revealed cases  $I(t)$ , respectively:

$$N(t) = \frac{N_\infty}{1 + \exp[-r(t - \tau)]} \quad (2)$$

$$I(t) = \frac{dN}{dt} = \frac{rN_\infty \exp[-r(t - \tau)]}{\{1 + \exp[-r(t - \tau)]\}^2} \quad (3)$$

In Gompertz model the equation for total revealed cases  $N(t)$  changes to

$$\frac{dN}{dt} = rN \left( 1 - \frac{\ln N}{\ln N_\infty} \right) \quad (4)$$

which leads to the following dynamics of  $N(t)$  and  $I(t)$ , respectively:

$$N(t) = N_\infty \exp \left[ \ln \left( \frac{N_0}{N_\infty} \right) \exp \left( -\frac{r(t - \tau)}{N_\infty} \right) \right] \quad (5)$$

$$I(t) = \frac{dN}{dt} = r \ln \left( \frac{N_{0i}}{N_{\infty i}} \right) \exp \left[ \ln \left( \frac{N_0}{N_\infty} \right) \exp \left( -\frac{r(t - \tau)}{N_\infty} \right) - \frac{r(t - \tau)}{N_\infty} \right] \quad (6)$$

We analyzed three approaches to the description of dynamics newly revealed cases  $I(t)$  and COVID-19 associated lethal cases  $D(t)$ . The first and the second assume that during each wave (1, 2, ...,  $k$ ) of COVID-19 spread dynamics of daily revealed cases and deaths are described independently and by standalone solutions, which allows to express full dynamics as the sum with the respect to number of waves in logistic model

$$I(t) = \sum_{i=1}^k \frac{r_i N_{\infty i} \exp(-r_i[t - \tau_i])}{\{1 + \exp(-r_i[t - \tau_i])\}^2} \quad (7)$$

$$D(t) = \sum_{i=1}^k \frac{\tilde{r}_i D_{\infty i} \exp(-\tilde{r}_i[t - \tilde{\tau}_i])}{\{1 + \exp(-\tilde{r}_i[t - \tilde{\tau}_i])\}^2} \quad (8)$$

or Gompertz model

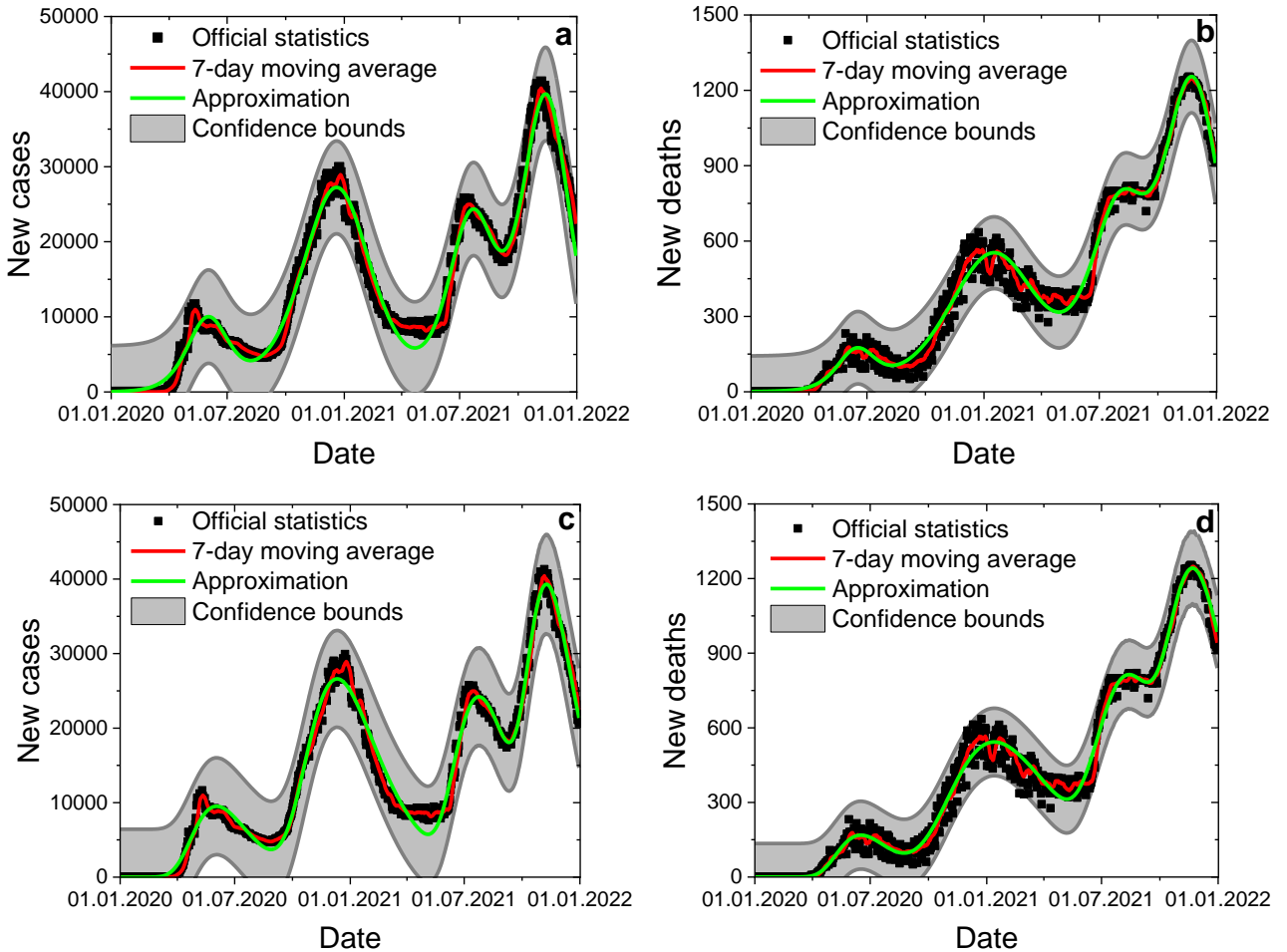
$$I(t) = \sum_{i=1}^k r_i \ln\left(\frac{N_{0i}}{N_{\infty i}}\right) \exp\left(\ln\left[\frac{N_{0i}}{N_{\infty i}}\right] \exp\left[-\frac{r_i(t - \tau_i)}{N_{\infty i}}\right] - \frac{r_i(t - \tau_i)}{N_{\infty i}}\right) \quad (9)$$

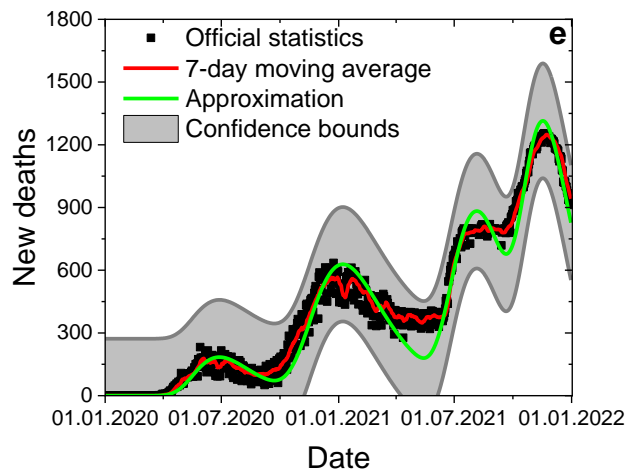
$$D(t) = \sum_{i=1}^k \tilde{r}_i \ln\left(\frac{D_{0i}}{D_{\infty i}}\right) \exp\left(\ln\left[\frac{D_{0i}}{D_{\infty i}}\right] \exp\left[-\frac{\tilde{r}_i(t - \tilde{\tau}_i)}{D_{\infty i}}\right] - \frac{\tilde{r}_i(t - \tilde{\tau}_i)}{D_{\infty i}}\right) \quad (10)$$

while the third approach is aimed to automodel solution for daily new lethal cases dynamics  $D(t)$  calculated from newly revealed cases  $I(t)$  (Eq. 9) by multiplication and time shifts of corresponding dynamics for separate waves:

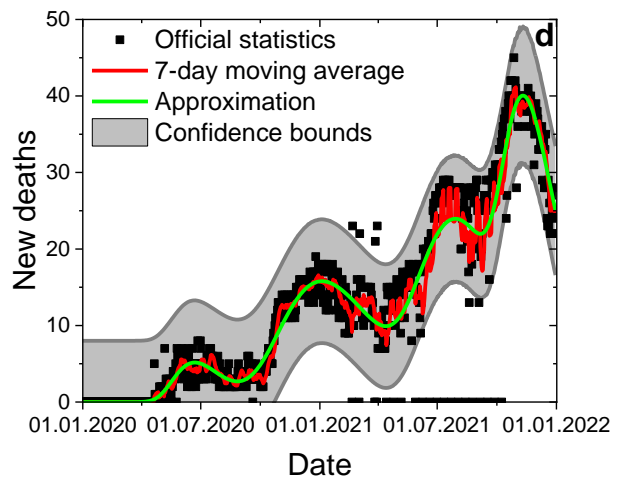
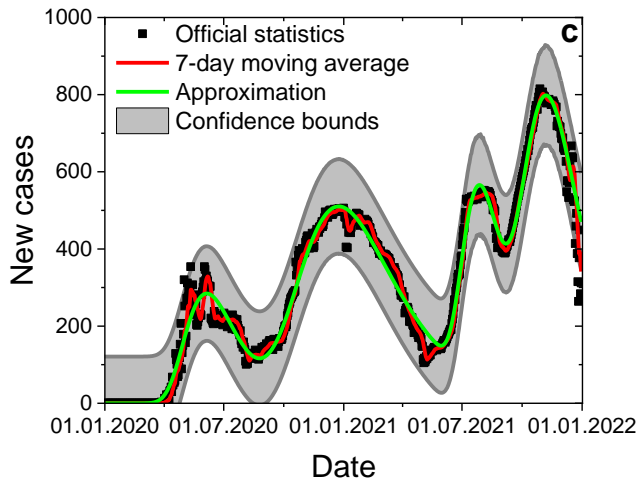
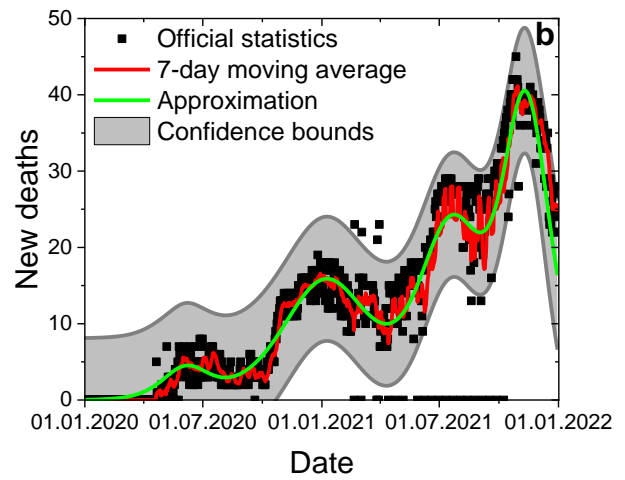
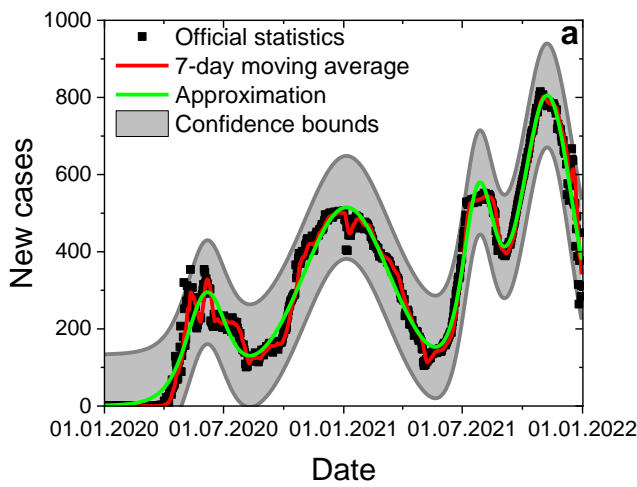
$$D(t) = \sum_{i=1}^k a_i I_i(t - \Delta t_i) \quad (11)$$

It should be noted that (3) is not a solution of Gompertz equation. Developed approaches were employed for the study of COVID-19 spread in different countries and regions, including Russian Federation (Fig.1) and Nizhny Novgorod Region of Russian Federation (Fig. 2).





**Figure 1:** Daily dynamics of newly revealed cases (a, c) and COVID-19 associated lethal cases (b, d, e) in Russian Federation calculated by logistic model (a, b), Gompertz model (c, d) and automodel solution for daily new deaths (e)



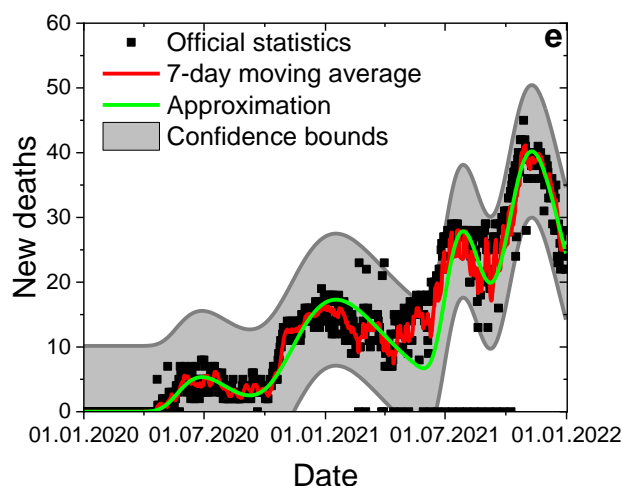


**Figure 2:** Daily dynamics of newly revealed cases (a, c) and COVID-19 associated lethal cases (b, d, e) in Nizhny Novgorod Region calculated by logistic model (a, b), Gompertz model (c, d) and automodel solution for daily new deaths (e)

For the description of COVID-19 spread at meso and micro levels agent-based modeling was employed. This approach assumes that the population is a pool of agents interacting with each other. Individual behavior characteristics are determined by set of constant (e.g. age) and variable (e.g. self-isolation index) parameters. Agent based-modeling also allows accounting for random epidemic factors, restrictive measurements, vaccination etc. Agent-based modeling proved itself as a go-to tool for simulation of epidemiologic process at various levels from supermarket [10] to single city [11] and even the country [12]. We developed agent-based model for COVID-19 spread with accounting for testing system, restrictive measurements and vaccination [13, 14]. The model was also upgraded to multicentral, when studied region is assumed as a number of pools representing regional center and periphery cities with transport connections and pendulum migration between them [15]. The comparison of theoretical and simulated data with accessible official COVID-19 statistics revealed good agreement both for modelling the whole region Nizhny Novgorod Region and single cities within it, which proves the capabilities of developed models.

## ACKNOWLEDGEMENTS

The study was supported by supported by RFBR (project no. 20-51-80004), CNPq (project no. 441016/2020-0), NSFC (project no. 82161148012), and partly supported in the frames of the Governmental Project of the Institute of Applied Physics RAS (Project #FFUF-2021-0014).

## REFERENCES

- [1] W. O. Kermack, A. G. McKendrick, A contribution to the mathematical theory of epidemics, Proc. of the Royal Society of London. Series A 115(772), 700–721, 1927.
- [2] S. He, Y. Peng, K. Sun, SEIR modeling of the COVID-19 and its dynamics, Nonlinear Dyn. 101(3), 1667-1680, 2020.
- [3] A. Bouba, K.B. Helle, K.A. Schneider, Predicting the combined effects of case isolation, safe funeral practices, and contact tracing during Ebola virus disease outbreaks, Plos One, 18(1), e0276351, 2023.
- [4] V.N. Leonenko, S.V. Ivanov, Fitting the SEIR model of seasonal influenza outbreak to the incidence data for Russian cities, Russian J. Numer. Anal. Mathem. Modell., 31(5), 267-279, 2016.
- [5] M. Khairulbahri, The SEIR model incorporating asymptomatic cases, behavioral measures, and lockdowns: Lesson learned from the COVID-19 flow in Sweden, Biomed. Signal Process. Control, 81, 104416, 2023.
- [6] Q. Sun, T. Miyoshi, S. Richard, Analysis of COVID-19 in Japan with extended SEIR model and ensemble Kalman filter, J. Comput. Appl. Math., 419, 114772, 2023.
- [7] J.M. Carcione, J.E. Santos, C. Bagaini, J. Ba, A Simulation of a COVID-19 Epidemic Based on a Deterministic SEIR Model, Front. Public Health, 8, 230, 2020.
- [8] E. Pelinovsky, A. Kurkin, O. Kurkina, M. Kokoulina, A. Epifanova, Logistic equation and COVID-19, Chaos Solitons Fractals 140, 110241, 2020.
- [9] E. Pelinovsky, M. Kokoulina, A. Epifanova, A. Kurkin, O. Kurkina, M. Tang, E. Macau, M. Kirillin, Gompertz model in COVID-19 spreading simulation, Chaos Solitons Fractals 154, 111699, 2022.
- [10] F. Ying, N. O’Clery, Modelling COVID-19 transmission in supermarkets using an agent-based model, Plos One 16(4), e0249821, 2021.

- [11] A. Shoukat, T.N. Vilches, S.M. Moghadas, P. Sah, E.C. Schneider, J. Shaff, A. Ternier, D.A. Chokshi, A.P. Galvani, Lives saved and hospitalizations averted by COVID-19 vaccination in New York City: a modeling study, *Lancet Reg Health Am* 5, 100085, 2022.
- [12] G.N. Rykovanov, S.N. Lebedev, O.V. Zatsepin, G.D. Kaminskii, E.V. Karamov, A.A. Romanyukha, A.M. Feigin, and B.N. Chetverushkin, Agent-based simulation of the COVID-19 epidemic in Russia, *Her. Russ. Acad. Sci.* 92(8), 747–755, 2022.
- [13] M. Kirillin, E. Sergeeva, A. Khilov, D. Kurakina, and N. Saperkin, Monte Carlo simulation of the covid-19 spread in early and peak stages in different regions of the Russian Federation using an agent-based modelling, in *Saratov Fall Meeting, Chinese-Russian workshop on Biophotonics and Bioimaging-2020 1*, 2020.
- [14] M. Kirillin, A. Khilov, V. Perekatova, E. Sergeeva, D. Kurakina, I. Fiks, N. Saperkin, M. Tang, Y. Zou, E. Macau, E. Pelinovsky, Simulation of the first and the second waves of COVID-19 spreading in Russian Federation regions using an agent-based model, *J. Biomed. Photonics Eng.* 9(1), 010302, 2023.
- [15] M. Kirillin, A. Khilov, V. Perekatova, E. Sergeeva, D. Kurakina, I. Fiks, N. Saperkin, M. Tang, Y. Zou, E. Macau, E. Pelinovsky, Multicentral Agent-Based Model of Four Waves of COVID-19 Spreading in Nizhny Novgorod Region of Russian Federation, *J. Biomed. Photonics Eng.* 9(1), 010306, 2023.

## STUDY OF OSMOTIC AND CROSS-LINKING DEFORMATIONS IN BIOLOGICAL TISSUES BY OPTICAL COHERENCE ELASTOGRAPHY

YULIA ALEXANDROVSKAYA<sup>1</sup>, EKATERINA KASIANENKO<sup>2</sup>, OLGA BAUM<sup>2</sup>,  
ALEXANDER SOVETSKY<sup>1</sup>, ALEXANDER MATVEEV<sup>1</sup>, TATIANA SHMIGOL<sup>3</sup>, PAVEL  
KARAVAIKIN<sup>3,4</sup>, VADIM NEGREBETSKY<sup>3</sup>, VLADIMIR ZAITSEV<sup>1</sup>

<sup>1</sup>*A.V. Gaponov-Grekhov Institute of Applied Physics of the Russian Academy of Sciences, Russia*

<sup>2</sup>*Institute of Photon Technologies, Federal Scientific Research Center “Crystallography and Photonics”, Russian Academy of Sciences,, Russia*

<sup>3</sup>*N.I. Pirogov National Research Medical University, Ministry of Health of Russia, Russia*

<sup>4</sup>*Central Clinical Hospital with Polyclinic, Russia*

vyuzai@ipfran.ru

### ABSTRACT

New insights into the diffusion-associated deformations of biological tissues studied by optical coherent elastography (OCE) are discussed in this study. Possible applications of the strain analysis to the diagnostics of early degradation of biological tissues, such as gradual proteoglycan depletion in cartilage, are proposed. It is shown that using the emerging OCE technique enabling quantitative visualization of spatially-resolved strain dynamics [1,2] the osmotically-induced deformations can be distinguished from the ones caused by the formation of collagen cross-links. Various chemical agents, such as organic alcohols, omnipaque, inorganic salts and glutaraldehyde, are considered in terms of their activity in inducing osmotic and cross-linking deformations in tissues and polyacrylamide gels (tissue phantoms) [3].

### ACKNOWLEDGEMENTS

The study was supported by the Russian Science Foundation grant No. 22-12-00295

### REFERENCES

- [1] Alexandrovskaya, Y.; Baum, O.; Sovetsky, A.; Matveyev, A.; Matveev, L.; Sobol, E.; Zaitsev, V. Optical Coherence Elastography as a Tool for Studying Deformations in Biomaterials: Spatially-Resolved Osmotic Strain Dynamics in Cartilaginous Samples. *Materials* **2022**, *15*, 904. <https://doi.org/10.3390/ma15030904>.
- [2] Yu. Alexandrovskaya, O. Baum, V. Zaitsev, A. Sovetsky, A. Matveyev, L. Matveev, K. Larin, E. Sobol, V. Tuchin, Optical and mechanical properties of the cartilage during optical clearing, In book *Tissue optical clearing: new prospects in optical imaging*, CRC Press (Dan Zhu, Elina Genina, and Valery Tuchin Eds.), **2021**, Boca Raton, Florida, United States.
- [3] Alexandrovskaya, Y.M.; Kasianenko, E.M.; Sovetsky, A.A.; Matveyev, A.L.; Zaitsev, V.Y. Spatio-Temporal Dynamics of Diffusion-Associated Deformations of Biological Tissues and Polyacrylamide Gels Observed with Optical Coherence Elastography. *Materials* **2023**, *16*, 2036. <https://doi.org/10.3390/ma16052036>.

## ASSESSING THE APPLICABILITY OF AEROGELS FOR THE ANALYSIS OF SKIN VAPOR SAMPLES IN TERAHERTZ RADIATION

VIACHESLAV ZASEDATEL<sup>1</sup>, YANA TULENEVA<sup>2</sup>, YURY KISTENEV<sup>1</sup>

<sup>1</sup>*Laboratory of Laser Molecular Imaging and Machine Learning, National Research Tomsk State University, Russia*

<sup>2</sup>*Physical Faculty, National Research Tomsk State University, Russia*  
zevs@ido.tsu.ru

### ABSTRACT

Skin vapor analysis can be used to assess human health conditions using various biological markers. Detection of markers is possible using highly sensitive terahertz radiation and various sorbents, such as aerogel. The study shows that the aerogel is a transparent absorbent for terahertz radiation, and is also capable of accumulating samples within 5-10 minutes after contact with human skin. In this case, the samples are suitable for research up to 78 hours.

### INTRODUCTION

Currently, areas of research related to determining the composition of skin vapors using highly sensitive gas analysis are actively developing. The human body in the process of life releases many different substances, including volatile ones. Analysis of biological gas samples, such as exhaled air and skin vapors, can serve as methods for non-invasive analysis of various pathologies and conditions [1]. To determine such substances, non-ionizing, long-wave terahertz radiation is used, which allows the identification of many molecules. In medicine, terahertz spectroscopy is of particular importance because it is an excellent way to characterize a large number of organic molecules. In addition, photons in this radiation range have very low energy, which, compared to existing methods in medicine, gives a tangible advantage to terahertz imaging, since it does not pose a danger of ionization for biological systems. Due to its properties, it allows for rapid non-invasive studies, and the absorption spectra of many organic molecules in the terahertz region have now been obtained. Terahertz spectroscopy makes it possible to analyze interactions both intramolecular and interactions between molecules. Thus, this area contains information about the rotational and low frequency vibrational modes of biological molecules through absorption lines, as well as about the deformations of hydrogen bonds. The vibrational and electronic properties of molecules can be studied over a wide frequency band provided by coherent terahertz spectroscopy in the time domain [2,3].

To analyze samples of skin vapors, methods are needed that allow not only to collect and store samples for a sufficient time, but also to process them with the necessary methods. Various absorbents, in particular aerogels, can be used for this purpose. Aerogels are a porous material, and in the classification of materials, they are classified as mesoporous. Their structure consists of a set of globules, which have a size of the order of several nanometers, connected to each other by a network of air-filled mesopores [4]. It turns out that very thin walls of a few nanometers create a three-dimensional labyrinth of cavities and layers. The cavities have a diameter of about 2-50 nanometers and most often occupy 95% or more of the volume, which indicates that this material consists of 95% or more air. Density is estimated from 1 to 150 kg/m<sup>3</sup> [5]. The most common are quartz aerogels. The minimum density of their evacuated version is 1000 times less than the density of water and even 1.2 times less than the density of air. Such aerogels transmit light in soft ultraviolet, visible and infrared radiation, but the latter contains hydroxyl bands at 3500 cm<sup>-1</sup> and 1600 cm<sup>-1</sup>, typical for quartz, which is obtained by dehydrating silica gels.

Since aerogels can be a promising absorbent for analyzing pathological conditions using skin vapors, this study assessed the capabilities of this material for sampling and analyzing samples in terahertz radiation.

### MATERIAL AND METHODS

The aerogel used in the study was produced at the Federal Research Center "Institute of Catalysis SB RAS" in Novosibirsk, Russia. It has a density of 0.2 g/cm<sup>3</sup> and consists of 80% air and 20% silicon dioxide. The example of aerogel shown on the Figure 1.



**Figure 1:** the example of silica aerogel

To analyze the collected samples, a T-Spec spectrometer (EXPLA) was used, which allows obtaining data containing information about the structure and spectroscopic characteristics of the samples. This spectrometer allows you to scan various images, both in solid and liquid states, but with a size of no more than 20\*20 mm. In this case, the spatial resolution is approximately 1 mm. The appearance and optical design of the T-Spec spectrometer is shown in Figure 2. To generate and record THz radiation, a photoconductive antenna is used, illuminated by very short laser pulses. Pulses are generated by a pump laser with an output power of no more than 100 mW at a wavelength of  $1050 \pm 40$  nm, with a duration of 10 – 150 fs and a repetition rate of about 30 – 100 MHz. The pump beam is divided into two beams, falling on a diaphragm splitter, designated in Figure 4 as BS1, the coefficient for this division is related by the ratio 55:45. Mirrors M1 and M2 direct the beam through the fast delay line to the emitter, and lens L1 focuses the pump beam into a gap on the photoconductive antenna. The slow delay line consists of a corner reflector, which is hollow inside, or a PR4 prism on a stepper motor, as well as a fixed PR3 prism or mirrors. The second beam of the pump beam is directed to the detector antenna by mirror M3, and lens L2 focuses the pump beam into the gap on the photoconductive antenna. A slow delay line is only required in some cases where high spectral resolution is required or very thick samples are available. The wavefront of the electric field of THz radiation forms scanning by a fast delay line with a frequency of 10 Hz. The spectral content of THz radiation is given by the Fourier transform taken from the wavefront, and the absorption spectrum of the substance under study is given by a comparison of the spectra with and without a sample along the path of propagation of THz radiation. To obtain a better signal-to-noise ratio, averaging can be performed over 1024 scanned curves.

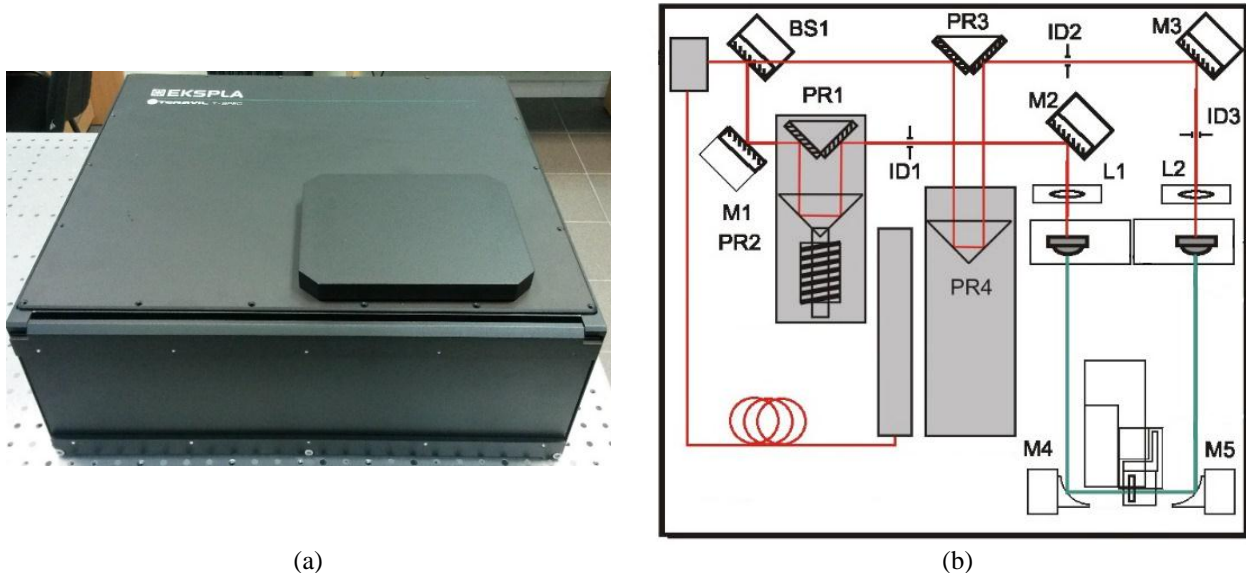


**Figure 2:** (a) spectrometer "T-Spec" (EXPLA) – (b) OPTICAL design of the T-Spec spectrometer

## EXPERIMENTAL DESIGN

The experimental technique consisted of dividing an aerogel sample into 5mm thick plates, which were sequentially fixed on the forearm using a gauze bandage for a certain time, and then, using a metal holder, they were installed in a spectrometer to study them for transmission (Figure 3).



(a)



(b)

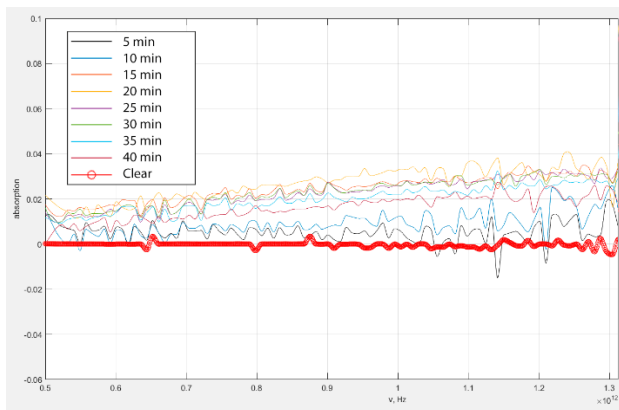
**Figure 3:** (a) placing an airgel sample on the forearm – (b) placing the airgel sample in the spectrometer holder

A reference signal of the absorption spectrum was obtained from each plate (at 4 points due to the heterogeneity of the sample), then the sample was placed on the forearm for 5, 10, 15, 20, 25, 30, 35 and 40 minutes. After this, the absorption spectra of each sample were recorded again.

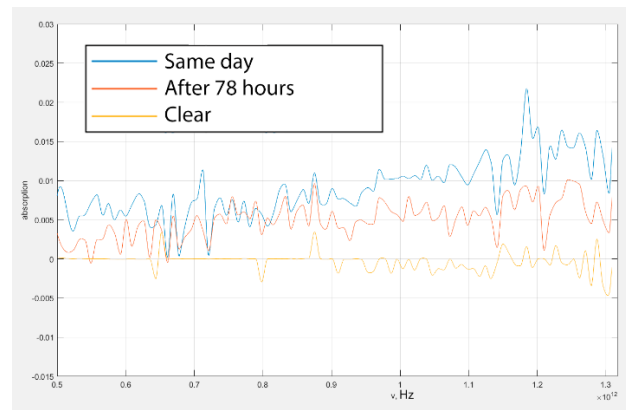
Additionally, spectra of one of the samples (fixed for 5 minutes) were obtained 78 hours after the first measurement.

## RESULTS

The data obtained for each sample at 4 points was averaged. Figure 4 (a) shows the absorption spectra of the samples for each exposure time and Figure 4 (b) shows absorption spectra of evaporation from the surface of the skin in a sample kept on the forearm for 5 minutes on the day the sample was taken and after 78 hours in comparison with a clean sample.



(a)



(b)

**Figure 4:** (a) absorption spectra of evaporation from the skin surface obtained using different airgel samples for each exposure time – (b) absorption spectra of a clean sample and a sample treated twice - immediately after the experiment and 78 hours after the experiment

The spectra obtained from the experiment are complex multicomponent spectra of a mixture of various substances; therefore, the principal component analyze (PCA) was used to find the differences in the spectra. The processing results are presented in Figure 5.

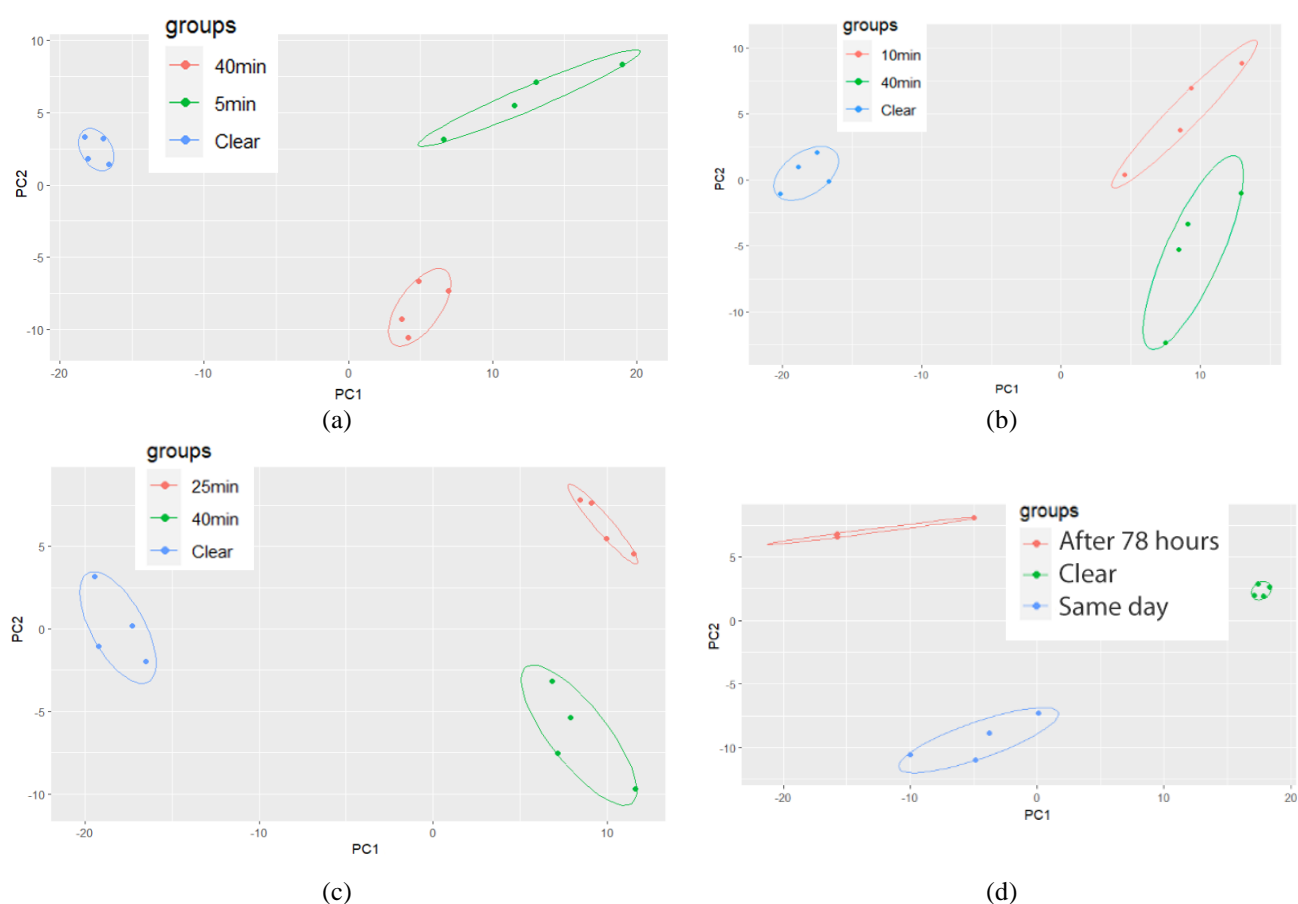


**Figure 5:** representation of aerogel absorption spectra data in various coordinates of the principal components for different exposure times of images on the forearm compared to the clean sample: (a) exposure times of 5 and 40 minutes - (b) exposure times of 10 and 40 minutes - (c) exposure times of 25 and 40 minutes - (d) clean sample and the sample, examined after 78 hours

## CONCLUSION

When analyzed using the principal component method, it is clear that the studied spectra have sufficient separation in the data, which can serve as confirmation of the possibility of the aerogel for use as an absorbent in the selection of skin evaporations. In this case, a sufficient exposure time on the skin surface is 5-10 minutes, which makes it possible to limit subsequent experiments to this time. Also, analysis of the sample, done 78 hours after the first study, shows that the areas corresponding to the pure spectrum are separated from the areas corresponding to the spectra of the samples maintained on the forearm. At the same time, it can be seen that the areas corresponding to the spectra on the day the sample was taken and after 78 hours are also distant from each other, which may indicate temporary degradation of the sample. However, the separation of areas compared to the pure sample allows the sample to be used for subsequent analysis.

## CONTRIBUTION

The research was carried out with the support of a grant under the Decree of the Government of the Russian Federation No. 220 of 09 April 2010 (Agreement No. 075-15-2021-615 of 04 June 2021).

## REFERENCES

- [1] B. de Lacy Costello, A. Amann, H. Al-Kateb, C. Flynn, W. Filipiak, T. Khalid, D. Osborne, N.M. Ratcliffe. A review of the volatiles from the healthy human body. *J Breath Res.* 2014 Mar;8(1):014001. doi: 10.1088/1752-7155/8/1/014001. Epub 2014 Jan 13. PMID: 24421258.
- [2] Stepanov E.V. Measuring device for determining the concentration of sulfur-containing substances in exhaled gas. *Trudy IOFAN*, 2005, vol. 61, pp. 5–47. (in Russ.)
- [3] A. Knyazkova, U. Kistenev, A. Borisov. THz spectroscopy of evaporation from the skin surface in patients with diabetes mellitus. *Optics of the atmosphere and ocean. Atmospheric physics. Materials of the XXV International Symposium*, 2019. p. A-21-A-25.
- [4] T. Petrova, U. Ponomarev, A.A. Solodov, A.M. Solodov, A. Daniluk. Spectroscopic nanoporometry of aerogel. *Letters to JETP*, 2015. vol. 1, p. 68-70. doi: 10.7868/S0370274X15010142
- [5] A. Pozdnyak. Aerogels, their properties and applications. 54th scientific conference of graduate students, undergraduates and students of BSUIR. 2018. p. 198-201.

## RAMAN-LIBS FOR TUMOR TISSUE IMAGING AND CELLS DETECTION

YOUYUAN CHEN, PENGKUN YIN, ZHENGYING PEENG, QINGYU LIN, YIXIANG DUAN

*Research Center of Analytical Instrumentation, School of Mechanical Engineering, Sichuan University, Chengdu, People's Republic of China*

qylin@scu.edu.cn

### ABSTRACT

With cancer seriously hampering the increasing life expectancy of people, developing an instantly diagnostic method has become an urgent objective. we developed a label-free LIBS method for high-throughput recognition of tumor cells based on interpretable deep learning. Saliency maps thus obtained amplified the differences between the spectra of cell lines. The proposed method achieved high accuracy and is seen as an interpretable classification process for cancer cell lines. Moreover, we further focused on the analysis of tumor cells with Raman. We proposed a novel strategy based on signal amplification reaction (i.e. 3D DNA walker and CHA ) and SERS for ultrasensitive detection of tumor cells. The tumor cell can be recognized by the corresponding aptamer sequence and can be detected by this SERS method. Our group also proposed LIBS instrument and method for the diagnostic analysis of clinical lung cancer tissues based on label-free imaging. The heterogeneity of multi-elements and molecular fragments was obtained simultaneously for three types of clinical samples containing different proportions of cancerous tissue by laser-induced breakdown spectroscopy (LIBS) imaging.

### REFERENCES

- [1] Y. Chen, P. Yin, Z. Peng, Q. Lin\*, Y. Duan, Q.. Fan, Z. Wei. High-throughput recognition of tumor cells using label-free elemental characteristics based on interpretable deep learning. *Analytical Chemistry*, 94, 3158–3164, 2022.
- [2] Z. Wei, Q. Lin\*, E. N. Lazareva, P. A. Dyachenko, J. Yang, Y. Duan, V. V. Tuchin\*. Optical clearing of laser-induced tissue plasma. *Laser Physics Letters*, 18,085603, 2021.

**PILOT STUDY OF A LOW-INVASIVE EX VIVO METHOD OF OPTICAL CLEARING SKIN  
USING NEEDLE-FREE INJECTION OF OPTICAL CLEARING AGENTS**

YURIY SURKOV<sup>1,2</sup>, ISABELLA SEREBRYAKOVA<sup>1,2</sup>, ELINA GENINA<sup>1,2</sup> AND V.V. TUCHIN<sup>1,2,3</sup>

<sup>1</sup>*Saratov National Research State University, N.G. Chernyshevsky, Russia*

<sup>2</sup>*National Research Tomsk State University, Russia*

<sup>3</sup>*Institute of Precision Mechanics and Control Problems of the Russian Academy of Sciences, Russia*

e-mail: surkov9898@gmail.com

**ABSTRACT**

Optical imaging techniques have some advantages, such as non-invasiveness, high resolution, relative simplicity and minimization of side effects, which are not achievable by classical medical imaging, such as computed tomography, magnetic resonance imaging and ultrasound. [1, 2]

It is important to note that optical imaging techniques, such as confocal microscopy, optical coherence tomography (OCT), photoacoustic and multiphoton microscopy [1, 2], and phototherapy techniques, such as laser, photodynamic and photothermal therapy, are playing an increasingly important role in modern medical care and research practice [3,4]. However, due to the low transparency of biological tissues, which arises due to the heterogeneity of the refractive indices of the structural components of the tissue and intercellular fluid, as well as due to the absorption of probing radiation by chromophores that are part of biological tissues [1, 5]. As a consequence, optical imaging and phototherapy are applied only to the superficial tissues of the body.

Increasing the intensity of incident radiation can increase the penetration depth of the probing light beam, but this approach will inevitably cause additional stress or damage to surrounding tissues [4]. Optical clearing (OC) of biological tissues is a method of increasing the transparency of biological tissues, designed to increase the efficiency and quality of imaging and the effective depth of phototherapeutic methods [6].

The classical approach to OC uses the application of optical clearing agents (OCAs) to the target area of biological tissue. Alcohols, sugars, organic acids, and others are usually used as OCAs. In case of OC of the skin, the barrier and heterogeneous characteristics of the skin layers prevent the penetration of OC, which leads to low effectiveness of OC and/or requires prolonged application/soaking. [6] Several approaches have been proposed to overcome the barrier properties of the skin, such as mechanical and laser perforations, subcutaneous injection of OCA, sonophoresis, microdermabrasion, and the use of microneedle patches [6, 7]. In this work, we propose a method that allows for rapid and efficient delivery of OCA into the dermal layers using a needle-free injection.

A needle-free injector allows the target substance to be injected under high pressure into the skin. The jet pierces the upper layers of the skin and penetrates the biological tissue through a small hole. In addition, with this method of administration, OCA is distributed throughout the volume of the dermis, in contrast to traditional injection, in which OCA forms a drop under the skin, and more time is required for its uniform distribution [8].

Aqueous 40% solutions of Omnipaque-300 (iohexol 300 mg/ml), polyethylene glycol (PEG-300), polypropylene glycol (PPG), 100% Omnipaque-300 and 100% PEG-300 were used as OCA. The injection volume for each OCA was 50  $\mu$ l. The object of study was 5 areas of skin on the right and left sides of the back, 1.5 cm away from the spine, on the carcass of a male outbred laboratory rat, obtained from the vivarium of the Center for Collective Use of the State Medical University named after V.I. Razumovsky. On the studied areas of the skin, hair was removed using depilatory cream.

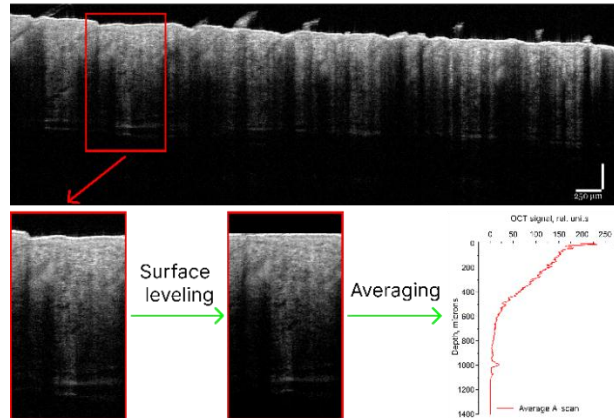
To monitor the skin condition before and immediately after needle-free injection of OCA, dermatoscopy with 10x magnification and high-frequency ultrasound (ultrasound) using the DUB SkinScanner device (tpm taberna pro medicum GmbH, Germany) with two probes operating at central frequencies were used 33 and 75 MHz with a scanning depth of 3.2 mm and axial resolution of 48 and 21  $\mu$ m, respectively. To record changes in the optical characteristics of the skin, a GAN930V2-BU spectral optical coherence tomograph (Thorlabs, USA), with an axial resolution of 5.34, was used.

Artifact-free regions of interest (ROIs) were selected to analyze B-scan OCT images before and after needle-free injection. The width of such ROIs was from 150 to 650  $\mu$ m, the number of ROIs for each OCA was at least 5. The B-scan within the ROI was averaged into one A-scan. Because the skin has an uneven surface, we used a program written in Matlab for horizontal alignment before averaging the B-scan (Figure 1).

To restore the attenuation coefficient of the OCT signal, the algorithm proposed in [9] was used. This method is based on a single scattering model and two assumptions: i. almost all radiation is attenuated within the depth range of the OCT scan; ii. backscattered light, which is recorded by the OCT system, constitutes a fixed fraction of the attenuated probing radiation. These assumptions allow us to estimate the attenuation coefficients for each pixel in the data set. Multiple scattered light is not taken into account. According to this approach, the attenuation coefficient -  $\mu_{\text{OCT}}$ , is determined by the equation:

$$\mu_{OCT}(i) = \frac{1}{2\Delta} \log \left( 1 + \frac{I(i)}{\sum_{i+1}^N I(i)} \right), \#(1)$$

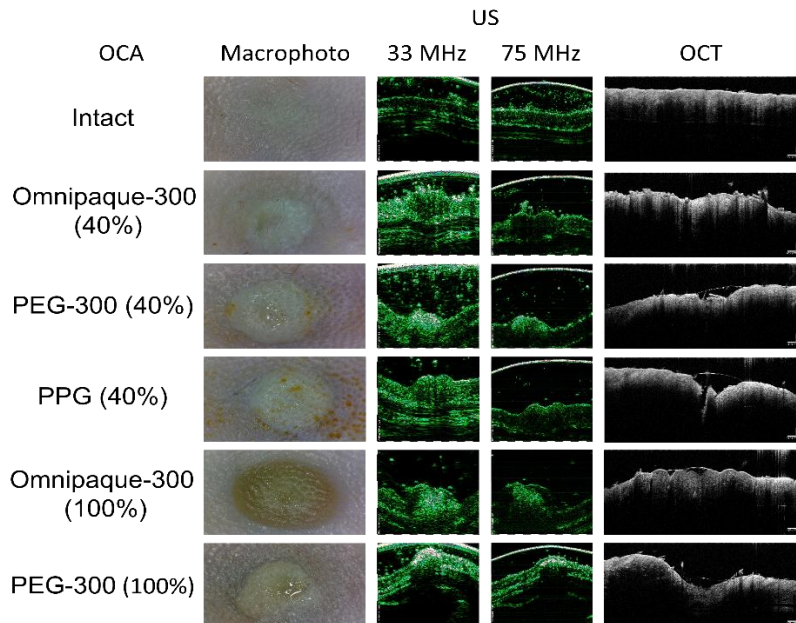
where  $\Delta$  is the pixel size,  $I(i)$  is the signal intensity of the  $i$ -th pixel,  $N$  is the number of pixels in the axial direction.



**Figure 1:** Schematic representation of obtaining an averaged A-scan within the region of interest, highlighted with a red rectangle

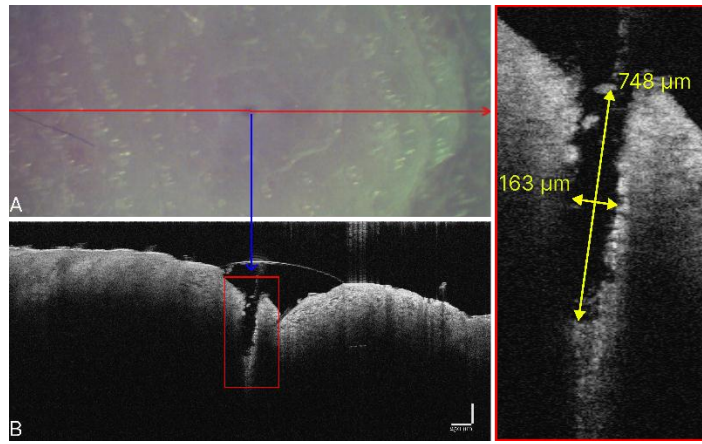
Equation (1) was used to calculate the attenuation coefficient of each pixel in the depth profiles for each B-scan. For each ROI selected for B-scan analysis,  $\mu_{OCT}(z)$  profiles were constructed with a step of 50  $\mu\text{m}$ .

Figure 2 shows dermoscopy images before and after needle-free OCA injection. It can be seen that the OCA injection site becomes whiter, which is associated with an increase in scattering of the tissue area. However, after injection of 100% Omnipaque-300, a decrease in scattering can be observed, which makes the underlying layers of biological tissue visible even to the naked eye - muscle tissue. Figure 2 shows typical images obtained using high-frequency ultrasound before and after OCA injection. It is easy to notice a change in the geometry of biological tissue and the echogenicity of the ultrasound signal after injection of OCA. The volume of tissue that has changed as a result of injection has a fuzzy boundary, the echo signal of which is indistinguishable from the signal of the intact area, which makes it difficult to measure the size of the volume of biological tissue exposed to the action of OCA. The average width and depth of the volume of tissue affected by the change can be estimated at approximately 5.9 and 1.2 mm, respectively. Figure 2 3 column shows typical OCT images before and after OCA injection. You can notice a change in the geometry of the skin after injection and relatively small traces of violation of the integrity of the epidermis.



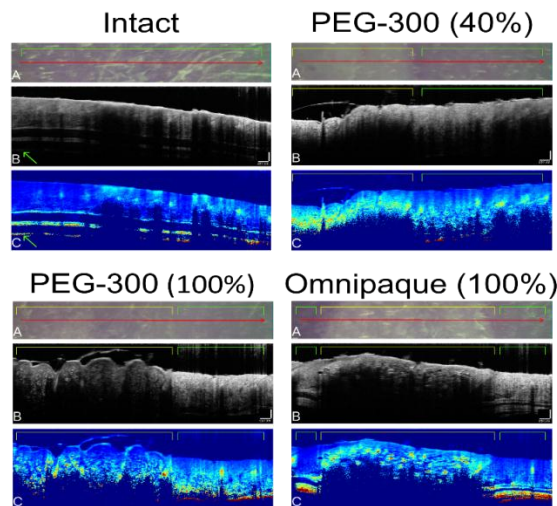
**Figure 2:** Representative images of dermoscopy, ultrasound, and OCT before and after free-needle OCA injection

In Figure 3 you can see the location of the breakdown of biological tissue by the OCA jet; the width and depth were approximately 163 and 748  $\mu\text{m}$ , respectively.



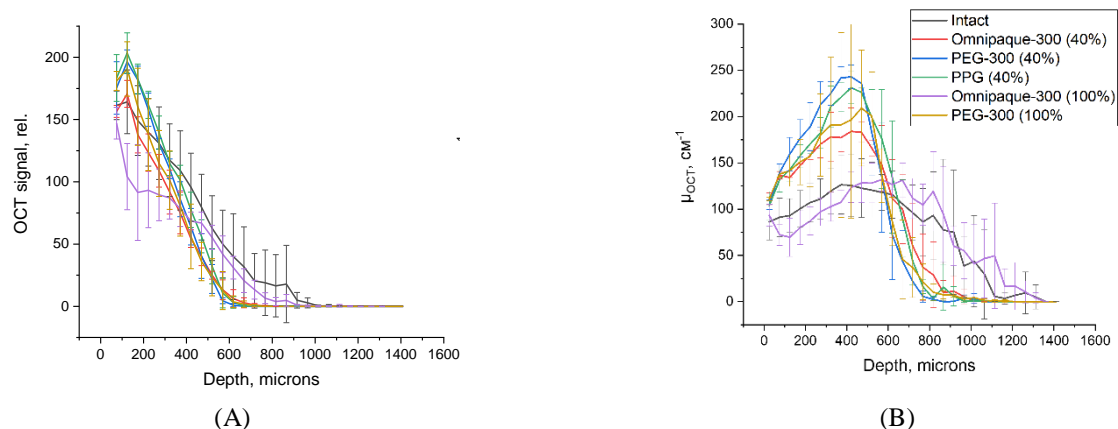
**Figure 3:** Images of the site of puncture of rat skin during needle-free injection of 40% PPG solution, (A) macrophoto, (B) OCT scan

Figure 4 shows a typical macro image, B-scan and reconstructed OCT signal attenuation coefficient image of the skin of a laboratory rat before and after OCA injection. In the attenuation coefficient image, contrast structures that are not visible on the original B-scan can be easily seen. In addition, the attenuation coefficient of the intact dermis has a fairly uniform depth profile; inhomogeneities  $\mu_{\text{OCT}}$  can arise for several reasons: i. violation of the key assumption of the model [9]. It is easy to notice that a needle-free injection of 50  $\mu\text{l}$  of a 40% aqueous solution of PEG-300 causes a significant increase in the attenuation coefficient of the OCT signal compared to the intact area. Injection of undiluted PEG-300 causes a local increase in  $\mu_{\text{OCT}}$ , but less compared to 40% PEG-300. Injection of undiluted Omnipaque leads to a decrease in the attenuation coefficient and intensity of the OCT signal compared to intact skin, however, small areas of increase in  $\mu_{\text{OCT}}$  can be seen.



**Figure 4:** Images of (A) macrophoto with the plane and direction of OCT scanning marked with a red arrow, (B) B-scan of OCT, (C) calculated attenuation coefficient of the OCT signal, skin of a laboratory rat before and after injection of OCA

Figure 5 shows the dependences of the OCT signal depth and  $\mu_{\text{OCT}}$ , calculated from several ROIs for each OCA and intact skin. It can be noted that for intact skin, in Figure 5 it is designated as “Control”, and for undiluted Omnipaque-300 the dependence of the attenuation coefficient has a more horizontal form, while for the remaining OCA  $\mu_{\text{OCT}}$  tends to increase to a depth of  $\sim 400 - 500 \mu\text{m}$ , which can be explained by a larger proportion of multiply scattered photons in the case of injection of the OCA used, with the exception of 100% Omnipaque. The decrease in OCT signal amplitude and  $\mu_{\text{OCT}}$  upon injection of 100% Omnipaque compared to the intact area at a depth of up to  $\sim 350 \mu\text{m}$  demonstrates the potential of this method of delivering OCA into the skin for effective and rapid OC.



**Figure 5** OCT signal (A) profiles and OCT signal attenuation coefficient (B) from depth before (Intact) and after the introduction of various OCAs into the rat casing

A new approach to the rapid delivery of OCA into the casing using the function of fast and effective optical clearing of biological tissues is presented. This method is based on needle-free injection of OCA into the casing. The size of the area changed immediately after injection is approximately 5.9 mm in the lateral direction and 1.2 mm in the direction from the surface of the skin. During a dermoscopic examination, we noticed that a small part of the OCA is removed from the injection area through a breakdown in the skin, resulting from rupture of the upper layers of tissue under the influence of the injector jet. The maximum breakdown size that we observed in the experiments was estimated using OCT, the force width and depth being 163 and 748  $\mu m$ , respectively. The effect of instantaneous OC upon injection of undiluted Omnipaque-300 has been shown.

The reported study was funded by the grant of RFBR (#20-52-56005) and the grant under the Degree of the Government of the Russian Federation No. 220 of 09 April 2010 (Agreement No.075-15-2021-615 of 04 June 2021).

## REFERENCES

- [1] Tuchin V. V., Pop J., Zakharov V. Multimodal optical diagnostics of cancer. – Springer International Publishing, 2020. – p. 1-605.
- [2] Attia A. B. E. et al. A review of clinical photoacoustic imaging: Current and future trends // Photoacoustics. – 2019. – V. 16. – P. 100144.
- [3] Wang J. et al. MoS<sub>2</sub>-based nanocomposites for cancer diagnosis and therapy // Bioactive Materials. – 2021. – V. 6. – №. 11. – P. 4209-4242.
- [4] Liu K. C., Wang J. C. Analysis of thermal damage to laser irradiated tissue based on the dual-phase-lag model // Heat and Mass Transfer. – 2014. – V. 70. – P. 621-628.
- [5] Tainaka K. et al. Chemical principles in tissue clearing for whole-body cell profiling // Annual review of cell and developmental biology. – 2016. – V. 32. – P. 713-741.
- [6] Genina E. A. et al. Optical clearing of tissues: Benefits for biology, medical diagnostics, and phototherapy // Handbook of Optical Biomedical Diagnostics. – 2016. – V. 2. – P. 565-637.
- [7] Ouyang M. et al. Skin optical clearing enabled by dissolving hyaluronic acid microneedle patches // Biological Macromolecules. – 2022. – V. 220. – P. 1188-1196.
- [8] Yu C., Walter M. Needleless injectors for the administration of vaccines: a review of clinical effectiveness. – 2020. – P. 1-33.
- [9] Vermeer K. A. et al. Depth-resolved model-based reconstruction of attenuation coefficients in optical coherence tomography // Biomedical optics express. – 2014. – V. 5. – P. 322-337.

INFLUENCE OF WAVELENGTH OF LIGHT ON ANTIMYCOTIC ACTIVITY OF CHLORINE-CONTAINING PHOTODYNAMIC DRUGS

ANDREI BELIKOV<sup>1,2</sup>, YULIA FEDOROVA<sup>1</sup>, SERGEY SMIRNOV<sup>1</sup>, ANASTASIA KOZLOVA<sup>1</sup> AND LYUDMILA KRAEVA<sup>3</sup>

<sup>1</sup>*Institute of Laser Technologies, ITMO University, Russia*

<sup>2</sup>*Research Institute of Dentistry and Maxillofacial Surgery, Pavlov First State Medical University of St. Petersburg, Russia*

<sup>3</sup>*Laboratory of Medical Bacteriology, Saint-Petersburg Pasteur Institute, Russia*

avbelikov@gmail.com

**ABSTRACT**

Chlorine-containing drugs are a part of photodynamic (PD) therapy which is one of the perspective methods of laser therapy like Low Level Laser Therapy (LLLT) etc. Photodynamic therapy in the context of the treatment of mycoses is very perspective. To date, more than 50 types of fungal infection pathogens have been identified [1]. They are usually divided into three groups: dermatophytes, yeast-like and mold fungi. The most common fungal nail disease is onychomycosis, a fungal infection of the nail plate, nail bed and matrix. Onychomycosis affects from 2 % to 25 % of people [1,2]. The percentage of onychomycosis increases to 50% in patients with pathology of the nail plate [3,4]. Dermatophytes are the main causative agents of onychomycosis, accounting for about 80-90 % of cases of fungal infection [5]. The second most common pathogens of onychomycosis are the yeast-like fungi *Candida* sp., which account for no more than 5-10 % [6]. With nail candidiasis, the most common fungus (in 90% of cases) is *C. albicans*. Much less common causative agents of onychomycosis are *C. parapsilosis*, *C. tropicalis* and *C. guilliermondii*. In third place in terms of frequency of distribution among the population are molds (*Aspergillus* sp., *Scopulariopsis* sp., *Fusarium* sp. and others). Diseases of these fungi occur mainly in countries with tropical and subtropical climates [1]. Thus, in many cases, mycosis is associated with the fungus *C. albicans*. It is a polymorphic fungus capable of growing in yeast, hyphal and pseudo hyphal forms. The hyphal form penetrates the epithelium and endothelium, causing tissue damage and allowing access to the bloodstream. Under certain circumstances, *C. albicans* can cause infections that range from superficial skin infections to life-threatening systemic infections. In addition to onychomycosis (nail candidiasis), *C. albicans* is a common cause of infections of the mucous membranes. In some groups of immunocompromised patients, it also causes life-threatening bloodstream infections that spread to internal organs. Several factors and activities have been identified that contribute to the pathogenic potential of this fungus, such as molecules that mediate adhesion and invasion of host cells, hydrolase secretion, yeast-to-hyphae transition, contact perception and thigmotropism, biofilm formation, phenotypic switching, and a number of attributes fitness. In the treatment of mycosis, chlorine-containing drugs “Chloderm” or “Chloderm with hyaluronic acid” (Russia) can be used. For effective photodynamic treatment it is very important that radiation effectively change the drug, that is its wavelength should be strongly absorbed by drugs. Radiation with wavelengths of 405 nm, 450 nm and 660 nm is strongly absorbed by the chlorine-containing drugs and for this reason can be used for effective photodynamic treatment of mycosis. The type of photodynamic treatment can be divided on to resonant (405 nm, 660 nm), in which light wavelength coincides with absorption peak of photosensitizer, and on to non-resonant (450 nm), when light is strongly absorbed by photosensitizer but does not coincide with peak of its absorbance. The effect of wavelength and radiation dose on the absorption spectra of “Chloderm” or “Chloderm with hyaluronic acid” was studied previously [7-10].

The purpose of this study was to compare the antimycotic activity of the two above-mentioned chlorine-containing photodynamic drugs after resonant or non-resonant photodynamic treatment with the above wavelengths on *C. albicans* fungus and to find the most effective wavelength for such photodynamic treatment.

Scheme of study of antimycotic activity of chlorine-containing photodynamic drugs is presented in Fig.1.

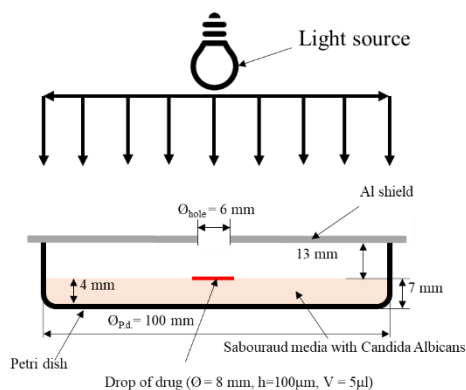


**Figure 1:** Scheme of study of antimycotic activity (PMI) of chlorine-containing photodynamic drugs

The study protocol was as follows: #1 - a drop of a drug was placed on Sabouraud media surface with *C. albicans*; #2 - Al (aluminum) shield with a hole was placed on Petri dish edges to protect zone which surround the treated area from light action; #3 - PD treatment at wavelengths of 405 nm, 450 nm or 656±10 nm with intensity 160 mW/cm<sup>2</sup> per 25 min (to reach dose of 240 J/cm<sup>2</sup>) was performed; #4 - samples were incubated during 24 hours at 37 °C; #5 - Al shield was removed, sample was placed under the optical microscope, and CFU/mm<sup>2</sup> in control or treated area was calculated. For control samples manipulations #1 and #3 were excluded. The value CFU/mm<sup>2</sup> for samples with drop of drug but without PD treatment was also determined (for that samples manipulation #3 was excluded). Antimycotic activity (PMI) was calculated according to following equation:

$$PMI = \frac{CFU_{Control} - CFU_{PD}}{CFU_{Control}} * 100\%, \quad (1)$$

where  $CFU_{Control}$  – colony-forming unit per mm<sup>2</sup> of control sample after 24 hours incubation at 37 °C,  $CFU_{PD}$  – colony-forming unit per mm<sup>2</sup> of PD treated samples after 24 hours incubation at 37°C.

The typical photos of samples after PD treatment with wavelengths of 405nm, 450nm or 656±10 nm are presented in Fig.2.

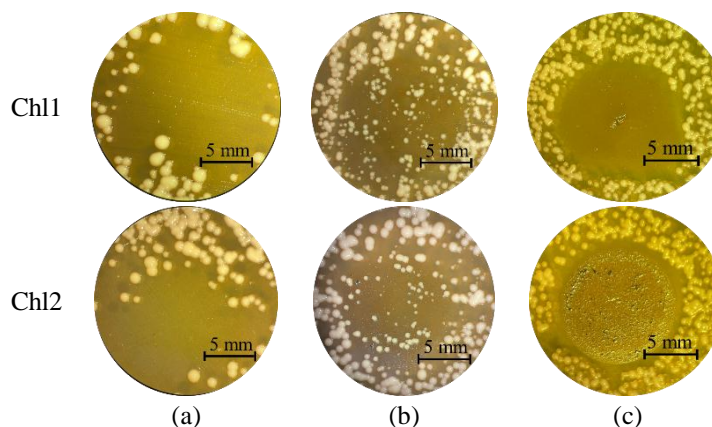


**Figure 2:** Typical photos of Sabouraud media surface with *C. albicans* after application “Chloderm” (Chl1) and “Chloderm with hyaluronic acid” (Chl2), PD treatment with wavelengths of 405 nm (a), 450 nm (b) or 656±10 nm (c) and incubated during 24 hours at 37 °C

The white spheres on the photos are the colony-forming units (CFUs). For control samples CFU/mm<sup>2</sup> was 2.57±0.33. For no-PDT samples CFU/mm<sup>2</sup> was 2.45±0.35 for “Chloderm” and 1.98±0.26 for “Chloderm with hyaluronic acid”. Thus, it was observed that application of “Chloderm” and “Chloderm with hyaluronic acid” without photodynamic treatment do not dramatically influence on CFU/mm<sup>2</sup> of *C. albicans* fungus.

Influence of wavelength of light on antimycotic activity (PMI) of chlorine-containing drugs “Chloderm” (Chl1) and “Chloderm with hyaluronic acid” (Chl2) was studied. A 100% - PMI was observed inside the treated area only after resonant PD treatment with wavelengths of 405 nm or 656±10 nm.

This work is supported by the grants the Russian Science Foundation, RSF 22-25-00468

## REFERENCES

- [1] N.L.Kubasova, Features of diagnosis and treatment of onychomycosis caused by non-dermatomycetes: dissertation. Ph.D., St. Petersburg, p. 121, 2015. (In Russian)
- [2] M. Ghannoum, N. Isham, V. Catalan M., A second look at efficacy criteria for onychomycosis: clinical and mycological cure, *British Journal of Dermatology*. 182-187, 2014.
- [3] M. Chadeganipour, S. Nilipour, G. Ahmadi, Study of onychomycosis in Isfahan, Iran, *Mycoses*. 153-157, 2010.
- [4] G. Tchernev, P.K. Penev, P. Nenoff et al., Onychomycosis: modern diagnostic and treatment approaches, *Wien Med Wochenschr*. 1–12, 2013.
- [5] J. Faergeman, R. Baran, Epidemiology, clinical presentation and diagnosis of onychomycosis, *British Association of Dermatologist*. 1–4, 2003.
- [6] A.Yu. Sergeev, Yu.V. Sergeev, V.Yu. Sergeev, New concepts of pathogenesis, diagnosis and therapy of onychomycosis, *Immunopathology, Allergology, Infectolog*. 9-16, 2007. (In Russian)
- [7] A.V. Belikov, A.D. Kozlova, S.N. Smirnov, Y.V. Fyodorova, Investigation of the Changes in Extinction Spectrum of Modern Chlorine-Containing Photosensitizing Drugs under the Visible Light Action, *Journal of Biomedical Photonics & Engineering*. 040502, 2022.
- [8] A.V. Belikov, Y.V. Fyodorova, A.D. Kozlova, S.N. Smirnov, Laser delivery and spectral study of a modern chlorine-containing drug for the treatment of onychomycosis at laser radiation with a wavelength of 450 nm, *Optics and Spectroscopy*. 872-881, 2022.
- [9] A.V. Belikov, A.D. Kozlova, Y.V. Fyodorova, S.N. Smirnov Laser delivery, processes, and spectral study of a modern chlorine-containing drug for the treatment of onychomycosis under laser influence with a wavelength of 405 nm, *Optics and Spectroscopy*. 841-849, 2023.
- [10] A.V. Belikov, S.N. Smirnov, Tavalinskaya A. D. Laser delivery and spectral study of a chlorin-containing drug for the treatment of onychomycosis with sequential laser ( $\lambda = 2810$  nm) and photodynamic ( $\lambda = 656 \pm 10$  nm), *Optics and Spectroscopy*. 1–9, 2021.

## PHOTOSAFE NON-INVASIVE DETECTION OF DEEP-SEATED LESIONS VIA TRANSMISSION RAMAN SPECTROSCOPY

JIAN YE

*School of Biomedical Engineering, Shanghai Jiao Tong University, Shanghai, China*  
[yejian78@sjtu.edu.cn](mailto:yejian78@sjtu.edu.cn)

### ABSTRACT

Non-invasive localization of deep lesions remains a long-standing pursuit for clinical applications, and its key point lies in the detection and depth estimation of a single lesion in heterogeneous tissues. At present, full optical modalities are widely applied for biomedical sensing, diagnosis, and intraoperative guidance. However, due to the strong photon absorption and scattering of biological tissues, it is challenging to realize *in vivo* deep detections, particularly for those using the safe laser irradiance below biological maximum permissible exposure (MPE) [1]. We reported *in vivo* surface-enhanced transmission Raman spectroscopy (SETRS) to achieve the non-invasive and photosafe localization of deep lesion deeply hidden in either *ex vivo* thick tissues or *in vivo* mice model [2-4]. We synthesized the near-infrared SERS nanotags with single-nanoparticle detection sensitivity, and developed a home-built TRS system with an enlarged beam size to lower the laser power density to  $0.264 \text{ W/cm}^2$ , below the MPE criteria. By using the TRS system, we successfully demonstrated the detection of SERS nanotags through up to 14-cm-thick *ex vivo* porcine tissues, as well as *in vivo* imaging of “phantom” lesions labeled by SERS nanotags in an unshaved mouse under MPE. Furthermore, we theoretically and experimentally demonstrate a universal method to achieve the depth estimation of phantom lesions *ex vivo* tissues, and also realized *in vivo* accurate localization of deep sentinel lymph nodes in a live rat model. This work highlights the potential of transmission Raman-guided identification and noninvasive imaging toward clinically photosafe cancer diagnoses.

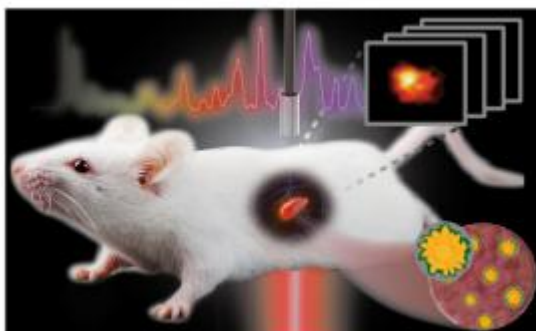


**Figure:** Schematic of non-invasive *in vivo* imaging of deep-seated tumor through living mice by using a transmission setup and ultrabright SERS contrast agent

### REFERENCES

- [1] Li Lin, Haoqi He, Ruiyang Xue, Yumin Zhang, Ziwen Wang, Shuming Nie, Jian Ye, Direct and quantitative assessments of near-infrared light attenuation and spectroscopic detection depth in biological tissues using surface-enhanced Raman scattering, *Med-X*, 2023, 1(1), 9.
- [2] Yumin Zhang, Ruoyu Chen, Fugang Liu, Peng Miao, Li Lin, and Jian Ye, In Vivo Surface-Enhanced Transmission Raman Spectroscopy under Maximum Permissible Exposure: Toward Photosafe Detection of Deep-Seated Tumors, *Small Methods* 2023, 7(2), 2201334.
- [3] Yumin Zhang, Li Lin, Jian Ye. A rapid and universal method for depth estimation of lesions in heterogeneous tissues via photosafe ratiometric transmission Raman spectroscopy. *VIEW*, 2023, 4(4), 20230022.
- [4] Zongyu Wu, Binge Deng, Yutong Zhou, Haoqiang Xie, Yumin Zhang, Li Lin, and Jian Ye. Non-Invasive Detection, Precise Localization, and Perioperative Navigation of In Vivo Deep Lesions Using Transmission Raman Spectroscopy, *Advanced Science*, 2023, 2301721

Научное издание

**Chinese-Russian Workshop on  
Biophotonics and Biomedical Optics-2023  
Proceedings of Chinese-Russian Workshop**

Edited by Polina A. Dyachenko, Dan Zhu and Valery V. Tuchin

SEPTEMBER 25 – 26, 2023

SARATOV

КИТАЙСКО-РОССИЙСКИЙ СЕМИНАР ПО  
БИОФОТОНИКЕ И БИМЕДИЦИНСКОЙ ОПТИКЕ-2023

Сборник материалов китайско-российского семинара

Под редакцией Полины А. Дьяченко, Дана Чжу и Валерия В. Тучина

Подписано в печать 29.12.2023 г. Формат 60×84/16.  
Усл.-печ. л. 3,2. Тираж 500 экз. Заказ № 312

---

Издательство «Саратовский источник»  
г. Саратов, ул. Кутякова 138б, 3 этаж.  
Тел. (8452) 52-05-93  
E-mail: saristoch@bk.ru

Отпечатано в типографии «Саратовский источник»